

Investigating gas turbulence in galactic discs

Timmy Ejdetjärn

Lund Observatory
Lund University



2019-EXA144

Degree project of 60 higher education credits (for a degree of Master)
May 2019

Supervisor: Oscar Agertz

Lund Observatory
Box 43
SE-221 00 Lund
Sweden

Abstract

The interstellar medium of both local and distant disc galaxies is observed to be supersonically turbulent and the turbulent motion of the gas is thought to be important for galaxy formation and evolution, particularly as a key ingredient for star formation. Consequently, this generates a striking relation between the star formation rate (SFR) and gas velocity dispersion (σ_g ; a measurement on the level of turbulence). However, there is no consensus on the origin of this turbulence and its relation with star formation is not yet understood. The two main features of this relation is a plateau of $\sigma_g \sim 10 \text{ km s}^{-1}$ for $\text{SFR} \lesssim 2 - 3 M_\odot \text{ yr}^{-1}$ and a rapid increase of $\sigma_g \gtrsim 100 \text{ km s}^{-1}$ for $\text{SFR} \gtrsim 2 - 3 M_\odot \text{ yr}^{-1}$. These very turbulent gas discs are mainly found in high redshift galaxies, which are observed on the spatial scale of several kpc and are, thus, poorly resolved. This also makes it difficult to accurately correct for beam smearing, which is an observational effect that increases the velocity dispersion due to mixing with the velocity of the disc rotation. Furthermore, they are mainly observed using $\text{H}\alpha$ as a tracer, which is dynamically different from e.g. neutral and molecular hydrogen. In this thesis, I determine which of these factors are crucial for shaping the observed features of the σ_g -SFR relation. Furthermore, I investigate the possible origins of gas turbulence in disc galaxies, focusing on two origins popular in literature: gravitational instability and stellar feedback. To achieve all this, I perform state-of-the-art hydro+ N -body simulations of entire galactic discs with a range of characteristics and feedback processes. I find simulated and observed σ_g -SFR relations to be in excellent agreement. However, the simulated galaxies only reach $\sigma_g \lesssim 50 \text{ km s}^{-1}$ while observational data suggest $\sigma_g \lesssim 150 \text{ km s}^{-1}$. I show that by considering the warm gas phase, $\sigma_{\text{H}\alpha} \sim 130 \text{ km s}^{-1}$ can be reproduced, which highlights the heterogeneity of the data, as different tracers have different kinematics. Furthermore, I demonstrate how even low levels of beam smearing can lead to severe overestimates of the observed turbulent velocity dispersions, a notion that calls into question results from high redshift galaxy observations. I show that the σ_g -SFR remains unchanged when removing stellar feedback and that gas turbulence in disc galaxies is driven by a marginally stable disc and that a galactic disc is naturally drawn towards marginal instability. Finally, I present two new analytic equations to predict the level of turbulence in galaxies from the warm ionised gas phase, using simple equipartition arguments, and in the case of a gravitationally unstable disc, by applying a multi-component Toomre's Q equation. The good match of these equations with simulation data encourage the development of new analytic models based on the warm ionised phase and tools such as Toomre's Q .

Populärvetenskaplig beskrivning

Vilken roll spelar gasturbulens för formationen av stjärnor i diskgalaxer?

Genom en simpel sökning på internet kan man nuförtiden hitta många vackra bilder på enskilda galaxer och på stora samlingar av galaxer, galaxhopar. Vårt solsystem befinner sig i Vintergatan, en spiralgalax inte helt olik många av dessa galaxer. Bilderna visar oftast ljuset som kommer från stjärnor och stjärnstoft, men galaxer består även av gas. Det är från massiva gasmoln i galaxer som stjärnor formas och att förstå gasen i galaxer är därav viktig för att förstå hur galaxer formas och utvecklas med tiden. En galax är den ugn i vilket allt annat kan skapas (stjärnor och planeter, vilka skapar andra byggblock - t.ex. tyngre metaller) och att förstå galaxer lägger därför grunden för ett djupare förståande inom alla astronomins ämnen.

En viktig komponent av en spiralgalax är dess disk, vilken är fylld med stjärnor och gas - dessa formar den kända spiralstrukturen. Det är i galaxer som dessa där större delen av alla stjärnor i universum formas. En kvarstående fråga inom astrofysik är hur miljön i galaxen, dvs. hur gasen beter sig, påverkar formationen av stjärnor. Det är numera väl-observerat att gasen i diskgalaxer är väldigt turbulent - vilket betyder att gasen rör sig väldigt snabbt och oorganiserat. Ännu mer intressant är att denna rörig gasmiljö är relaterad till hur galaxen ser ut - t.ex. påverkar turbulensen hur gasen är utspridd och hur många stjärnor som skapas varje år. Denna relation mellan gasturbulens och stjärnformation är inte ännu förstod och forskare är inte heller eniga om vad som gör gasen så extremt turbulent.

Det som är förstått är att yngre galaxer är mer turbulenta och formar mer stjärnor än äldre galaxer, som redan har förvandlat mestadels av sin gas till stjärnor. Baserat på detta, olika teorier för källan av gasturbulens i diskgalaxer har föreslagits. Slutet av en stjärnas liv kan sluta ganska explosivt, genom olika typer av supernova. Ett förslag är att dessa explosioner skjuter in nog med energi i gasen för att inducera turbulenta rörelser och desto fler stjärnor som formas, desto fler supernova kommer att ske. Ännu en populär idé är att potentiell energi från de massiva gasmolnen blir omvandlad till rörelseenergi när molnen kollapsar och stjärnor formas. Detta är de två huvudsakliga idéer jag undersöker i det här projektet.

I mitt projekt så gör jag numeriska simulationer på diskgalaxer för att avgöra hur gasturbulensen i dessa diskgalaxer ser ut och hur detta påverkar stjärnformation i galaxerna. En stor del av min analys är baserad på att den observationella datan som existerar är väldigt ohomogen, med vilket jag menar att datan kommer från många olika undersökningar och galaxerna observerade är i olika stadier av sina liv. En direkt jämförelse är därför svår att rättvist göra, så länge de olika faktorerna inte är övervägda noggrant.

Galaxer är komplicerade. Det är mycket som går in i receptet för att skapa en diskgalax. Du behöver stjärnor, stjärnstoft och gas, vilka sedan kan ha en stor variation av strukturer: spiralarmar, galaxstav och galaxbulb. Då har jag inte äns nämnt mörk materia och den del-struktur som existerar runt galaxen. Mitt projekt handlar om att förklara en del av detta recept, specifikt gasen, och att försöka förstå hur detta recept ändras med galaxernas ålder.

Contents

1	Introduction	12
2	Theory and Data	17
2.1	The Interstellar Medium	17
2.1.1	The Turbulent ISM	18
2.2	Star formation	22
2.3	Stellar Feedback	23
2.4	Observational data	24
2.4.1	Observational Effects	25
2.5	Toomre’s Q stability criterion	25
2.5.1	Conceptual Derivation	26
2.5.2	Stability of multi-component discs	27
2.6	Analytic Models	28
2.6.1	Gravitational Instability Model	28
2.6.2	Feedback Model	29
3	Method	32
3.1	RAMSES	32
3.1.1	Refinement Strategy	33
3.1.2	Star formation on mesh	35
3.1.3	Modelling stellar feedback	36
3.2	Simulation suite of galaxies	37
3.2.1	Galactic initial conditions	38
3.2.2	Simulation Runs	39
3.3	Analysing data	42
3.3.1	Observational comparison	42
3.3.2	Parameter analysis	42
3.3.3	Defining gas phases	45
4	Results	49
4.1	General properties of simulated galaxies	49
4.1.1	Visual comparison	49
4.1.2	Galaxy PDFs	51

4.1.3	Star formation histories	51
4.1.4	Kennicutt-Schmidt relation	53
4.2	The σ_g -SFR Relation	55
4.2.1	Exploring observational parameters	56
4.3	Mock observations	64
5	Discussion	68
5.1	Analytic models	68
5.1.1	Direct comparison with simulations	69
5.1.2	Model predictions	71
5.2	Driving turbulence in different phases	73
5.2.1	Comparison with analytic equations	73
5.2.2	Energy equipartition	74
5.3	Disc instability as a driver of turbulence	76
5.3.1	Deriving σ_g from Q	77
5.3.2	Driver of the instability	79
6	Summary and Conclusions	83

List of Figures

1.1	A motivating and key relation for this project, which indicates a clear relationship between the gas velocity dispersion σ_g and the star formation rate. The markers show observational data for both local and high redshift galaxies, observed through different means, discussed in Section 2.4 and the sources of the data points are shown in Table 2.1. The details of this relation is discussed in Section 4.2, but an apparent characteristic seen is the steep increase in velocity dispersion (around $\sim 10 M_\odot \text{yr}^{-1}$).	14
2.1	A cartoon illustrating the ISM gas cycle in a few simple steps, starting at the top and following the arrows the steps go as follows: As mentioned in the introduction, stars form from molecular clouds. After some time, these stars affect the ISM through stellar feedback effects, such as supernovae (more thoroughly explained in Section 2.3). This heats up the gas, which in turn excites the atom and likely ionises it, creating the ionised gas phase. Subsequent cooling occurs through radiative cooling, free-free emission, until the ionised gas can recombine into neutral atoms, followed by formation of molecular hydrogen on dust particles. The numbers shown correspond to the numbers in Figure 2.2, which illustrates the transitions between the phases and the colouring seen there corresponds to the colours here.	20

- 2.2 A phase plot of the ISM, showing temperature against density, with arrows and numbers to highlight the continually ongoing gas cycle. Furthermore, I have also included lines that mark the temperature cuts used in (parts of) this project to approximate the different gas phases (e.g. molecular H_2 at 5 - 20 K). The colouring is based on the number density of hydrogen, n_{H} . The values shown here have been calculated from one of the galaxy simulations, `fg50_FB`, during its starburst period (195 Myr simulation time). The characteristics of the simulation is laid out in Table 3.2 and further explained in Section 3.2.1. This plot goes together with Figure 2.1, to illustrate how the phase changes between three major phases: At **1** cold dense gas (molecular clouds) quickly becomes part of the hot and diffuse state at **2** from stars forming and undergoing supernova that heat up the surrounding gas. This phase would not be present on this diagram without these feedback effects. The ionised gas then gradually cools until it recombines into atoms at **3** and eventually molecules, renewing the gas supply for star formation, at **1**. 21
- 3.1 An example of the refinement levels in the AMR grid applied in RAMSES. The figure is of a projected density, where the brighter the grid cell, the higher the density. A dense gas clump can be seen as a white spot in the centre of the figure. This is a zoom-in of a dense molecular cloud in the `fg10_noFB` galaxy. This clump is located 5 kpc from the centre and the axes denote the relative distance from the centre of this image; i.e. the distance from the clump. The size of this clump is around $\Delta x \approx 60$ pc. As mentioned in Section 3.1.1, since this clump is more dense than its surrounding area, it is better resolved; the black grid around the clump has a smaller grid than the red grid, in particular at the edges of this figure. 34
- 3.2 An illustration of how the beams were distributed throughout the galaxy. The galaxy in the background is the `fg10_10FB` run. The red dots correspond to positions in which a beam is located. For each position, different beam sizes are used, as demonstrated for one of the red dots as big black rings. The beams were distributed according to Section 3.3.2. This figure does not accurately portray the number of bins or the beam sizes used. 43
- 3.3 The distribution of $\text{H}\alpha$ emissivities as a function of temperature for the simulation runs. A clear peak can be seen around the temperatures $T \approx 10^4 - 10^5$ K and only the magnitude seems to lessen for the runs without feedback. The fact that the emissivity peak is around the temperature cuts used (Table 3.3) is encouraging for the use of temperature cuts to approximate the gas phases; here it mainly confirms the gas tracer for the warm ionised medium. 47

4.1	Projected properties of the density and temperature the simulated galaxies. The size of these boxes are all $20 \text{ kpc} \times 20 \text{ kpc}$, and the <code>fg10</code> runs are evaluated at $t = 250 \text{ Myr}$, while the <code>fg50</code> runs are calculated at $t = 150 \text{ Myr}$. The runs without any feedback are seen to clump together more and there is a clear correlation with the more dense areas being colder. Some clumping, as seen in the <code>fg50_FB</code> run, is expected in high-redshift galaxies. Outflow of material is another key characteristics in the feedback runs which is observed in these plots.	50
4.2	The density and temperature PDFs of the galaxy in each run. The density is seen to be more spread out for the FB run galaxies. These are calculated around 300 Myr for all simulations, except <code>fg50_FB</code> , which is shown at $t = 200 \text{ Myr}$ in its run. However, they were evaluated for the same time duration in refinement $\Delta t = 100 \text{ Myr}$, due to the difference in when the refinement was turned on (see Section 3.2).	52
4.3	The SFR and gas fraction through time for each run. These are global values, i.e. the SFR and the gas fraction was evaluated for the entire galaxy. The effects of feedback are confirmed to overall work as a suppressor of the star formation rate. The high gas fraction simulations rapidly deplete all its gas supply.	52
4.4	The KS-relation between surface density of gas Σ_g and star formation rate $\dot{\Sigma}_*$. The coloured density diagram is of the simulated and the number of points in each grid is scaled with colour logarithmically, as seen by the colour bars. The black contours in the plot is data from (Bigiel et al. 2008) for local galaxies; two contours are shown, the smaller contour simply shows better where the data is concentrated. The black circles are observations from Kennicutt (1998) of starburst galaxies. All of the data here has been observed as a combination of H I and H_2 and using a beam size of 0.5 kpc (only true for the Bigiel observational data). The three dotted lines represent different depletion times of gas in the local region ($\tau = 0.1, 1, 10 \text{ Gyr}$), their corresponding values are shown in the upper-right plot on their respective line. Each plot represent one simulation run, noted by their respective text boxes. The specifics on the appearance of this figure is discussed in Section 4.1.4.	54
4.5	The σ_g -SFR relation for each simulation run. The markers correspond to the different data points, shown in Table 2.1. The simulation data is seen as the blue-green-yellow heat map behind the data points, where yellow indicates a higher density of points. The velocity dispersion is evaluated from looking at the galaxy head-on, $\theta = 0^\circ$, beam size $\geq 0.5 \text{ kpc}$ and including all of the gas (no defined phase). There is no significant difference noticed between the FB and noFB runs. The exception is the large σ_g in <code>fg10_FB</code> , which is likely from beams mainly containing ionised, diffuse gas.	57

4.6	The velocity dispersion in different SFR bins as a function of the beam size used; here I adopted to have more beam sizes than the rest of the analysis, $d_{\text{beam}} = [0.05, 0.1, 0.25, 0.5, 1, 1.5, 2, 2.5, 3, 4, 5, 6, 7, 8, 9, 10]$ kpc. This figure uses simulated data from <code>fg10_FB</code> . The shape of these lines at different SFRs is not as expected when considering that observational and theoretical work indicate that turbulence should increase with beam size. This likely had to do with small beams landing on very turbulent patches. To properly evaluate this relationship, the weighted average of all the bins were taken for each beam size, using the amount of points in each SFR beam as their weight; shown as a dashed line.	59
4.7	The σ_g -SFR relation for each simulation run. The markers correspond to the different data points, shown in Table 2.1. The simulation data is seen as the green-yellow histogram behind the data points, where yellow indicates a higher density of points. The velocity dispersion is evaluated from every inclination angle, $\theta = 0 - 90^\circ$, and including all of the gas (no temperature mask). The possible effects of beam smearing are highlighted when compared to Figure 4.5. Each angle has a slightly different curve for this relation, which can clearly be seen from the histogram in <code>fg10_FB</code> . There is no discernible difference between FB and noFB runs.	60
4.8	The velocity dispersion in different SFR bins as a function of the galaxy inclination. Left plot shows the <code>fg10_FB</code> data and the right shows the <code>fg50_FB</code> data. The dashed line is the averaged quantity, using the amount of points in each bin as their respective weights. A clear increase in σ_{LOS} is seen with inclination and, for a high SFR region, even a small uncorrected inclination $\theta = 45^\circ$, affects the velocity dispersion severely $\sigma_{LOS} \sim 100 \text{ km s}^{-1}$. The implications of these is especially prominent in high-redshift galaxies. . . .	61
4.9	The σ_g -SFR relation in the <code>fg10</code> simulation for different gas tracers, using the straightforward approach of temperature cuts to defined the gas phases. Molecular and atomic σ_g are seen to vary only slightly when including feedback, while $H\alpha$ is noticeably higher for the feedback run. This makes comparisons between phases troublesome and their differences need to be kept in mind.	62
4.10	The σ_g -SFR relation in the <code>fg50</code> simulation for different gas tracers, using the straightforward approach of temperature cuts to defined the gas phases. Molecular and atomic σ_g are seen to vary only slightly when including feedback, while $H\alpha$ is significantly higher for the feedback run. This makes comparisons between phases troublesome and their differences need to be kept in mind.	63

4.11	A projection map of the different gas phases in the interstellar medium, showing the feedback simulations of both gas fractions. Here, the number density n is denoted with H_2 , HI or $H\alpha$, which all are the weighted number density, using the weights relevant for the corresponding phases (described in Section 3.3). Here only the FB runs are shown. The projections for <code>fg10_FB</code> are at $t = 250$ Myr and <code>fg50_FB</code> is at $t = 150$ Myr.	65
4.12	The σ_g -SFR relation in the <code>fg10_FB</code> and <code>fg50_FB</code> cases, using the more refined method for determining the different gas phases (detailed in Section 3.3.3). Comparing to Figure 4.10, which was a more rudimentary approach, these simulations are slightly different. Most notably, the σ_g for $H\alpha$ has changed for the lower gas fraction galaxy: the SFR is lower, which might be due to the warm ionised phase not being present in star forming clouds for long enough. The data presented here is evaluated from simulation outputs ($150 < t < 300$) Myr.	66
4.13	The σ_g -SFR relation for the $H\alpha$ tracer, using the detailed approach discussed in Section 3.3. The three plots are identical except that they show data for specific beam sizes, as written in the text boxes. This figure is meant to demonstrate the bias of the observational data, as high-redshift galaxies are mainly observed at with large beams sizes, equivalent to poor (large) spatial resolutions. The data used here is only for the <code>fg_50FB</code> run, evaluated for several at $270 > t > 150$ Myr.	67
5.1	The σ_g -SFR relation predicted by the GI (left) and FB (right) analytic models (shown as lines) along with data points from the references in Table 2.1. The colour of the lines correspond to the free parameter values shown in the legends and using $v_c = 200$ km s ⁻¹ , while the shaded areas represent the interval $v_c = 150 - 250$ km s ⁻¹ ; chosen for comparisons with Figure 3 in KB16. The free parameters were chosen to encompass the entirety of the observational data.	69
5.2	A direct comparison between the velocity dispersion from simulations (<code>fg50_FB</code>) and the analytic models in KB16. The colours correspond to the GI (blue) and FB (yellow) models and the different areas show where 30, 68 and 80% of the data is encompassed, centered around the region with the most points of data. The plot on the left has assumed the same Toomre Q values as in KB16 while the right plot uses the corresponding values derived from the simulation. The combined Q is here defined as Q for a thin disc.	70

5.3	The relation predicted by the KB10 model between σ , SFR and the global gas fraction, f_g . The crosses show data from my simulations while the other markers represent the data points from Table 2.1. The specific curve predicted by the GI model is seen in Eq. 5.1, and is visualised as a red line and the curve predicted by the FB model is shown in Eq. 5.2. The coloured regions correspond to a range of possible values for the galaxies. The left and right plot adopt different ranges, to illustrate that a good match relies heavily on the exact values applied. <i>Left:</i> The GI model adopts $\epsilon_{\text{ff}} = 5\%$ for the line and $\epsilon_{\text{ff}} = 1 - 10\%$ as the range. The FB model adopts $\Sigma_{\text{tot}} = 100 \text{ M}_{\odot} \text{ kpc}^{-2}$ $\Sigma_{\text{tot}} = 50 - 1000 \text{ M}_{\odot} \text{ kpc}^{-2}$. <i>Right:</i> The GI model adopts $\epsilon_{\text{ff}} = 1\%$ for the line and $\epsilon_{\text{ff}} = 0.5 - 5\%$ as the range. The FB model adopts $\Sigma_{\text{tot}} = 50 \text{ M}_{\odot} \text{ kpc}^{-2}$ for the line and $\Sigma_{\text{tot}} = 20 - 3000 \text{ M}_{\odot} \text{ kpc}^{-2}$ for the range.	72
5.4	Toomre Q values plotted against the radial distance from the centre, including all runs; fg10 on the left and fg50 on the right, where the dotted lines are the runs without any feedback. The Q -values shown are for the gas, stars and the combined parameter, using three different methods for combining these, discussed in this section and explained in Section 2.5.2. These values were evaluated at kpc-scale beam size.	73
5.5	The velocity dispersion for $\text{H}\alpha$ derived from simulations plotted against the velocity dispersion predicted by the GI and FB models. The left plot assumes constant Toomre Q parameters, while the right one uses values derived from the simulation. These plots use the fg_50FB data.	75
5.6	The relation between the $\sigma_{\text{H}\alpha}$ analytically derived, Eq. 5.7, and the one calculated from simulations. Different factors for the energy contributed by $\text{H}\alpha$ are used and the best agreement seem to be given for $F_{\text{H}\alpha} \approx 40\%$	76
5.7	A direct comparison between the σ_g calculated from simulations and the ones predicted from Eq. 5.8 and 5.9; derived from two different approaches of combining Toomre Q parameters. The left and right plots show the differences between a slight change in the combined Q , motivated by the values seen in Figure 5.4. Both approaches seem to cluster around 50 km s^{-1} and 5 km s^{-1} . The lower values arise due to the outer region of the galaxy, where the Toomre Q are significantly different.	78
5.8	The fraction of mass in a marginally stable state ($Q \leq 2$), for different Toomre Q , as a function of the simulation time. Dashed lines correspond to the region in which the instability is driven by the gas. A clear transition from gas- to star-driven instability is seen to occur rather quickly. Note: the actual transition value is somewhere between the two data points with a dashed line between them.	80

5.9	The fraction of mass in a marginally stable state disc ($Q \leq 2$), for different Toomre Q , as a function of the total gas fraction of the galaxy. Dashed lines correspond to the region in which the instability is driven by the gas. A clear transition from gas- to star-driven instability is seen to occur rather quickly. Note: the actual transition occurs somewhere between the two data points with a dashed line between them.	81
5.10	The ratio of TQ calculated for the gas and star components as a function of the global gas fraction. The product of the thickness weights T and Q values determine which component is dominating the instability. For a thin disc ($T = 1$) the ratio is simply a comparison between the Q parameters. The dashed line corresponds to the region in which the instability shifts from being driven by the gas or stars, where a ratio $T_g Q_g / T_* Q_* < 1$ indicates that the gas is driving the instability.	82

List of Tables

2.1	The complete literature library for the data used involving SFR and σ . This table relates each reference to a marker, which are used throughout the project when plotting the quantities from that reference. To note is that most of the beam sizes and redshifts are very approximate, e.g. Alcorn et al. (2018) analysed samples of entire dwarf galaxies with a variety of sizes. Galaxies noted with a redshift ‘local’ were observed at redshifts much smaller than 1, but the precise redshift is usually not specified in their source. The data of this table is very heterogeneous, i.e. the observations are of different types of disc galaxies (e.g. normal, dwarf, merged galaxies) with different properties (e.g. mass, morphology). This is explained in Section 2.4, and its implications are discussed in the Summary, Chapter 6.	31
3.1	Initial conditions used for each run of simulated galaxies, explained in Section 3.2.1. The parameters are identical between runs with the same galaxy properties (gas fractions) but different physics (with and without feedback); hence the FB/noFB notation.	40
3.2	Important characteristics of each simulation run. The choice of when to refine the simulations is motivated in Section 3.2.	41
3.3	Temperature cuts performed during analysis and their respective phase and tracer analogue. The cuts are the same as shown in Figure 2.2 and are evidently approximative.	45
4.1	The scaling between σ_g and SFR, determined from fitting function of the shape in Equation 4.1 and described in this Section.	55

Chapter 1

Introduction

Contemporary galaxy formation theories have come a long way and are nowadays able to reproduce global properties of galaxies, such as masses and sizes, over the lifespan of the Universe. These theories are based on known physical effects ranging from cosmological structure formation to the intricate details of star formation. However, a completely predictive framework does not yet exist, leaving the details of galaxy formation a major unsolved problem in modern astrophysics (see e.g. [Naab & Ostriker 2017](#), for a review on current obstacles in theoretical work). In broad strokes, there are two ‘flavours’ of galaxies: star forming (disc) and quenched (elliptical/spheroidal) galaxies. The latter are believed to originate from the former, either through merger or secular evolution, which makes disc galaxies an important progenitor for other types of massive galaxies (see e.g. [Benson 2010](#)).

Although quite diverse, disc galaxies are thought to be constituted by at least three major components: a dark matter halo, a bulge and a disc. The dark matter halo surrounds the entire galaxy and its characteristics are believed to set important properties of galaxies ([Watson & Conroy 2013](#); [Tinker et al. 2013](#); [Gu et al. 2016](#)). In the Milky Way, the bulge is in the centre of the galaxy, hosting a super massive black hole, but is otherwise composed of mainly older stars. Galactic discs have stars, gas and dust within them and may exhibit substructures, such as spiral arms and bars; then referred to as spiral galaxies. The gaseous and dusty part in a disc galaxy is known as the interstellar medium (ISM) and can be further split into different components related to the phases of the gas.

The multi-phase nature of the ISM was first motivated, from a theoretical view, by [McKee & Ostriker \(1977\)](#). They suggested that the ISM had three major phases stemming from the shockwave heating caused by supernova explosions. These phases are apparent as dense molecular clouds, neutral atomic gas and diffuse ionised gas. The different densities and velocities of the phases lead to a noticeably different dynamics in each phase (see e.g. [Hensler 2009](#), for a review of the ISM phases). Furthermore, momentum and energy input by massive stars via stellar feedback effects (e.g. supernovae explosions) can drive galactic outflows of hot gas, which play a major role in galaxy evolution (e.g. [Hopkins et al. 2012](#); [Hayward & Hopkins 2017](#)).

Star formation occurs in giant molecular clouds at a low efficiency of a few percent per free-fall-time over a wide range of scales ([Krumholz & Tan 2007](#); [Bigiel et al. 2008](#),

2011; Salim et al. 2015), but much higher efficiencies are possible in individual clouds (Lee et al. 2016). This indicates that galaxy formation is a very inefficient process, suggested to be regulated by feedback effects; supernovae, stellar winds and stellar radiation (Agertz & Kravtsov 2015, 2016). However, the rate at which stars form is very different between local and high redshift galaxies, as the latter tend to have more of their mass in gas, which allows them to reach star formation rates (SFR) from tens up to thousands $M_{\odot} \text{ yr}^{-1}$ (then referred to as *starburst* galaxies; Kennicutt 1998). As a comparison, the Milky Way has a SFR of $\sim 2 M_{\odot} \text{ yr}^{-1}$ (Chomiuk & Povich 2011; Licquia & Newman 2015). Local disc galaxies can also reach very high SFRs, but due to the lack of gas this requires triggering from external factors (e.g. mergers and gravitational compression).

A striking property of the gas in the ISM is that it is supersonically turbulent across a wide range of spatial scales (e.g. Elmegreen & Scalo 2004; Mac Low & Klessen 2004; McKee & Ostriker 2007) and even for several different observational tracers of gas (detailed in Section 2.4). This means it has a seemingly random motion, independent of its bulk velocity, which significantly exceeds the speed of sound in the medium, hence ‘supersonic’. This turbulence can readily be understood to help mix the material in the galaxy and, through this, indirectly set the elemental abundances of newly formed stars (Yang & Krumholz 2012; Armillotta et al. 2018).

However, it has a more crucial impact on galactic properties such as the density distribution of the gas (e.g. Ostriker et al. 1999), understood as over- and underdensities caused by stochastic fluctuations from the turbulent motion. On smaller scales, turbulence is believed to be important for the initial core mass function, which is tightly related to the initial mass function of stars (Hopkins et al. 2012). From this, one can infer that turbulence is strongly connected to star formation, which in turn is crucial for the formation and evolution of galaxies, as it changes with galactic properties and redshift (see e.g. the review by Glazebrook 2013).

Indeed, modern observations do indicate that there is a strong correlation between the star formation rate (SFR) and gas velocity dispersion (σ_g ; an observational proxy for turbulent motion, discussed in Section 2.4.1) in disc galaxies. This striking relation is shown for observational data of local and high redshift galaxies in Figure 1.1, with the references and specifics of the data points laid out in Section 2.4. One of the features of this plot is the sharp increase in σ_g at $\sim 10 M_{\odot} \text{ yr}^{-1}$. There is also a plateau around $\sigma_g \sim 10 \text{ km s}^{-1}$, which is where most local galaxies lie. Higher redshift galaxies are commonly observed with $\sigma_g \sim 50 - 100 \text{ km s}^{-1}$ and, as previously mentioned, at higher SFRs.

However, the origin of the ISM turbulence is still not understood, despite being an increasingly active field of studies (see e.g. the recent work of Hung et al. 2019; Yu et al. 2019). Motivated by this, one of the primary goals of this thesis is to investigate the source of turbulence and the σ_g -SFR relationship in disc galaxies. Several origins have been suggested for the gas turbulence (presented in Section 2.1.1), but for this project I intend to focus on two popular solutions:

- **Gravitational instability:** In order for a region to undergo a high rate of star formation, there needs to be a lot of gas to support this. The more gas available, the

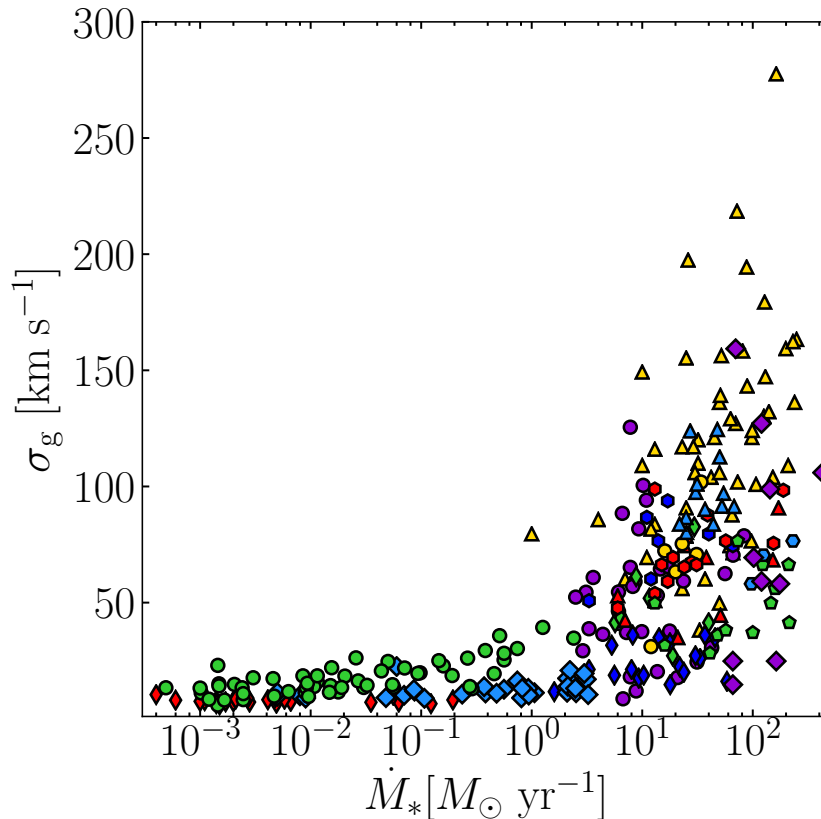


Figure 1.1: A motivating and key relation for this project, which indicates a clear relationship between the gas velocity dispersion σ_g and the star formation rate. The markers show observational data for both local and high redshift galaxies, observed through different means, discussed in Section 2.4 and the sources of the data points are shown in Table 2.1. The details of this relation is discussed in Section 4.2, but an apparent characteristic seen is the steep increase in velocity dispersion (around $\sim 10 M_\odot \text{ yr}^{-1}$).

more gravitational interaction between the gas, leading to an instability which turns potential energy into turbulent energy.

- **Stellar feedback:** A region with a lot of young massive stars will experience a lot of feedback effects, like supernova explosions. The energy ejected this way is naturally suggested to drive the highly turbulent motions of the gas.

Efforts have been made to evaluate the galactic turbulence through analytic models, which usually focus on one particular possible origin. In Krumholz & Burkart (2016), the galaxy-averaged velocity dispersion of a galaxy is suggested to be mainly gravity-driven. Their model is based on an analytic steady-state solution of a galactic disc by Krumholz & Burkert (2010), which they compare with a feedback-driven model by Faucher-Giguère et al. (2013). While analytic models are useful for comparisons with data, as they can help

evaluate the ongoing physical effects, they also tend to oversimplify the problem at hand and reduce the degrees of freedom to form simple relations. In particular, the two models described here have not been thoroughly analysed and complementary numerical studies are necessary to fully understand the problem.

Numerical simulations of galaxies have over the decades become a very sophisticated and reliable tool for understanding the formation and evolution of galaxies (see [Naab & Ostriker 2017](#), for a review). These simulations have been able to reproduce observed quantities at multiple different scales and are crucial to help us with a detailed view of galaxies.

I will use RAMSES, an N-body+hydrodynamical code, to perform state-of-the-art simulations of galactic disc, in order to investigate the role of gravity and stellar feedback in driving interstellar gas turbulence. This is achieved by varying the galactic parameters and the included physics (e.g. feedback processes) and evaluating the resulting velocity dispersions under different conditions. For the analysis, comparisons are done between simulations and analytic predictions, which can help with establishing what the source may be. Furthermore, I present two predictive equations for the velocity dispersion based on the warm ionised gas phase and for a marginally stable disc.

Layout of my thesis

In Chapter 2, I will go over in detail the nature of the ISM, star formation, feedback processes as well as the theoretical framework used for stability analysis. I also go into depth about the core problem of my thesis; the supersonic turbulence of the ISM and the SFR- σ_g relation, while discussing relevant observational data in Section 2.4. In particular, the two analytical models for feedback- and gravity-driven galactic turbulence are presented in detail in Section 2.3 and 2.6.1, respectively.

In Chapter 3, I describe the suite used for the simulations, which includes how star formation and feedback is implemented. An outline of how the RAMSES code operates, and how the data analysis was carried out, are also presented here.

In Chapter 4, I first validate the simulation data by comparing the data with known quantities and features. I show my findings on the calculated gas turbulence in disc galaxies and explore its dependence on different observational parameters, discussed in the previous chapter. Mock observations are done to perform detailed analysis of the gas phases.

In Chapter 5, I carry out a direct comparison of the gas velocity dispersion between models of feedback and no feedback, to determine its impact of driving turbulence. The analytic models are compared with data and against each other. Additionally, some key assumptions of the models are scrutinised using the stability analysis previously discussed.

In Chapter 6, I summarise the work that has been done in this project and the derived results. For the lay reader, I recommend reading the main conclusions of this project, summarised on page 85. By reflecting on my discussions I aim to say whether interstellar turbulence in galactic discs is feedback- or gravity-driven. Finally, I end by recommending future work and improvements of this work as well as the analysed analytic models.

Summary of Chapter 1:

Gas turbulence in galactic discs is an ongoing research topic. Interstellar turbulence is thought to play a key role in controlling aspects of star formation and other galactic properties. However, there are still several unanswered questions within this field that remain, one of which is the **key question:** *what is driving the turbulence in the interstellar medium?* While several solutions have been suggested, gravitational instability and stellar feedback are popular contenders, for which there are predictive, analytic models. In this project, I will use numerical simulations to investigate the source of interstellar turbulence, its relation with star formation and new ways of predicting the level of turbulence from simple stability arguments.

Chapter 2

Theory and Data

In this chapter, I discuss characteristics of the interstellar medium, as well as how star formation and feedback occur in a galaxy. These are related to the core concept of the project: gas turbulence in galactic discs. Focus is also put on describing how the turbulence of the interstellar medium shapes galaxy characteristics and the key relation and motivation behind this work, the σ_g -SFR relation, as mentioned in the introduction. Furthermore, I discuss the observational data of these two parameters; how the quantities are calculated from observations as well as potential measuring biases. The specific data used throughout the plots of this thesis is also discussed here.

As mentioned in the introduction, the analytical models used for comparison are dependent on the stability of the disc, and this needs to be carefully implemented. Therefore, the theoretical framework I use for analysing disc instabilities is presented here, namely Toomre's Q parameter, along with a discussion on how the different parameters should be handled. Finally, the gravity- and feedback-driven analytic models, which are the origin of turbulence in focus during this project, are laid out and discussed in detail.

2.1 The Interstellar Medium

The entirety of the gas in a galactic disc is often referred to as the interstellar medium (ISM), which contains several phases of gas. The idea of a multi-phase gas in galaxies was initially proposed by [McKee & Ostriker \(1977\)](#), who presented the idea of the ISM having three distinctive phases originating from supernova explosions. Today, there are generally five major phases which are considered (see e.g. [Ferrière 2001](#), for a review), with characteristic densities and temperatures; correlated by colder gas phases being more dense. These phases are usually referred as: cold molecular medium, cold neutral medium (atomic gas), warm neutral medium (atomic gas), warm ionised medium, hot ionised medium. However, these phases do not possess any well-defined boundaries and instead the temperatures and densities of the gas in the ISM are continuous, meaning there is an overlap of the phases. Furthermore, the composition of the ISM (in terms of mass) is 70.4% of hydrogen, 28.1% of helium and 1.5% of heavier elements, i.e. metals (e.g. [Spitzer 1978](#)). Most of the metals

in a galaxy are locked into dust particles, which are relevant for the ISM since they act as a site for atoms to condense onto, and form molecules (e.g. [Hensler 2009](#)).

The ISM phases do not follow an identical distribution throughout a galaxy. For example, most of the ISM is located in its atomic phase, which is distributed homogeneously throughout the gas disc; neutral hydrogen has been found to have a constant surface density out to a radius of about 14 kpc in the Milky Way ([Diplas & Savage 1991](#)). However, most of the dense molecular gas in our galaxy resides within the spiral arms, inside giant molecular clouds, as the increased density within the arms allow for gas to more easily cool through collisions (e.g. [Elmegreen 2011](#)). The arms can be seen as local maximum of a density wave “travelling” through the disc (e.g. [Binney & Tremaine 1987](#)). Molecular hydrogen is also most prominent within the inner part of our galaxy; out to around 8 kpc ([Clemens & Barvainis 1988](#); [Bigiel et al. 2008](#)). These places are therefore the regions where star formation is primarily occurring. Additionally, the typical size of a molecular cloud is in the range 5 – 200 pc and their typical mass can lay between $10^3 - 10^7 M_{\odot}$ (e.g. [Larson 1981](#); [Murray 2011](#)). This is true for local spiral galaxies. However, the structure of galaxies at higher redshift, which have yet to turn the majority of their gas into stars, consist mainly of big, self-gravitating clumps of gas. These bright, star forming clumps have sizes of ~ 1 kpc and masses on the order of $\sim 10^9 M_{\odot}$ (e.g. [Tacconi et al. 2013](#)).

There exists an important cycling process between phases for the gas in the ISM, which is shown as a cartoon in [Figure 2.1](#). The cycle is explained in its captions, but a brief overview is given here. The ionised phase contains material heated up primarily by supernovae and radiation from massive stars (so called HII-regions), which is most prominent around star forming regions of young stars. This is because the gas around newly born stars has yet to cool down, but it will inevitably do so through spontaneously emitting radiation. Eventually, it will be cold enough for the ionised gas to recombine with electrons and enter the neutral phase. Further cooling then recovers the molecular phase, in the manner explained previously. An additional visual aid for this is the phase plot seen in [Figure 2.2](#), which shows temperature plotted against density and highlights the cyclic transition from cold dense gas to hot diffuse gas. More detail is given in its captions. Additionally, the phase plots contain a visual of the temperature cuts done in this project to evaluate different phases of the ISM, which will become relevant during the analysis, [Section 3.3.3](#).

2.1.1 The Turbulent ISM

As previously mentioned in the introduction, the ISM has been observed to be supersonically turbulent over many different galaxies for a large variety of scales and redshifts. This is also true for different observational tracers; the 21 cm line of H I ([van Zee & Bryant 1999](#); [Petric & Rupen 2007](#); [Tamburro et al. 2009](#); [Ianjamasimanana et al. 2012, 2015](#); [Stilp et al. 2013](#); [Chepurnov et al. 2015](#)), the low-level rotational transition lines of CO ([Caldú-Primo et al. 2013, 2015](#); [Meidt et al. 2013](#)) and recombination lines of ionised gas ([Cresci et al. 2009](#); [Lehnert et al. 2009, 2013](#); [Green et al. 2014](#); [Le Tiran et al. 2011](#); [Genzel et al. 2014](#); [Moiseev et al. 2015](#)). However, the level of observed turbulence, as quantified by the gas

velocity dispersion σ , still changes with the observed scale and tracer used.

There have been several suggested origins of this turbulence. For example, magnetic fields, shear from rotation, gravitational instabilities and stellar feedback (see e.g. [Mac Low & Klessen 2004](#), and references therein). Thermal broadening is not able to explain the observed line widths, as it only accounts for, at most, $\sigma \sim 10 \text{ km s}^{-1}$ (e.g. [Chu & Kennicutt 1994](#)). There is also the requirement of maintaining this turbulence over an extended amount of time. At a minimum, the energy has to be globally (on average) injected at the same rate as it is dissipated. Other properties, such as the environment, may also play a part in how much the proposed sources contribute to the turbulent motions.

One of the pioneers in investigating interstellar turbulence was [Larson \(1981\)](#), who was able to derive an empirical power law for the velocity dispersion in a molecular cloud as a function of either radius or mass. This indicates that turbulence can affect the properties of molecular clouds and, in extent, the galaxy. Additionally, turbulence can readily be understood to affect the distribution of gas densities through compressing and rarefaction motions; shocks originating from the random turbulent motion increases the density in some regions while decreasing it other regions. This is known as the probability density function (PDF) and is set by the level of turbulence in a galaxy ([Salim et al. 2015](#)), meaning that an increased turbulence extends the available gas densities to higher and lower values. This has a key effect on star formation, which is observed to increase with the amount of turbulence and can be intuitively understood from the increased densities promoted by a wider distribution function; the increased density of a cloud makes it more probable to collapse to form stars. A more direct consequence is its role in mixing material (e.g. heavy metals from stellar ejecta) in the disc.

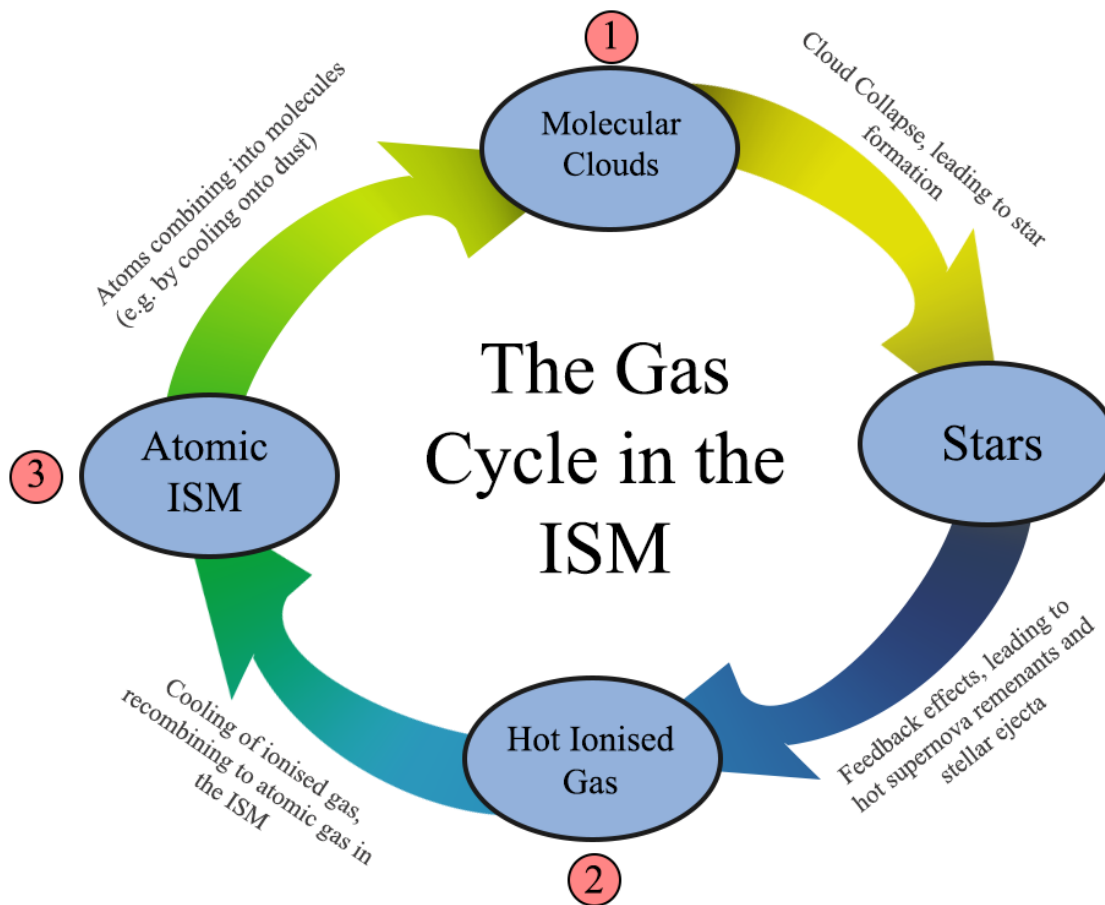


Figure 2.1: A cartoon illustrating the ISM gas cycle in a few simple steps, starting at the top and following the arrows the steps go as follows: As mentioned in the introduction, stars form from molecular clouds. After some time, these stars affect the ISM through stellar feedback effects, such as supernovae (more thoroughly explained in Section 2.3). This heats up the gas, which in turn excites the atom and likely ionises it, creating the ionised gas phase. Subsequent cooling occurs through radiative cooling, free-free emission, until the ionised gas can recombine into neutral atoms, followed by formation of molecular hydrogen on dust particles. The numbers shown correspond to the numbers in Figure 2.2, which illustrates the transitions between the phases and the colouring seen there corresponds to the colours here.

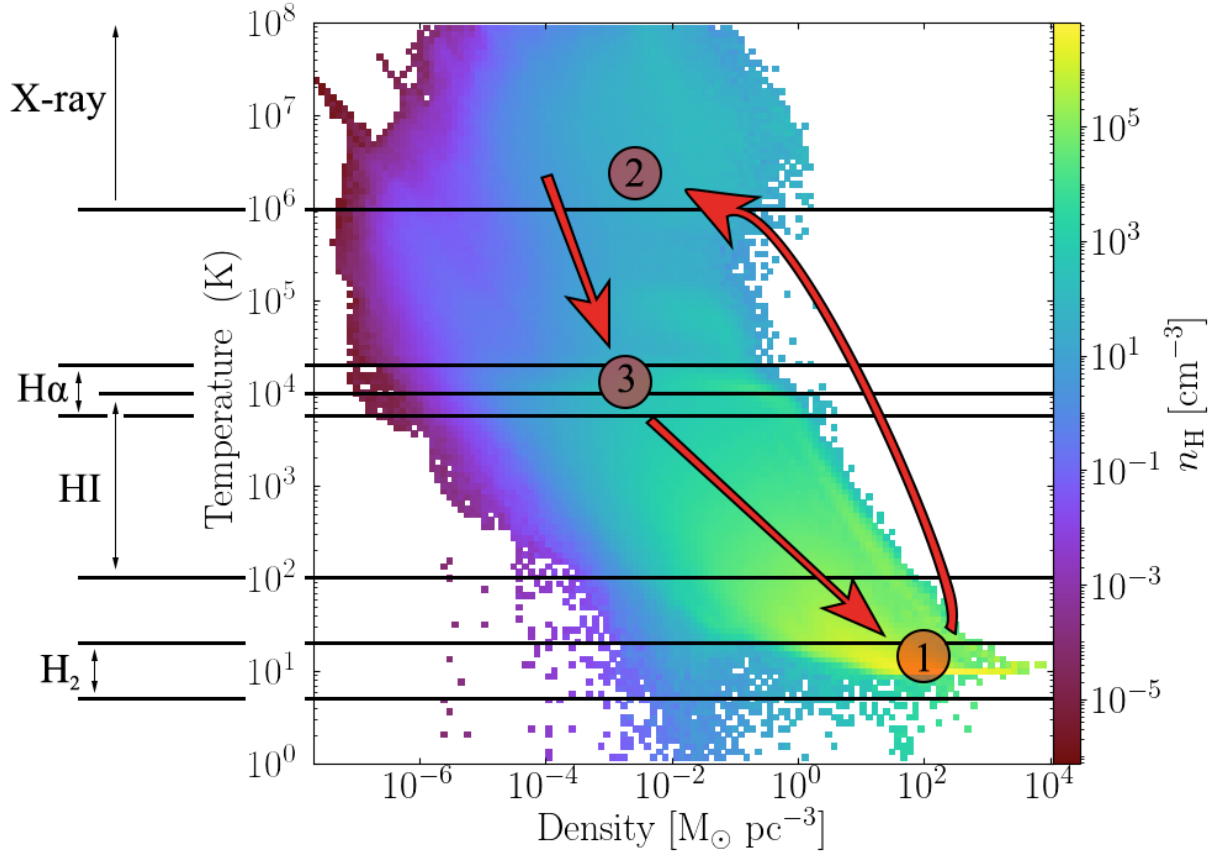


Figure 2.2: A phase plot of the ISM, showing temperature against density, with arrows and numbers to highlight the continually ongoing gas cycle. Furthermore, I have also included lines that mark the temperature cuts used in (parts of) this project to approximate the different gas phases (e.g. molecular H_2 at 5 - 20 K). The colouring is based on the number density of hydrogen, n_{H} . The values shown here have been calculated from one of the galaxy simulations, `fg50_FB`, during its starburst period (195 Myr simulation time). The characteristics of the simulation is laid out in Table 3.2 and further explained in Section 3.2.1. This plot goes together with Figure 2.1, to illustrate how the phase changes between three major phases: At **1** cold dense gas (molecular clouds) quickly becomes part of the hot and diffuse state at **2** from stars forming and undergoing supernova that heat up the surrounding gas. This phase would not be present on this diagram without these feedback effects. The ionised gas then gradually cools until it recombines into atoms at **3** and eventually molecules, renewing the gas supply for star formation, at **1**.

2.2 Star formation

The formation of stars is a very important aspect of galaxy formation, however, the precise conditions, both locally and globally, are not yet well understood. Stars form in the ISM from giant molecular clouds, where the sub-structures in the clouds form gravitationally bound cores of molecular gas. These will become gravitationally unstable as they become more dense and eventually these cores collapse to form stars (Megeath et al. 2016). The stars forming from an individual molecular cloud, in the same event, will presumably form stars according to some distribution of stellar masses and follow the canonical initial mass distribution (IMF; Kroupa 2002; Chabrier 2003; Bastian et al. 2010).

The starburst of local galaxies is mainly attributed to galaxy interactions and mergers (e.g. Sanders & Mirabel 1996), while high redshift galaxies typically have both higher merger rates and gas fractions which allow for higher rates of star formation; related to the observed clumping of gas at these high redshifts (Agertz et al. 2009). Notably, the star formation rate (SFR) of a starburst galaxy is around an order of magnitude larger than that of a typical local isolated disc galaxy (Saintonge et al. 2012). Constraints on the average star formation in galaxies suggest that most galaxies had their peak SFR at a redshift of $z \sim 2$ (e.g. Behroozi et al. 2013). In this project, I explore both local and high-redshift, isolated, galaxies in my simulations.

By investigating the star formation of the Milky Way, Schmidt (1959) found that, in a given region, the star formation surface (or column) density and molecular & neutral hydrogen gas surface density follow a simple power law (see Schaye & Dalla Vecchia 2008, for a recent review). Kennicutt (1998) analysed this relationship further by looking at local star forming galaxies and confirmed that this law was applicable to other galaxies. This law is therefore commonly referred to as either the Schmidt or Kennicutt-Schmidt (KS) law and simply states

$$\dot{\Sigma}_* \propto \Sigma_g^N, \quad (2.1)$$

where $\dot{\Sigma}_*$ is the star formation rate surface density and Σ_g is the surface density of the gas. The quantities are usually expressed in the units $M_\odot \text{ yr}^{-1} \text{ pc}^{-2}$, for the star formation surface density, and $M_\odot \text{ kpc}^{-2}$, for the gas surface density. The index N has been found to assume values $N = 1.0 \pm 0.2$ (Bigiel et al. 2008) for local galaxies, when using atomic and molecular hydrogen as tracers. Kennicutt (1998) investigated starburst galaxies observed from different tracers and found that these galaxies follow the law for a larger index, $N = 1.4 \pm 0.15$. This higher index can then be understood to be related to how much of the gas is turned into stars, reminiscent of a star formation efficiency. Therefore, there is a clear distinction that can be made between different galaxies for this relation. In section 4.1.4, I will get back to this property and explain why this is a crucial benchmark for my simulations.

The globally-averaged efficiency of star formation in galaxies has been found to be very low (around a few percent), leading to the conclusion that galaxy formation in itself is a very inefficient process. The value derived is somewhat dependent on the actual scale and region where one observes, as measurements of local giant molecular clouds regions have

been found to be close to unity in some cases (Lada et al. 2010; Murray 2011; Evans et al. 2014).

2.3 Stellar Feedback

After stars have formed, they take an active part in galactic properties; affecting its environment through different feedback effects. For example, the continuous radiation of photons is absorbed by dust and gas, imparting its energy and momentum into the ISM and is particularly important in young massive stars. The stellar winds from stars also inject energy and momentum, but does so via ejection of material. These winds contain heavy metals produced in the centre of stars (surfaced through convection) and enrich the ISM. Finally, there is the explosion of stars, supernovae (SNe), which effect the ISM in the same manner as stellar winds, but are able to eject more energy, momentum and much heavier elements. The energy involved in such an explosion is of the order 10^{51} ergs, ejecting mass of $m \sim 10 M_{\odot}$ at speeds on the order of $v \sim 5000 \text{ km s}^{-1}$. The formation and impact of the more common SNe types (type II and type Ia) are what is mainly discussed in this section, as they are implemented into my simulations (see Section 3.1.3).

Core-collapse SNe are denoted as Type II and happen when stars $m > 8M_{\odot}$ reach the end of their life of fusing elements. The star has an iron-nickle core which becomes inert and steadily contracts, eventually collapsing with the aid of photodissociation in the core. This ends with the star becoming a degenerate neutron star and expelling a variety of materials, notably some elements heavier than iron. Type Ia SNe results in the same outcome, but is caused when a white dwarf accumulates mass until it reaches the Chandrasekhar limit of $m = 1.44 M_{\odot}$. This mass usually comes from a companion star that has swelled up into a red giant. With a standard Kroupa or Chabrier IMF, an average SN ejects mass of the order $m \sim 10 M_{\odot}$ and one SN occurs roughly every $100 M_{\odot}$ star mass formed (Kroupa 2002; Chabrier 2003).

McKee & Ostriker (1977) hypothesised that the material coming from SNe acts to self-regulate the star formation in galaxies by disturbing the molecular clouds by ‘tearing away’ the gas from the cloud cores. However, it is also possible that it can enhance star formation through the same effect; by perturbing molecular cloud cores on the verge of gravitational collapse and make them unstable. As mentioned above, stellar feedback, such as SNe, heat up the surrounding gas to temperature of $T > 10^6 \text{ K}$, which forms the hot ionised phase and severely affects the warm ionised phase $T \sim 10^4 \text{ K}$. In particular, SNe heat up the gas through shock waves, as the high velocity ejecta interacts with the surrounding gas of the ISM. These very large temperatures are not attainable through disc dynamics, e.g. cloud collision and shear occurring in other phases. Clearly, SNe have a big impact on the phases in the ISM as well as its kinematics. This knowledge is important going forward, as I have adjusted the feedback in my simulations, which makes this important to understand its possible impact. This will be further discussed in Section 3.2 and onward.

Using numerical simulations, Agertz et al. (2013) investigated, among other things, the relevance of the three different feedback effects throughout a galaxy’s lifetime. The energy

and momentum outputs from radiation pressure was found to be dominant at very early times, but this changed relatively quickly as stellar winds became prominent. While not every star undergoes SNe, the specific momentum input of one SN ($P_*/m_* \approx 3000 \text{ km s}^{-1}$), is significantly larger than that of radiation and stellar winds. Therefore, SNe quickly became the most dominant feedback process not long after the occurrence of the first SN, $\Delta t \sim 3 - 40 \text{ Myr}$, which is the lifetime of the massive OB stars. After this, the amount of SNe forming was sufficient to remain the most impacting of the three feedback effects discussed.

2.4 Observational data

In this section, I present a list of compiled data from literature sources and discuss relevant observational parameters. This data includes star formation rates and velocity dispersions of a variety of galaxies and are used for comparisons with my simulations. However, in order to draw accurate conclusions about the correlation between observational data and simulations, the origin and handling of the data needs to be carefully considered, which is explained in this section. The data references are shown in Table 2.1, along with relevant information about the approximate beam sizes (some papers only mention using sub-kpc or kpc scale), redshift (local or high-redshift, z) and whether the observed angle (inclination) of the galaxy was considered. An important aspect of the data is that due to the large variety in observational parameters, it is not homogeneous; which can lead to confusion when comparing the data. Furthermore, there are various types of disc galaxies (e.g. normal, dwarf, merger) and galactic properties (e.g. mass, morphology), which vary between data and may effect the gas turbulence and star formation of the disc. In this project, I evaluate the impact of these observational parameters, but do not go into any detailed analysis of disc galaxy types or properties.

To better understand how the data is applied, it is useful to mention how the phases are observed and what kind of limitations certain gas tracers suffer. The molecular (hydrogen) phase is inferred from the absorption of the $J: 2 \rightarrow 0$ rotational transition in the CO molecule, as this molecule is common on the dust around molecular clouds. This transition is very weak and therefore mainly observed locally (e.g. Caldú-Primo et al. 2015). The same goes for neutral hydrogen H α , which is found by its characteristic 21 cm line, originating from a change in spin orientation (Krumholz 2015). Furthermore, most of the data compiled in this table uses the Balmer-alpha (also known as H α) transition (mainly $3p \rightarrow 2s$) as a tracer. The reason this is a common tracer for these galaxies is that its flux is related to star formation (through an empirical law), but also since it is relatively opaque; in the far red spectrum with a wavelength of $\lambda = 6564 \text{ \AA}$. This transition as a gas tracer for the warm ionised medium is more thoroughly explored in my analysis, explained in Section 3.3.3.

In the table, the literature data has also been assigned specific plot markers, which are used repeatedly throughout the project whenever that specific data is plotted. To note is that observational data is observed in grids and the beam size mentioned here is their grid

resolution, which is not identical to the beam size used during my analysis (see Section 3.3 for how I define my beams), but they are still possible to compare directly.

2.4.1 Observational Effects

The velocity dispersion of any tracer is usually evaluated by looking at the line width of spectral lines, using telescopes with the observational view of a cone or beam. Systematic effects which affect the width of the observed spectral line are then referred to as ‘‘beam smearing’’. A beam-smearred velocity gradient affects the velocity dispersion by increasing the range of velocities, which then broadens the line width due to Doppler shift. For a resolved galaxy, there are multiple ways in which the overall velocity dispersion can be evaluated, but it is usually set as the flux-weighted mean of each beam. Di Teodoro et al. (2016) suggested that this type of averaging favours the inner regions of galaxies, which have a higher flux but are also more affected by beam smearing coming from inclination, due to the larger spread of velocities around the centre. This would then yield a bias towards higher global dispersion values.

High redshift disc galaxies will evidently be more difficult to resolve properly and so they tend to be measured globally. As briefly mentioned in Section 2.1.1, the turbulence is also dependent on the scale observed, meaning higher redshift galaxies will in general have a higher velocity dispersion purely due to the spatial size of the beam being larger at those redshifts. Furthermore, for these type of galaxies, Epinat et al. (2009) showed that if they are heavily affected by beam smearing, then the inclination is difficult to retrieve and to account for it. As such, I will return to analysing the impact of beam smearing on the velocity dispersion in Section 4.2.1, where I demonstrate how even small inclinations can significantly affect the observed dispersion. In the same section I also look at the impact of beam sizes and tracers.

There have been several methods to account for beam smearing of the velocity field. Assuming a typical shape of the observed galaxy and fitting that to the observed shape can yield a rough estimate on the inclination of the disc (this is done by e.g. GALFIT; Peng et al. 2002). Another method is to use the tilted ring method (e.g. Epinat et al. 2009), which applies data cubes to construct a 3D map of the galaxy. This method can also reconstruct more than just the velocity field of the galaxy, e.g. the surface density distribution.

2.5 Toomre’s Q stability criterion

As gravitational instability is believed to hold a key part in driving gas turbulence (Krumholz & Burkhardt 2016), it is important to carefully consider a theoretical framework to evaluate this instability. One of the most common ways of quantifying this instability is Toomre’s Q, which governs the stability of a smaller patch inside a disc system, applicable for both galactic and planetary discs. Toomre’s Q parameter was first derived by Safronov (1960), but got its name after Toomre (1964), in which Toomre derived and presented this param-

eter in a more general and comprehensive way. The relation was initially derived for an axisymmetric, flat disc with a continuous distribution of particles and with differential rotation. However, it is just as easily derived for a fluid disc, resulting in only a small change in constants. A conceptual derivation is presented below, to give a better understanding of where this tool come froms, and I'd recommend to see e.g. [Binney & Tremaine \(1987\)](#) for a more detailed view of the derivation.

Beyond the straight forward limit of $Q = 1$, where the disc is on the threshold of stability, values of $Q \sim 2 - 3$ is the limit for marginal stability. This criterion has been explained as accounting for non-axisymmetric effects not present in the derivation of the Toomre parameter. For example, the dense arms of a spiral galaxy will offset the condition of stability by encouraging collapse in the disc (e.g. [Binney & Tremaine 1987](#)).

2.5.1 Conceptual Derivation

In [Section 5.3](#), I will study the relation between Q and σ in great detail, warranting a careful description in this section. Here, I give a basic idea of the derivation of Toomre's Q , see e.g. [Binney & Tremaine \(1987\)](#) for its full derivation. In contrast, an informed reader may skip forward to the next subsection.

The Toomre parameter for an axisymmetric, fluid disc with a differential rotation, can be determined by analysing the response of the disc to a small perturbation, which makes the disc contract. This perturbation is driven by gravity, expressed as a surface density wave function with an exponential decline with the angular frequency ω ,

$$\Sigma(\omega, t) \propto e^{-i\omega t}, \quad (2.2)$$

where k is the wavenumber, x is the position and t is the time. The important concept here is that if ω would attain an imaginary value, the spectrum would start increasing exponentially and result in very high densities, which would force the disc to collapse. Here, I will simply use the dispersion relation derived for ω ,

$$\omega^2 = \kappa^2 - 2\pi G \Sigma_0 |k| + \sigma^2 k^2, \quad (2.3)$$

without going into any detail how it is derived and instead try to give an intuitive understanding of each term. In this equation, k is the wave number, κ is the epicyclic frequency, Σ_0 is the surface density, σ is the velocity dispersion and G is the gravitational constant. Furthermore, the different components of this equation can be identified: $+\kappa^2$ can be thought of as the rotational support from collapse, $+\sigma^2 k^2$ is the pressure support from collapse and $-2\pi G \Sigma_0 |k|$ is the gravitational forces driving instability.

Evidently, ω becomes a way to determine the stability of the disc at a particular wavenumber. The disc is stable for $\omega^2 > 0$ and unstable when $\omega^2 < 0$, as this results in an imaginary number and causing an exponential growth. By evaluating the dispersion relation at $\omega = 0$ (the marginal instability for the fluid), the disc is unstable as long as there are no positive solutions for k . This condition then yields

$$Q_g \equiv \frac{\kappa \sigma_g}{\pi G \Sigma_g}, \quad (2.4)$$

where $Q_g < 1$ is locally unstable. The above method can be expanded to a disc filled with star particles and differ only slightly from the approach of a fluid,

$$Q_* = \frac{\kappa\sigma_*}{3.36G\Sigma_*}. \quad (2.5)$$

2.5.2 Stability of multi-component discs

Combining the Toomre parameters, for e.g. stars and gas, is a necessary step to determine the stability of a multi-component disc, which is the case for most galaxies. To keep in mind here is that the combined Q is derived to also obey the instability criterion of $Q \sim 1$. There have been several different approaches to combining Q parameters and an extensive look into different methods was done by [Romeo & Falstad \(2013\)](#). They found that the commonly used [Wang & Silk \(1994\)](#) approximation,

$$\frac{1}{Q_{\text{WS}}} = \frac{1}{Q_g} + \frac{1}{Q_*} \quad (2.6)$$

gave errors upwards of 40% the actual value. This approximation is a direct combination of the Q parameter, which effectively assumes that both components contribute an equal amount to the stability and only remaining valid when $\sigma_g \approx \sigma_*$. A more accurate recipe for combining Q -parameters was presented in [Romeo & Wiegert \(2011\)](#),

$$\frac{1}{Q_{\text{RW}}} = \begin{cases} \frac{W}{Q_*} + \frac{1}{Q_g} & \text{if } Q_* \geq Q_g, \\ \frac{1}{Q_*} + \frac{W}{Q_g} & \text{if } Q_* \leq Q_g; \end{cases} \quad (2.7)$$

which accounted for the difference in dynamics of the components through a weight,

$$W = \frac{2\sigma_*\sigma_g}{\sigma_*^2 + \sigma_g^2}. \quad (2.8)$$

Furthermore, [Romeo & Wiegert \(2011\)](#) also derived a combined Q parameter for a two-component disc, but allowed the disc of stars and gas to have a thickness. This was primarily meant to account for the thickness of the gaseous disc. They give the following recipe:

$$\frac{1}{Q_{\text{RW}}} = \begin{cases} \frac{W}{T_*Q_*} + \frac{1}{T_gQ_g} & \text{if } T_*Q_* \geq T_gQ_g, \\ \frac{1}{T_*Q_*} + \frac{W}{T_gQ_g} & \text{if } T_*Q_* \leq T_gQ_g; \end{cases} \quad (2.9)$$

$$T = \begin{cases} 1 + 0.6 \left(\frac{\sigma_z}{\sigma_R}\right)^2 & \text{for } 0 \leq \sigma_z/\sigma_R \leq 0.5, \\ 0.8 + 0.7 \left(\frac{\sigma_z}{\sigma_R}\right) & \text{for } 0.5 \leq \sigma_z/\sigma_R \leq 1. \end{cases} \quad (2.10)$$

The thin disc approximation can be recovered simply by setting $\sigma_z = 0$. An important thing to note, and keep in mind, here is that the condition $T_*Q_* \leq T_gQ_g$ states that stars are dominating the instability (and vice-versa), since the component with the smallest value drives the instability. This is important for differentiating between star- or gas-driven instability regimes. I will return to these regimes, but also elaborate on the role of disc stability to predict the observed σ , in Section 5.3.

Romeo & Falstad (2013) expanded upon this derivation and presented a general equation for the combination of an arbitrary amount of components, while also accounting for their vertical thickness. As an aside, the larger limits ($0.5 \leq \sigma_z/\sigma_R \leq 1$) in Eq.2.10 were taken from their article.

2.6 Analytic Models

Comparisons between observational data and predictions from analytic models are very useful, as they give a way to interpret observed relations. The key relation that is investigated in this project is between turbulence, quantified as velocity dispersion σ , and the star formation rate (SFR). By applying models derived using different sources of energy injection, they can hopefully be separated and evaluated to determine which model best explains the observed link between σ and SFR.

I here focus on the analytic equations used in Krumholz & Burkhardt (2016, the specific models are described in detail below), which were modelled after gravitational instability (GI) and feedback (FB). These gas turbulence origins are popular in literature, and therefore of interest to investigate. However, these models have never been properly tested against simulations, other than direct comparisons with data, where the heterogeneity of the data is often not considered. Notably, there are some assumptions made in the models which are questionable and need to be evaluated, as I will mention in the coming section but detail in Section 5.1.

2.6.1 Gravitational Instability Model

To evaluate the possible effects of gravitational instability (GI), the analytic model derived by Krumholz & Burkert (2010, hereafter KB10) for a steady-state disc is used. The derivation of this model uses the Navier-Stokes equations, which govern the properties of a fluid, and assumes an axisymmetric fluid disc which is marginally stable with time; i.e. a steady state. The entire disc is therefore assumed to always be on the verge of gravitational collapse, a quasi-stable state, which is equivalent to having a Toomre parameter of $Q \sim 1$. The idea behind this model driving a galaxy-scale turbulence σ_z is that the disc will, at some point, slightly dip under the Toomre condition for a stable disc, contract and turn potential energy into turbulent energy, which would stabilise the disc to $Q \gtrsim 1$. This is equivalent to a radial transport of mass through the disc, which would on average have a mass flux inwards (as detailed in Krumholz et al. 2018). Finally, any feedback effects are neglected in this model.

The model predicts the surface gas density Σ_{GI} and turbulence σ_{GI} within some radius r . Expressions for these quantities are given as

$$\Sigma_{\text{GI}} = \frac{v_c}{\pi G Q r} \left(\frac{f_g^2 G \dot{M}}{\eta} \right)^{1/3} \quad (2.11)$$

$$\sigma_{\text{GI}} = \frac{1}{\sqrt{2}} \left(\frac{G \dot{M}}{\eta f_g} \right)^{1/3}, \quad (2.12)$$

in which the mass accretion rate \dot{M} is a free parameter and η (a factor for the dissipation rate of turbulent energy) is of order unity. The gas fraction and circular velocity are denoted f_g and v_c , respectively. These equations were derived with high-redshift galaxies in mind, which, according to KB16, implies $\sigma_* \approx \sigma_g$. The reasoning is that stars have yet to differentiate themselves from the gas clouds this is also the case at the outer parts of local galaxies. An important thing to note is that they use the Q_{WS} approximation and a flat rotation curve $\Omega = \sqrt{2}v_c$ and re-write it for the velocity dispersion

$$\sigma_{\text{GI}} \approx \frac{\pi G r \Sigma Q}{\sqrt{2} v_c f_g}. \quad (2.13)$$

As mentioned in Section 2.5.2, this approximation can be quite inaccurate and this is further investigated in Section 5.3.

When presenting this model, KB16 uses the assumption that the whole disc is filled with molecular hydrogen and, therefore, star formation is not limited to spiral arms. This is referred to as the “Toomre regime” (e.g. Krumholz et al. 2012), which is viable for high-redshift galaxies. This assumption allows a free-fall time (the timescale of unhindered radial gravitational collapse) to be calculated from the mid-plane pressure density, as opposed by the density of a molecular cloud. This has the form

$$t_{\text{ff}} = \sqrt{\frac{3}{2\phi_{\text{P}}}} \left(\frac{\pi Q r}{4 f_g v_c} \right), \quad (2.14)$$

where $\phi_{\text{P}} \approx 3$ accounts for the presence of stars. By integrating over the entire disc using these variables, KB16 derives a global SFR- σ_g relation,

$$\dot{M}_{*,\text{GI}} = \int_{r_0}^{r_1} 2\pi r \epsilon_{\text{ff}} \frac{\Sigma}{t_{\text{ff}}} dr = \frac{16}{\pi} \sqrt{\frac{\phi_{\text{P}}}{3}} \left(\frac{\epsilon_{\text{ff}} v_c^2}{G} \ln \frac{r_1}{r_0} \right) \frac{1}{Q^2} f_g^2 \sigma. \quad (2.15)$$

2.6.2 Feedback Model

The feedback-driven turbulence model presented here (Faucher-Giguère et al. 2013, hereafter FQH13), was derived focusing on galaxies with high gas surface densities, allowing for plenty of molecular gas to form stars from, similar to the “Toomre regime”. This simplifies the approach by avoiding explicit consideration of a multi-phase ISM. Given how important the gas cycle is, explained in Section 2.1, this approximation may prove crucial.

The model is based on a hydrostatic equilibrium; i.e. the balancing of gravity and the momentum input from gas ejected by massive star in different feedback processes, most notably SNe. This model then determines a galaxy-averaged star formation rate density,

$$\dot{\Sigma}_{*,\text{FB}} = \frac{2\sqrt{2}\pi G Q_g \phi}{F} \left(\frac{P_*}{m_*} \right)^{-1} \Sigma^2. \quad (2.16)$$

where $\phi \approx 1$, $F \approx 2$ are constants that are supposed to cover uncertainties in how much energy actually enters the ISM, e.g. some energy may be lost to vertical outflows. The exact values shown here are the ones recommended by FQH13. As already mentioned, P_*/m_* is the momentum injection per unit mass of stars formed, with a typical value of 3000 km s^{-1} . Furthermore, KB16 argued the model requires $Q_g \sim 1$ since star formation only occurs when the molecular clouds fragment and collapse and the model requires star formation in order to inject energy from stellar feedback effects. The Toomre-based velocity dispersion is the same as for the GI-driven model Eq. 2.13,

















$$\sigma_{\text{FB}} = \frac{\pi G r \Sigma Q_g}{\sqrt{2} v_c}, \quad (2.17)$$

but without f_g and using Q_g (as the other model considers both gas and stars). The difference comes from them assuming $Q_{\text{WS}} = Q \approx 1$. KB16 combined these equations and integrated over the galactic radius, to deduce the globally-averaged model σ_g -SFR relation,

$$\dot{M}_{*,\text{FB}} = \int_{r_0}^{r_1} 2\pi r \dot{\Sigma}_* dr = \frac{8\sqrt{2}\phi v_c^2}{G Q_g F} \left(\ln \frac{r_1}{r_0} \right) \left(\frac{P_*}{m_*} \right)^{-1} \sigma^2. \quad (2.18)$$

The σ_g -SFR relation for both of these models are plotted in Figure 5.1. In the corresponding section, Section 5.1, I will scrutinise these models to understand to what degree they describe the state of actual galaxies.

Table 2.1: The complete literature library for the data used involving SFR and σ . This table relates each reference to a marker, which are used throughout the project when plotting the quantities from that reference. To note is that most of the beam sizes and redshifts are very approximate, e.g. [Alcorn et al. \(2018\)](#) analysed samples of entire dwarf galaxies with a variety of sizes. Galaxies noted with a redshift ‘local’ were observed at redshifts much smaller than 1, but the precise redshift is usually not specified in their source. The data of this table is very heterogeneous, i.e. the observations are of different types of disc galaxies (e.g. normal, dwarf, merged galaxies) with different properties (e.g. mass, morphology). This is explained in Section 2.4, and its implications are discussed in the Summary, Chapter 6.

Reference name	Survey/ Tool	Tracer	Beam sizes	Redshift	Inclination corrected	Mark
Alcorn et al. (2018)	ZFIRE	H α	2 – 4 kpc	2 – 2.5	Yes	
Cresci et al. (2009)	SINFONI/SINS	H α	\sim kpc	2	Yes	
Di Teodoro et al. (2016)	KMOS	H α	6 kpc	1	Yes	
Epinat et al. (2008)	GHASP	H α	\sim sub-kpc	Local	Yes	
Epinat et al. (2009)	SINFONI	H α	\sim kpc	1.2 – 1.6	Yes	
Genzel et al. (2011)	SINS	H α	2 kpc	2	Yes	
Ianjamasimanana et al. (2012)	THINGS	HI	\sim sub-kpc	Local	Yes	
Compiled by Krumholz et al. (2018)	SIMBAD	CO/HCN	\sim sub-kpc	Local	No	
Law et al. (2009)	Keck/OSIRIS	H α , [OIII]	1 kpc	2 – 3	No	
Lehnert et al. (2013)	SINFONI	H α , [NII]	5 – 9 kpc	1 – 3	No	
Lemoine-Busserolle et al. (2010)	VLT/ SINFONI	UV (H β / [OIII])	3.5–5 kpc	3	Yes	
Moiseev et al. (2015)	6-m tele. SAO RAS	H α	\sim sub-kpc	Local	No	
Patrício et al. (2018)	MUSE	[OII]	\sim sub-kpc	0.6 – 1.5	Yes	
Stilp et al. (2013)	THINGS/VLA-ANGST	HI	0.2 kpc	Local	Yes	
Varidel et al. (2016)	SDSS	H α	\sim sub-kpc	Local	Yes	
Wisnioski et al. (2011)	WiggleZ	UV, [OII]	0.4 kpc	1.3	No	

Chapter 3

Method

With the necessary theory outlined in Chapter 2, this Chapter focuses on the approach for simulating a galactic disc with the adaptive-mesh, hydrodynamical+N-body code RAMSES. I begin by giving a detailed explanation of what the RAMSES code does, e.g. the equations it solves for, some key numerical methods and the refinement strategy applied to the simulation volumes to efficiently refine the simulation. These explanations are here in order to build an understanding of how the code works, but also to motivate its validity. Building on that, the implementation of star formation and feedback are also discussed in great detail, as these physical effects are not present in the source code of RAMSES. Next I outline the suite used for the galaxy simulations, which includes, e.g. the galactic potentials used, the initial conditions of the galaxy and other important specifics of the runs.

For the analysis part, I present how I calculate relevant quantities from the simulation data. I also detail my approach for considering different observational parameters; beam size, galaxy inclination and gas tracer. The latter was evaluated using two completely different approaches, which are compared in the Results, Chapter 4.

3.1 RAMSES

RAMSES (Teyssier 2002) is a grid-based adaptive mesh refinement (AMR) code, created to calculate N-body and/or hydrodynamical systems. In the code, dark matter and stars are treated as collisionless particles, while the gas follows the fluid dynamics of an ideal mono-atomic gas, which has an adiabatic index of $\gamma = 5/3$. The particle interactions are calculated using a particle mesh method, based on a “quasi-Lagrangian” approach, in which the mesh structure is formed by trying to keep the number of particles constant in each cell (at least 1 per cell). The fluid properties are calculated on the grid and follow

the Eulerian equations in their conservative form:

$$\frac{\partial \rho}{\partial t} + \nabla \cdot (\rho \mathbf{u}) = 0 \quad (3.1)$$

$$\frac{\partial}{\partial t}(\rho \mathbf{u}) + \nabla \cdot (\rho \mathbf{u} \otimes \mathbf{u}) + \nabla p = -\rho \nabla \phi \quad (3.2)$$

$$\frac{\partial}{\partial t}(\rho e) + \nabla \cdot [\rho \mathbf{u}(e + p/\rho)] = -\rho \mathbf{u} \cdot \nabla \phi. \quad (3.3)$$

These equations govern the important properties of a fluid, which are: the thermal pressure p , mass density ρ and the fluid velocity \mathbf{u} . The equations are derived to conserve quantities such as the mass, momentum, $\rho \mathbf{u}$, and specific total energy e . Gravitational effects, both external and self-gravity, come into effect through the source terms as the potential ϕ , which in turn is solved through the Poisson equation,

$$\nabla^2 \phi = 4\pi G \rho. \quad (3.4)$$

RAMSES solves these differential equations using a single-grid Godunov scheme for finite volumes, where it applies a second order Riemann solver using the boundary conditions from the surrounding grid cells. The solver yields the fluxes of the gas along the grid cells. The total gravitational interaction is assessed for each grid cell, at each time step, by first determining the mass density in each cell from the fluid parameters and the particles. The latter is evaluated using a cloud-in-cell interpolation (see e.g. [Hockney & Eastwood 1981](#)), which effectively smears out the particle density as a homogeneous, cubical ‘cloud’ and calculates the density within a grid from the cloud volume it encompasses. Then, the potential can be derived from the density by integrating the Poisson equation, which yields the gravitational acceleration of each particle and the fluid. RAMSES uses a first-order linear approximation to calculate an initial guess for the acceleration induced by far-away objects, only considering their coarse structure, while local cells are further corrected later on. With the acceleration known, the new velocity of each particle is set and then their positions are updated accordingly.

3.1.1 Refinement Strategy

The mesh in RAMSES is a hierarchy of nested grid cells, where the spatial scales are related to their level of refinement. To get an intuitive understanding of how this works, the projected density of a dense molecular cloud has been plotted in [Figure 3.1](#), with the AMR grid superposed on this. More information is given in its captions.

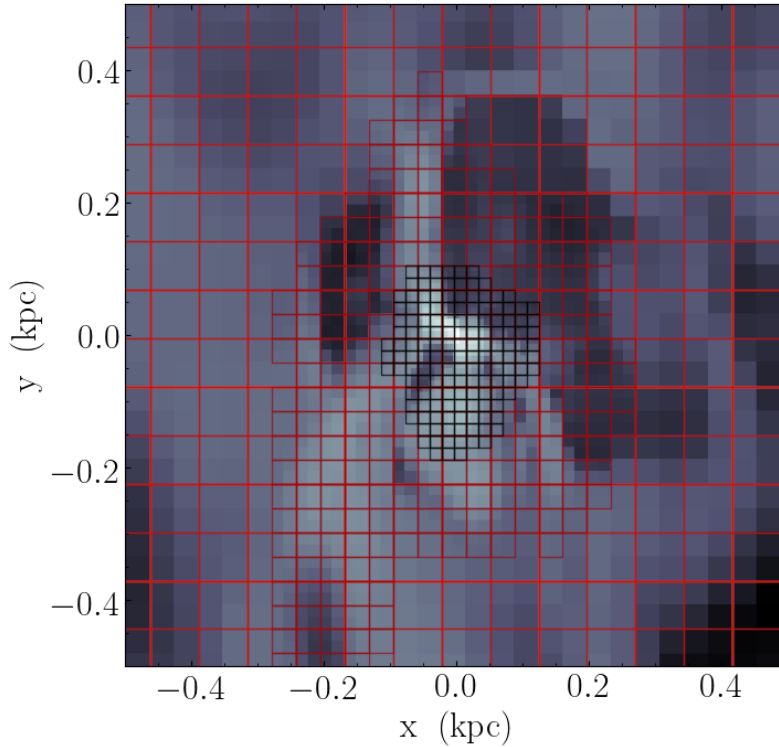


Figure 3.1: An example of the refinement levels in the AMR grid applied in RAMSES. The figure is of a projected density, where the brighter the grid cell, the higher the density. A dense gas clump can be seen as a white spot in the centre of the figure. This is a zoom-in of a dense molecular cloud in the `fg10_noFB` galaxy. This clump is located 5 kpc from the centre and the axes denote the relative distance from the centre of this image; i.e. the distance from the clump. The size of this clump is around $\Delta x \approx 60$ pc. As mentioned in Section 3.1.1, since this clump is more dense than its surrounding area, it is better resolved; the black grid around the clump has a smaller grid than the red grid, in particular at the edges of this figure.

When a cell of a certain refinement level (noted ℓ) is refined, it is split into two equally-sized halves in each dimension with refinement levels $\ell + 1$. For example, in the 3-dimensional case, one cube (parent cell) is split into eight smaller cubes (child cells). These grid elements are categorised as octs, which are the cells with the same parent cell and level of refinement. The pre-defined conditions used for refinement are derived from: the particle mesh (keeping the number of particles in a cell close to 1) and smooth transitions in spatial scale between grid cells. The latter is done when refining a specific cell, then the neighbouring cells are also marked for refinement. The primary user-defined refinement condition applied in these simulations is on the mass within a grid. The actual value on the limit can be chosen arbitrarily, as the key point is to resolve the fragmentation of dense

areas.

In order to keep track of all the different grids and particles as cells are refined and de-refined, RAMSES applies a "Fully-Threaded Tree" (Khokhlov 1998) data framework to its AMR process. A linked list is used to record the address of particles within each grid. The octs are part of a double linked list, which has a tree structure where each oct remembers who their parent and child cells are, but also its neighbouring octs. By using these lists, it is much easier to understand the structure of the cells and for the code to change it; refining a grid means adding child cells to the list of a parent cell while de-refinement implies simply removing this section of the list. In the context of parallel computing, RAMSES uses a Hilbert curve to track and distribute the cells to different processors, which in essence transforms the 3D environment to a 1D list of the cell addresses.

To make use of the AMR, RAMSES first looks at the highest refinement level ℓ_{\max} , where it solves the relevant equations for each time sub-step. This continues until all refinement levels have been calculated and is done independently of refinement levels lower than the one currently evaluated. In the simulations, a variable time step is used, to avoid performing unnecessary calculations on slowly evolving regions. The time steps between adjacent refinement levels also have to be synchronised, since the equations are time-dependent. In RAMSES, this is typically done by having the time steps in multiples of two, meaning a child cell synchronises with its parent every other time step, which avoids performing time interpolations. The size of a time step in a grid is dependent on a number of constraints to ensure the stability of the solution. The maximum time step that can be used within a grid is commonly known as the Courant–Friedrichs–Lewy condition, which is based on the criteria that a particle/fluid element may not cross the entirety of a cell in one time step, as then it would practically skip a domain. However, there are more strict constraints on the size of the time steps in each grid which could be applied (Teyssier 2002).

3.1.2 Star formation on mesh

RAMSES essentially works for any system applying particle and/or gas dynamics, but to simulate disc galaxies, the code needs to be ‘patched’ with information on how to handle ongoing star formation and feedback effects, along with the structural parts of a galaxy. Following the work done by Agertz & Kravtsov (2015), I here use the same patch (supplied to me by Oscar Agertz) for star formation and stellar feedback budget, which includes their method of metal advection and momentum injection from stellar winds and SNe. These will be discussed in the coming section.

The requirement for star formation to occur in a grid cell at any given time is based on a density threshold set as the mass of a star particle $\rho_* = 10^3 M_\odot$. The star formation rate density then follows

$$\dot{\rho}_* = \frac{\rho_g}{t_{\text{SF}}} \text{ for } \rho_g > \rho_*, \quad (3.5)$$

where ρ_g is the density for molecular gas. The star formation time scale $t_{\text{SF}} = t_{\text{ff}}/\epsilon_{\text{ff}}$ is defined from the free-fall time of a spherical object of uniform density $t_{\text{ff}} = \sqrt{3\pi/32G\rho}$

and the efficiency of star formation in a free-fall event ϵ_{ff} ; set as $\epsilon_{\text{ff}} \sim 1\%$, motivated by the discussion in Section 2.2. In the local universe, $t_{\text{SF}} \sim 2$ Gyr for molecular gas (Bigiel et al. 2011).

Stars in the simulations are grouped together as star particles, assumed to represent a single stellar population with an internal IMF; in particular, the canonical Chabrier IMF (Chabrier 2003). The initial mass of a star particle is $m = 10^3 M_{\odot}$, but this mass changes as the stars shed material through stellar winds and SNe. In order for the number of star particles to remain manageable, Eq. 3.5 is sampled every fine simulation time step using a stochastic process. More specifically, a discrete Poisson distribution is used to determine the number of star particles which form at each star formation event; these are then combined into one star particle. For details, see Section 2.3 in Agertz et al. (2013).

To form molecular clouds, the dynamically heated gas needs to cool down sufficiently, which is done through using the cooling functions dependent on gas temperature. Here I use the tabulated cooling functions of Sutherland & Dopita (1993) for cooling at temperatures $T \gtrsim 10^4$ K and Rosen & Bregman (1995) for $T \lesssim 10^4$ K. The functions are dependent on metallicity content for the cooling functions, as metals aid in cooling down the gas due to having more energy transitions available in its atomic configuration, which allows efficient radiative emission.

3.1.3 Modelling stellar feedback

In these simulations, stellar feedback from SNe, winds & radiation pressure are included, according to the sub-grid model by Agertz & Kravtsov (2015). While the simulations are state-of-the-art for analysing galactic discs, the resolution used is not high enough to resolve the transfer of mass, heavy elements, energy and momentum done by stars during their feedback processes. Therefore, a subgrid implementation of the stellar feedback is used, with a SN momentum injection based on Kim & Ostriker (2015) and an empirically motivated model for radiation pressure Agertz et al. (2013). The basic idea of the subgrid model is that momentum from radiation pressure, stellar winds and SNe blast waves is added to the 26 cells neighbouring the feedback event. However, the thermal energy that comes from shocks during stellar winds and SNe is inserted directly into the host cell of the star particle, together with the ejected mass and heavy elements.

A type II SN is approximated to happen as a star ends its H- and He-burning and leaves the main sequence, since a star will rapidly go through all its subsequent burning phases. The time at which this happens, the stellar lifetimes, are determined from a fitted function dependent on mass and metallicity, given by Eq. 3 in Raiteri et al. (1996). This function is inverted to calculate the mass leaving the main sequence as a function of age and metallicity. A core-collapse SN is set to occur if the mass leaving the main-sequence in the calculated time step Δt is in the mass range $m = 8 - 40 M_{\odot}$. As for SNIa, it is assumed to happen in a binary system containing a carbon and oxygen rich white dwarf. Stellar evolution theory predicts that binary stars in the mass range $\sim 3 - 16 M_{\odot}$ will yield white dwarfs able to exceed the Chandrasekhar limit with help from their companion. Additionally, the mass loss from stellar winds is accounted for in the early life of massive

stars ($m \geq 5 M_\odot$) and the late life of low mass stars ($m < 8 M_\odot$) some time before leaving the main sequence. After each feedback event, the star particle is updated according to the mass ejected, which is, along with the metals, inserted back into the ISM.

3.2 Simulation suite of galaxies

The galaxy simulations in this project are done with RAMSES (Teyssier 2002), an N-body and hydrodynamical code which uses an adaptive mesh refinement (AMR) technique to allow for high resolution under user-specified conditions. The code uses a mesh to calculate star and gas dynamics along a set of grid cells at a time and is refined (divided into eight smaller cells) when the contained mass is eighth times a chosen mass value (here $m \sim 10^3 M_\odot$); see Section 3.1 for specifics. In this section, I will present the characteristics of the simulation runs and in the following sub-sections I will present the initial conditions and how they are derived.

The initial composition of the galaxy is done by distributing the dark matter, stars and gas as particles, following the potentials used to describe the galaxy. These simulations use $N = 10^6$ particles and the equations for the potentials incorporated here are presented in Section 3.2.1. However, the system first needs to “relax” before it resembles a disc galaxy. This occurs when the system reaches an equilibrium state, i.e. an equilibrium between gravity and pressure that leaves the system in a stationary state. This happens on a dynamical time scale, which is roughly one rotation period of the galaxy. Therefore, the simulation are run with a much cruder refinement for $t \sim 200$ Myr (depending the the run) before feedback (in the feedback runs) is activated and any analysis is done. A shorter time was chosen for the higher gas fraction simulations, $t \sim 100$ Myr, as they underwent noticeable clumping much earlier. All of the simulations had 13 AMR levels during their relaxation period, which was then increased to 16 AMR levels. This corresponds to a minimum spatial grid cell size of $\Delta x \sim 10$ pc, allowing individual molecular clouds to be marginally resolved.

The hydrodynamic variables in RAMSES track four essential fluid parameters: density, 3D velocity vector and thermal pressure. In order to include metals into the simulation, the mass density of Fe and O are added to this list. Fe and O are highly relevant metals because they dominate the mass of SNII ejecta; they account for approximately 90% of mass ejected in a stellar population of $m_* = 10^4 M_\odot$ (Agertz et al. 2013). Furthermore, oxygen is an α -element and is assumed as a proxy for all α -elements. The metals merely act as scalars, following the fluid without directly affecting it. The simulation suite only takes into account these two metals, but during the cooling routine they are averaged together into a total metallicity (as the cooling function only depends on the total). They are combined according to

$$Z \approx 2 \cdot Z_{\text{O}} + 1 \cdot Z_{\text{Fe}}, \quad (3.6)$$

where the constants weigh them by the solar abundance of the α -elements and iron.

3.2.1 Galactic initial conditions

My simulations used galactic parameters chosen to emulate a Milky Way-sized galaxy at different redshift, based on those presented in [Agertz et al. \(2013\)](#) as part of the AGORA project. The initial conditions (ICs) were derived using GALIC ([Yurin & Springel 2014](#)), following the parametrisation of galactic disc done by [Mo et al. \(1998\)](#). The characteristic variables required to derive the structural setup for the galaxies in my simulations are shown in [Table 3.1](#). Many of the properties of a disc galaxy are connected with characteristics of the galaxy’s dark matter halo. A Navarro-Frenk-White profile ([Navarro et al. 1996](#)) is commonly adopted for the potential,

$$\rho_h(r) = \frac{\rho_h}{r/r_h(1+r/r_h)^2}, \quad (3.7)$$

where ρ_c is the critical density of the Universe (i.e. the density required for a flat Universe). The critical density sets the virial mass, which is approximately $M_{\text{vir}} = M_{200}$ and defined as

$$M_{200} = 200 \frac{4\pi\rho_c r_{200}^3}{3}. \quad (3.8)$$

In these equations $r_h = r_{200}/c$ is the halo scale length, c is the dark matter halo concentration and r_{200} is the virial radius. [Macciò et al. \(2007\)](#) determined the dark matter concentration factor from a fit of cosmological N-body simulations,

$$\log c = 1.020[\pm 0.015] - 0.109[\pm 0.005](\log M_{200} - 12), \quad (3.9)$$

where $h \equiv H_0/(100 \text{ km s}^{-1} \text{ Mpc}^{-1})$ is the reduced Hubble constant and H_0 is the Hubble constant. In the aforementioned Table, v_{200} is the circular velocity of the disc at the distance of virialisation. This is approximated as the maximum circular velocity, which is sufficient for my purposes.

These values are not only dependent on the dark matter halo and, therefore, it is useful to go through the other galaxy components. The bulge potential used here is given by [Hernquist \(1990\)](#) as

$$\rho_b(r) = \frac{M_b r_b}{2\pi r} \frac{1}{(r+r_b)^3}, \quad (3.10)$$

where r_b is the bulge scale length and M_b is the bulge mass. The density distribution of the stellar and gaseous disc is described by an vertically and horizontally logarithmic shape,

$$\rho(r, z) = \rho_d \exp(-r/r_d) \exp(-z/z_d), \quad (3.11)$$

where r_d is the scale radius of the disc and z_d is the scale height.

Additionally, the dark matter spin parameter λ is also required, but is usually assumed a value of $\lambda = 0.05$; derived from N-body simulations as the most likely value, in a log-normal probability distribution (e.g. [Bullock et al. 2001](#)). With all of this combined, if the reader has the resources and previous knowledge of performing hydrodynamic galaxy simulations, my simulations should be reproducible.

3.2.2 Simulation Runs

The designated names of the runs are given in Table 3.2 together with a brief mention of the adopted values for key galaxy parameters (e.g. gas fraction) and what physics is included. The initial conditions given in Table 3.1 were chosen in order to simulate a galaxy with a Milky Way mass at different stages of its evolution; essentially local and high redshift. However, note that the point here is not to do any direct comparison with the Milky Way. The gas fraction acts as a proxy for this, since the gas in an isolated galaxy is steadily depleted with time due to star formation. In other words, a high gas fraction galaxy represents a higher redshift galaxy. To compare the overall effects of feedback in a galaxy, two runs were done for each galaxy. One run includes all the feedback processes discussed earlier (denoted **FB**; SN type II, SN type Ia, stellar winds, radiation pressure) and one with no feedback (denoted **noFB**). The simulation box used in all simulations is a cube with sides of 600 kpc length and boundary conditions that allow the outflow of material. The large box and boundary conditions are chosen to mimic the environment of an isolated galaxy.

The following paragraph is intended to explain some discrepancies between the simulations, which was decided on to ‘finish’ my simulations within the set time frame of this project. During the course of running my simulations, the $f_g = 50\%$ gas fraction galaxy with feedback (**fg50_FB**) achieved suspiciously small time steps; meaning the simulation would not be done within any reasonable time. The issue was identified as the injection of thermal energy by SNe in the grid cells, increasing the temperatures to extreme levels. Thus, this increased the thermal motion, which lowered the time steps. A temperature roof was therefore set at $T = 10^8$ K. Furthermore, to quicken the simulation I also changed the mass condition for refinement, explained in Section 3.1.1, to reduce the number of grids with large AMR levels. In order to keep the AMR levels of the **fg10_FB** and **fg50_FB** analogous, the mass requirement was made five times larger, the same ratio as between their gas fractions.

The simulations were run through parallel computing, using MPI libraries. The computational resources came from the Aurora servers at Lunarc; a centre for supercomputing at Lund University.¹

¹<http://www.lunarc.lu.se/resources/hardware/aurora/>

Table 3.1: Initial conditions used for each run of simulated galaxies, explained in Section 3.2.1. The parameters are identical between runs with the same galaxy properties (gas fractions) but different physics (with and without feedback); hence the FB/noFB notation.

Simulation name	fg10_FB/noFB	fg50_FB/noFB
Stellar disc mass, $M_{d,*}$ [$10^8 M_{\odot}$]	386.9	214.9
Stellar bulge mass, M_b [$10^8 M_{\odot}$]	43.0	43.0
Dark matter halo mass, M_h [$10^{10} M_{\odot}$]	125.5	125.5
Gas fraction, f_g	0.1	0.5
v_{200} [km s $^{-1}$]	150	150
Dark matter concentration factor, c	10	10
Gas metallicity [Z_{\odot}]	1.67	1.67
Scale height disc, z_d [kpc]	0.34	0.34
Scale radius disc, r_d [kpc]	3.43	3.43
Scale radius bulge, r_b [kpc]	0.3432	0.3432

Table 3.2: Important characteristics of each simulation run. The choice of when to refine the simulations is motivated in Section 3.2.

Name of run	Description
fg10_noFB	$f_g = 10\%$ gas fraction, $\epsilon_{\text{ff}} = 1\%$ star formation efficiency, no feedback processes, refined at 200 Myr
fg10_FB	$f_g = 10\%$ gas fraction, $\epsilon_{\text{ff}} = 1\%$ star formation efficiency, all feedback processes discussed, refined at 200 Myr
fg50_noFB	$f_g = 50\%$ gas fraction, $\epsilon_{\text{ff}} = 1\%$ star formation efficiency, no feedback processes, refined at 100 Myr
fg50_FB	$f_g = 50\%$ gas fraction, $\epsilon_{\text{ff}} = 1\%$ star formation efficiency, all feedback processes discussed, refined at 100 Myr

3.3 Analysing data

From the output data of RAMSES, all the different properties of the gas and stars present in the simulations can be extracted. To avoid having to write my own routine for this, I use a galaxy analysis tool called *yt*² (Turk et al. 2011). The *yt*-environment also provides derived fields along with a set of plotting presets. I mainly use *yt* for loading the data and creating projection plots, which are used to visualise the galaxy and its properties. Beyond that, the codes I use for reading, analysing and plotting the data were developed by myself for this project. I created a pipeline for reading, analysing and plotting everything seen in this thesis using Python, and the code can be sent upon request³. One of the plotting codes I created as a general tool for plotting different quantities against each other, allowing for a large amount of customisation. Lastly, the simulations are visualised as videos for both temperature and density (discussed in Section 4.1.1), which is done using a Python 2.0 code available among the RAMSES utilities.

3.3.1 Observational comparison

In Section 2.4, I discussed the observational data, available in Table 2.1, with the purpose of comparing it in detail with the simulation data. The data is heavily heterogeneous, being observed at varying beam sizes, inclinations, redshifts and gas phases (due to the difference in gas tracers used). When presenting all the data in Figure 1.1, I include all of the data compiled in this project, but in the coming comparisons I omit some of the data. This is done by lowering the ceiling of the velocity dispersion, ignoring data above $\sigma_g \gtrsim 150 \text{ km s}^{-1}$. This allows for a more focused comparison in the dispersion range relevant for the simulation data. Notably, only the observational data by Lehnert et al. (2013) is found to be at these high dispersions. I will return to the key issue of heterogeneous observational data for the σ_g -SFR relation when doing comparisons with the simulations, Section 4.2.1.

The data here is handled in the same manner as in Krumholz et al. (2018), using some of the data compiled by the authors which they have made publicly available. However, a non-negligible portion of the data was compiled by myself. A key thing they do is that they try to account for the broadening of the expanding ionised gas by removing 15 km s^{-1} in quadrature to the observational data. This is not done in this project, as to avoid tampering too much with the observational data. However, it only has an effect, although small, on the low velocity dispersion values for H α .

3.3.2 Parameter analysis

With the parameters recorded by the simulations for the particles and stars, a long list of values can be derived. I will focus on calculating properties important for comparison with the velocity dispersion, which is taken as a proxy of turbulence. I evaluate the

²<https://yt-project.org>

³timmy.ejdetjarn@gmail.com

simulation values through an observational perspective, i.e. I observe the galaxy through cylindrical beams and calculate relevant quantities from the data within each beam. These are distributed isotropically from the centre of the galaxy, as seen in Figure 3.2. Generally, the radial range went from 1 kpc to 20 kpc with a 1 kpc increment and the row of beams were defined every 20° step, giving rise to 18 angles. In total, the number of beams for each output, or time step, analysed was 360 beams. Keep in mind that then each of these beams were also evaluated for a range of beam sizes, inclinations and gas tracers.

Furthermore, in my analysis I consider some of the observational properties discussed in Section 2.4.1; the inclination angle of the galaxy, beam size and different gas tracers. The purpose is to see whether these have a significant impact on the measured velocity dispersion of galaxies and if they could explain some of the high literature values in the σ_g -SFR relation (as seen in Figure 1.1).

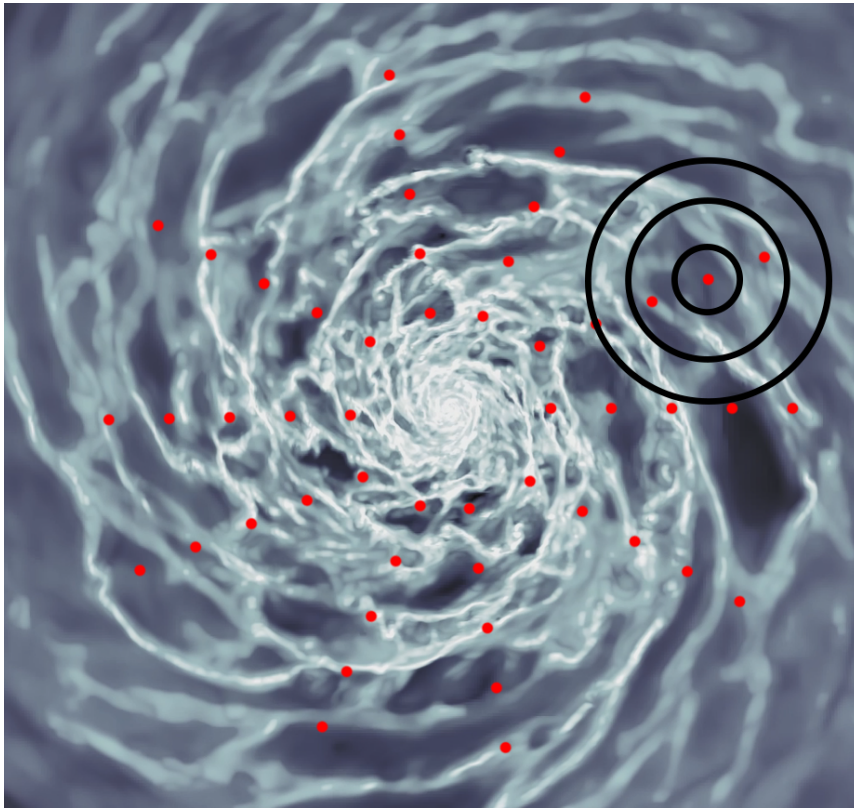


Figure 3.2: An illustration of how the beams were distributed throughout the galaxy. The galaxy in the background is the fg10_10FB run. The red dots correspond to positions in which a beam is located. For each position, different beam sizes are used, as demonstrated for one of the red dots as big black rings. The beams were distributed according to Section 3.3.2. This figure does not accurately portray the number of bins or the beam sizes used.

The gas velocity dispersion calculated here is weighted by the mass of each cell, to

account for the bulk velocity of the fluid. The mass-weighted σ has the general form,

$$\sigma = \sqrt{\frac{\sum_i W_i (v_i - \langle v \rangle)^2}{\sum_j W_j}}, \quad (3.12)$$

where W_i are the weights and $\langle v \rangle$ is the average velocity of the gas in the region analysed. Comparisons for a σ with no weights did, in most cases, not show significant difference and are therefore not present in the results. As is common, the dispersion is assumed to be isotropic. This turbulence is not the full turbulent velocity, as the sound speed of the medium,

$$v_s = \frac{\gamma k_B T_{\text{mean}}}{m_H}, \quad (3.13)$$

is needed in order to determine the total turbulent velocity, which is done simply by adding the velocities in quadrature $\sigma_{\text{g,tot}} = \sqrt{\sigma_{\text{g}}^2 + v_s^2}$. This was done for each σ_{g} plot presented here, when doing direct comparisons with analytic models (as they do not include the speed of sound). In this equation, $\gamma = 5/3$ is the adiabatic index, T_{mean} is the mean temperature and m_H is the hydrogen mass.

In this project, I consider the following inclination angles

$$\theta = [0, 15, 30, 45, 60, 75, 90]^\circ. \quad (3.14)$$

These were applied in the analysis by a simple sine/cosine rotational transformation of the positions and velocities of both stars and gas. For the plots in which simulation data for different angles have been used, I refer to the gas velocity dispersions as line-of-sight (σ_{LOS}). The size of the beams are defined as the diameter of the cylinders, which makes it more immediately comparable to the beam sizes of the observational data. An example of the range of beam sizes used in this project is

$$d_{\text{beam}} = [0.1, 0.5, 1, 2, 4, 6, 8, 12] \text{ kpc}. \quad (3.15)$$

The range of radii sizes used for the beams were altered throughout the analysis, partly because the velocity dispersion recorded for $d_b \lesssim 0.1$ kpc was found to have a large scatter in the σ_{g} -SFR relation, which would inhibit the analysis. For example, I used more beam when investigating the effects of beam size in Section 3.3.2.

Since both dark matter and stars are treated as particles, it is crucial to apply a mask to filter away the dark matter in the analysis. This is done through a mask for the particle mass, made to only include the masses of the less-massive disc stars. The star formation rate can be determined by looking at the formation time of particles and calculate how the star mass M_* has changed with time t . The masses are binned in bins of $\Delta t \sim 10$ Myr, which is a commonly used age for young stars (e.g. [Agertz et al. 2013](#)). With the masses divided into bins of time, the star formation is simply the time derivative of the masses, using a first-order linear approximation.

Table 3.3: Temperature cuts performed during analysis and their respective phase and tracer analogue. The cuts are the same as shown in Figure 2.2 and are evidently approximate.

Temperature [K]	5 – 20	$1 \times 10^2 - 1 \times 10^4$	$6 \times 10^3 - 2 \times 10^4$
Phase	Molecular	Warm & Cold Neutral	Warm Ionised
Approximative Tracer	CO	HI	H α

3.3.3 Defining gas phases

In this project, I recognise three major gas phases: molecular, (warm and cold) neutral and warm ionised; all composed mainly of hydrogen. I use two approaches for approximating the different gas tracers. The first one is done by performing simple temperature cuts, which does not fully represent the continuity of the phases in the ISM. The cuts used, along with what phase and observational tracer they correspond to are shown in Table 3.3 and represented in Figure 2.2. The benefit of this simple temperature based approach is its simplicity, and as I demonstrate in subsequent chapters, it illustrates well the level of turbulence present in different gas phases.

The other approach utilises the hydrogen and electron number densities, n_{H} and n_{e} , recorded by RAMSES. With this approach, each phase no longer follows a strict temperature boundary and is instead defined by phase-specific weights, meaning they naturally overlap, which is already present in the small overlap of the temperature cuts. The neutral hydrogen phase (cold and warm combined) is weighted by the hydrogen number density n_{H} . The molecular hydrogen is weighted by the molecular hydrogen fraction f_{H_2} , derived using the formalism of Krumholz et al. (2009). The warm ionised phases, traced by H α used theoretically derived emissivities (thermally emitted radiation) as its weight and applying experimental values of the $3p \rightarrow 2s$ transition in hydrogen, as was mentioned in Section 2.4.1. Both the emissivity coming from collisional excitation and recombination was considered during this analysis, described further down. The emissivity for both have the shape

$$\epsilon_{\text{H}\alpha} = n_{\text{e}}n_{\text{H}}h\nu q, \quad (3.16)$$

where q is the rate at which H α is emitted, the form of which is related to the theory behind its derivation. The energy of the H α emission is $h\nu = 3.026 \times 10^{-12}$ ergs, where ν is the light frequency and h is the Planck constant.

For my analysis, I used two different rates, which represent H α emission from collisional excitation

$$q_{\text{coll}}(T) = \frac{1.3 \times 10^{-6}}{T^{0.5}} \left(\frac{T}{11.2} \right)^{0.305} \times \exp \left(\frac{-h\nu}{kT} \right) \quad (3.17)$$

and recombination (following the formalism in e.g. Dijkstra 2017)

$$q_{\text{recom}} = \epsilon_{\text{H}\alpha}^{\text{B}}(T)\alpha_{\text{B}}(T), \quad (3.18)$$

where

$$\epsilon_{\text{H}\alpha}^B = 8.176 \times 10^{-8} - 7.46 \times 10^{-3} \log_{10}(T/10^4) + 0.451010 \times (T/10^4)^{-0.1013} \quad (3.19)$$

is the emitted rate of H α and

$$\alpha_B(T) = 2.753 \times 10^{-14} \times \left(\frac{315614}{T}\right)^{1.5} \times \left(1 + \left(\frac{315614}{T}\right)^{0.407}\right)^{-2.42} \quad (3.20)$$

is the probability that the cascade from hydrogen recombination emits an H α photon (fit from [Hui & Gnedin 1997](#)). These are case B recombinations, which is the case that allows cascading of energy. These q values can be added linearly to calculate the total emissivity. When calculating the emissivity within a cell, it is multiplied with the volume of the corresponding cell to avoid bias between the phases (since e.g. molecular hydrogen occupy the highest refinement levels).

The simulated emissivity shows a good agreement with the temperature cut since its peak is close to the temperature range used, as seen in [Figure 3.3](#). However, when comparing the σ_g -SFR relation for the two methods later, in [Section 4.3](#), there is a noticeable difference; which occurs due to the calculated ISM being continuous.

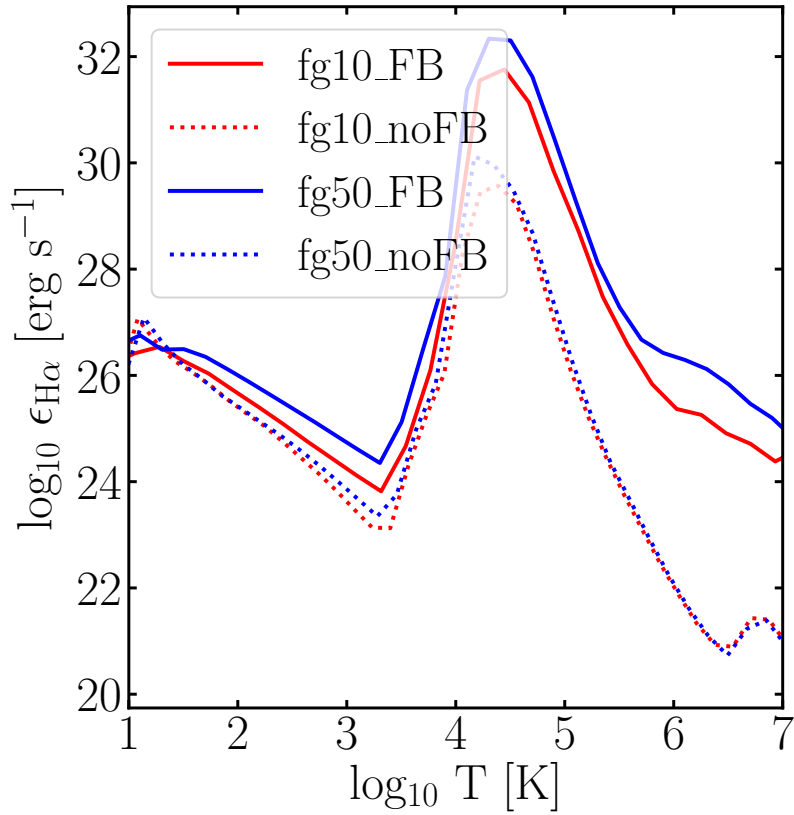


Figure 3.3: The distribution of H α emissivities as a function of temperature for the simulation runs. A clear peak can be seen around the temperatures $T \approx 10^4 - 10^5$ K and only the magnitude seems to lessen for the runs without feedback. The fact that the emissivity peak is around the temperature cuts used (Table 3.3) is encouraging for the use of temperature cuts to approximate the gas phases; here it mainly confirms the gas tracer for the warm ionised medium.

Summary of chapter 3:

- I perform simulations with the N -body+hydrodynamical code RAMSES and use a custom patch, provided to me, to implement star formation and feedback.
- Initial conditions for the simulations are for a Milky Way-like galaxy (characteristic masses and sizes), but at different redshifts; in order to cover both regimes, local and high-redshift galaxies, in the σ_g -SFR relation.
- Analysis is done with a completely self-written Python code, both for plotting and deriving quantities. Projection plots are done with the analysis code *yt*.
- The analysis is focused on the SFR- σ_g relation, with emphasis on the impact of observational parameters, such as beam size, beam smearing and gas tracer.

Chapter 4

Results

In this chapter I present the analysis of my simulated galaxies, following the methods outlined in Section 3.3. This chapter starts with thorough effort to validate the simulated data, which is done through visual representation and reproducing known galaxy quantities. This establishes confidence in the RAMSES, which will in turn encourage that the analysis will be correct. Next, I present the key relation of this project, σ_g -SFR, that I want to reproduce; together with observational data. Furthermore, the observational parameters discussed in Section 2.4.1 (beam size, galaxy inclination and gas tracer) are taken into consideration and evaluated in detail to see how they affect this relation; the method detailed in Section 3.3.2.

4.1 General properties of simulated galaxies

In order for the simulations to be trusted in a comparison with observational data, the validity of the simulations need to be benchmarked against known galactic properties. In the following subsection, I will go over the more important and relevant properties and confirm their appearances with data and predictions.

4.1.1 Visual comparison

An intuitive comparison can be done between how the simulated galaxy behaves and what is expected too see from a typical galaxy. Figure 4.1 shows the temperature and density projection of each galaxy run, as briefly laid out in Table 3.2. The specifics of the simulation parameters are given in the caption of the figure. A spiral structure is present in the galaxies and the no-feedback galaxies start to clump up to form denser structures of cold molecular gas. The importance of feedback is also seen in the vertical structure, where it evidently drives explosive outflows of gas. Movies of the projected density and temperature were also created for all simulations and have been compiled into several videos¹. From the movies

¹<https://www.youtube.com/playlist?list=PLev-Ya4xEN0s2NsbZALfbQtikwpNGtg5M>

it is evident how material is quickly ejected as feedback is turned on and how it later rains down onto the galaxy again.

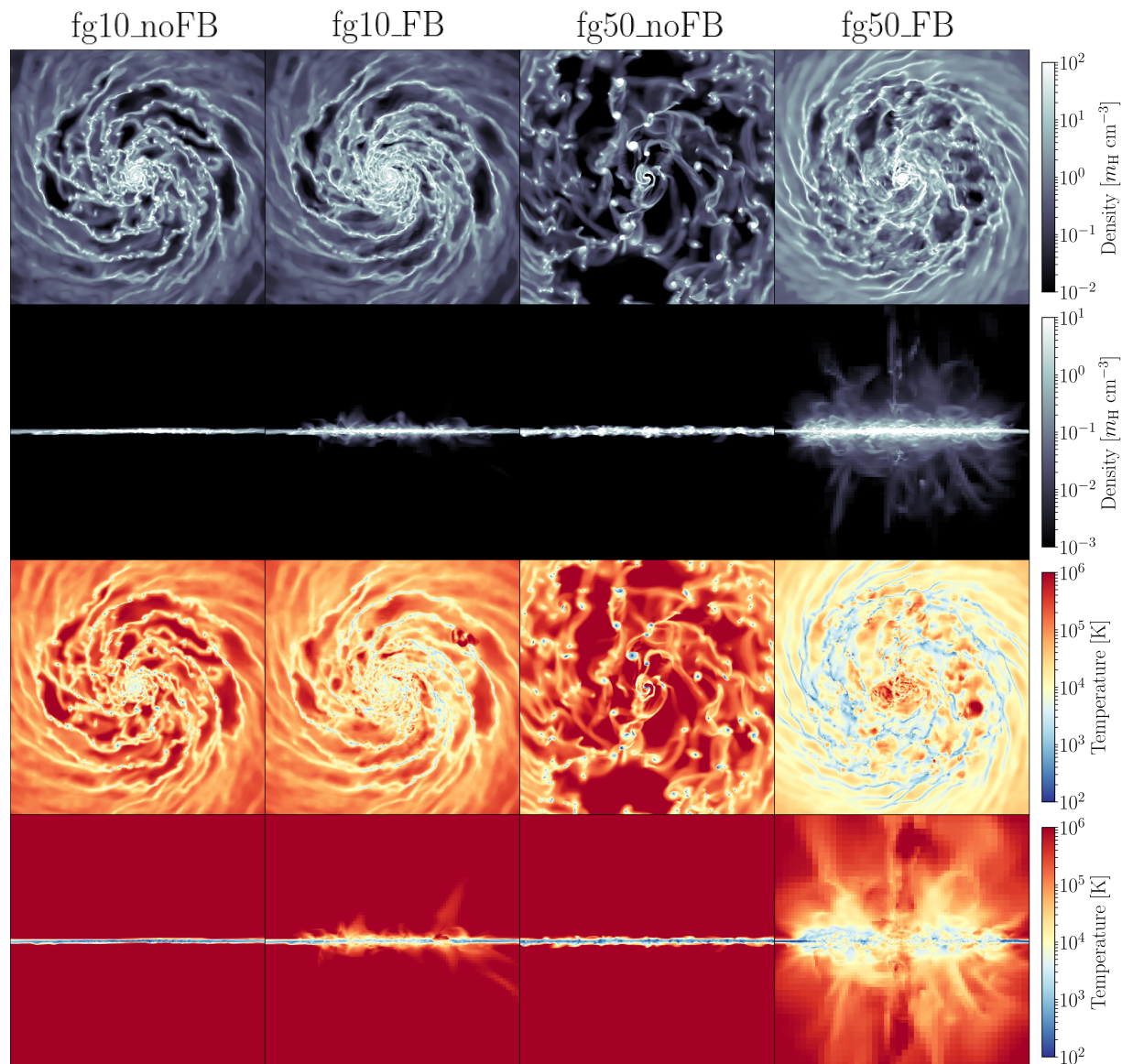


Figure 4.1: Projected properties of the density and temperature of the simulated galaxies. The size of these boxes are all $20 \text{ kpc} \times 20 \text{ kpc}$, and the **fg10** runs are evaluated at $t = 250 \text{ Myr}$, while the **fg50** runs are calculated at $t = 150 \text{ Myr}$. The runs without any feedback are seen to clump together more and there is a clear correlation with the more dense areas being colder. Some clumping, as seen in the **fg50_FB** run, is expected in high-redshift galaxies. Outflow of material is another key characteristic in the feedback runs which is observed in these plots.

4.1.2 Galaxy PDFs

The probability distribution function (PDF) of a galaxy’s density is an important property useful to evaluate whether the simulation is reasonable. The PDF is simply a function which describes the probability for the system (in this case a galaxy) to attain a certain value. This requirement can intuitively be understood from the visual plot, Figure 4.1, where the galaxy forms a lot more dense clumps when there is no feedback occurring. The density and temperature PDFs are shown in Figure 4.2. The temperature distribution between the FB and noFB runs are evident as the noFB runs can not reach the higher temperatures spurred on from SN and stellar winds through shocked winds, as discussed in Section 2.3. The density distributions are a bit more complicated, since stellar feedback tears apart the molecular clouds for the but also causes very dense shocks. Therefore, `fg10_FB` can be seen to have a lower maximum density than `fg10_noFB`, while `fg50_FB` has a higher maximum density than `fg50_noFB`. The difference could then be that `fg50` has more material around to cause these dense shocks, while the SNe in `fg10_FB` is more located in spiral arms. Furthermore, the galaxies with feedback are expected to reach lower densities simply from SNe creating a warm and diffuse phase in the ISM (see Section 2.1 for the gas cycle and how this warm phase is formed). The stochastic density fluctuations of turbulence, then caused by stellar feedback, is also a possible explanation for this behaviour. In general, the PDFs also agree with previous simulations that have investigated the density and temperature distributions (e.g. Agertz et al. 2013).

4.1.3 Star formation histories

The formation of stars is a key property for every subject within astronomy. In Figure 4.3, the SFR and gas fraction of the galaxies is plotted against time. These were evaluated globally, i.e. calculated independently of the beam analysis and represent the total SFR and gas fraction. As seen, the results are in agreement with expectations. The low gas fraction simulations have much less ongoing star formation, `fg10_FB` has $\dot{M}_* \sim 1 M_\odot \text{yr}^{-1}$ compared to $\dot{M}_* \sim 25 M_\odot \text{yr}^{-1}$ for `fg50_FB`, due to the lack of gas to form more dense molecular clouds. Another property seen is that feedback does indeed regulate the star formation in the galaxies; the SFR of `fg10` is almost an order of magnitude larger, $\dot{M}_* \sim 10 M_\odot \text{yr}^{-1}$, without feedback and `fg50_FB` reaches $\dot{M}_* \sim 100 M_\odot \text{yr}^{-1}$ at one points. This is made more evident when looking the global gas fraction as a function of time, seen in the same figure, where the depletion of gas is hindered in the FB runs. A key thing to note is the steep decline in gas fraction with time for the `fg50` simulations. It does not take long before the galaxy is closer to $f_g \sim 30\%$ than $f_g \sim 50\%$.

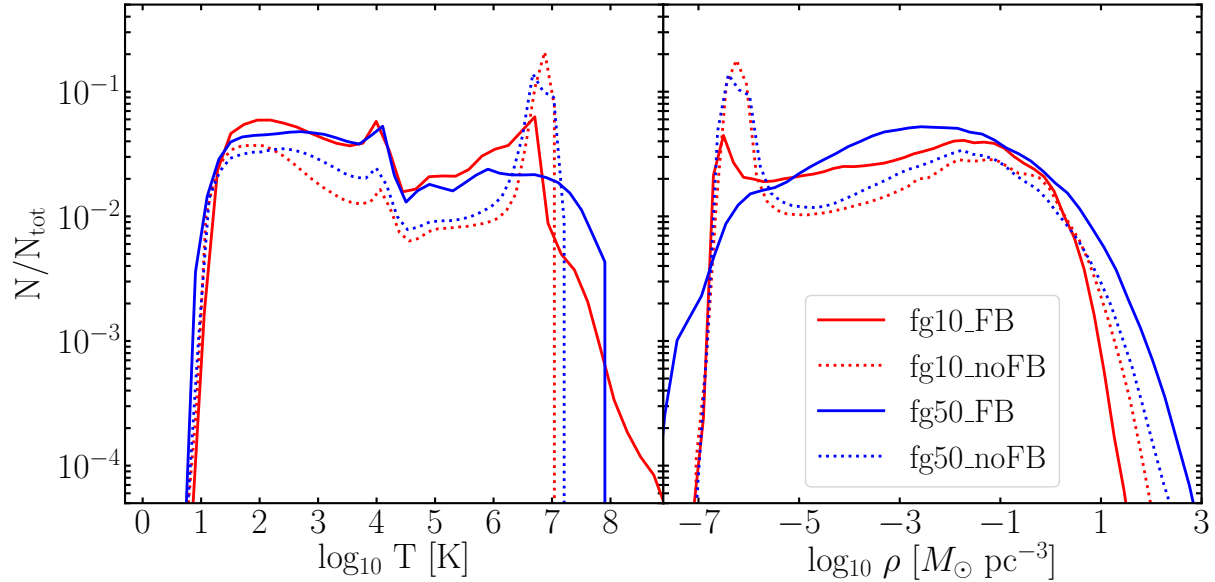


Figure 4.2: The density and temperature PDFs of the galaxy in each run. The density is seen to be more spread out for the FB run galaxies. These are calculated around 300 Myr for all simulations, except fg50_FB, which is shown at $t = 200$ Myr in its run. However, they were evaluated for the same time duration in refinement $\Delta t = 100$ Myr, due to the difference in when the refinement was turned on (see Section 3.2).

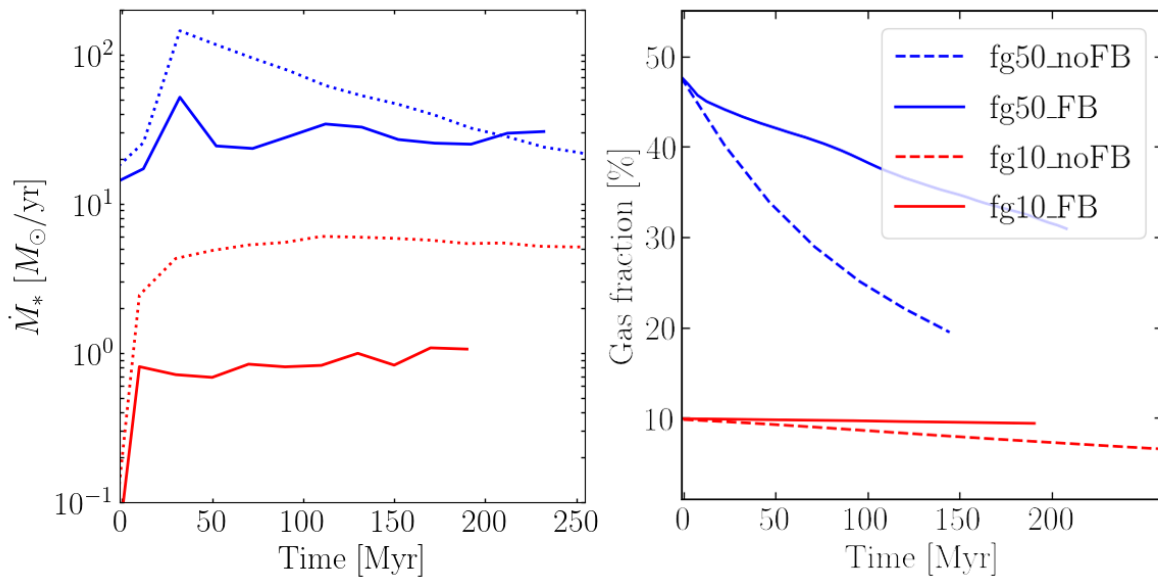


Figure 4.3: The SFR and gas fraction through time for each run. These are global values, i.e. the SFR and the gas fraction was evaluated for the entire galaxy. The effects of feedback are confirmed to overall work as a suppressor of the star formation rate. The high gas fraction simulations rapidly deplete all its gas supply.

4.1.4 Kennicutt-Schmidt relation

Here I present the KS-relation, discussed in detail in Section 2.2, reproduced with my simulated galaxies. The observed behaviour of my simulated galaxies is seen in Figure 4.4 to be a good match to local galaxies (Bigiel et al. 2008), i.e. for the low gas fraction runs. However, the simulation without feedback seems to follow a shorter depletion time $\tau = 0.1$ Gyr. The higher gas fraction runs reach the lower range of values suggested by high- z galaxies (Kennicutt 1998). This is encouraging, as matching this data is not trivial to do and does offer confidence to future results.

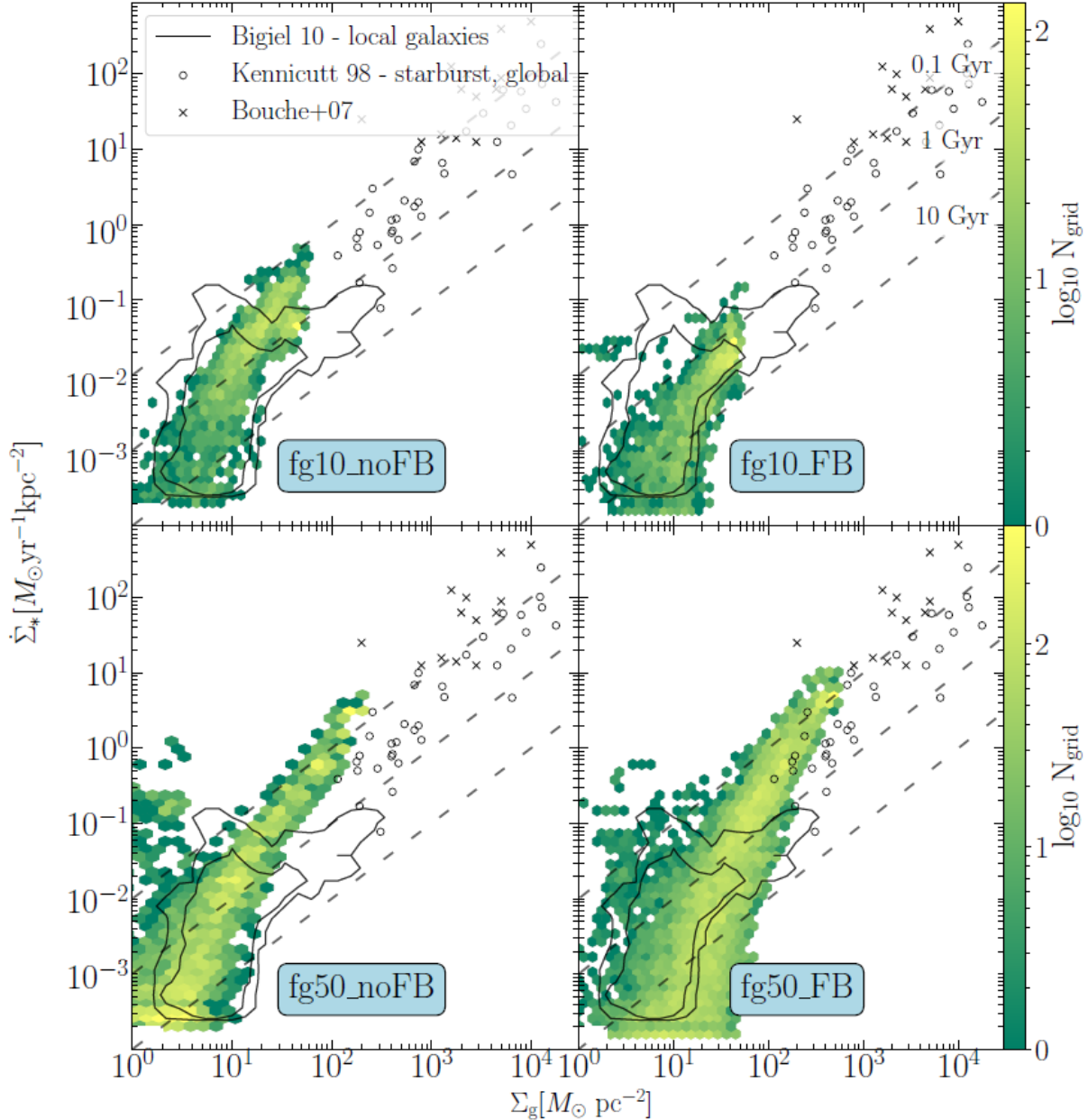


Figure 4.4: The KS-relation between surface density of gas Σ_g and star formation rate $\dot{\Sigma}_*$. The coloured density diagram is of the simulated and the number of points in each grid is scaled with colour logarithmically, as seen by the colour bars. The black contours in the plot is data from (Bigiel et al. 2008) for local galaxies; two contours are shown, the smaller contour simply shows better where the data is concentrated. The black circles are observations from Kennicutt (1998) of starburst galaxies. All of the data here has been observed as a combination of H I and H₂ and using a beam size of 0.5 kpc (only true for the Bigiel observational data). The three dotted lines represent different depletion times of gas in the local region ($\tau = 0.1, 1, 10$ Gyr), their corresponding values are shown in the upper-right plot on their respective line. Each plot represent one simulation run, noted by their respective text boxes. The specifics on the appearance of this figure is discussed in Section 4.1.4.

4.2 The σ_g -SFR Relation

The key relation I want to reproduce with my simulations in this project is the observed σ_g -SFR relation. By analysing the data from the galaxy simulations, as laid out in Section 3.3, I derived the two parameters and plotted them in Figure 4.5; together with the observational data from Table 2.1. The plots show an excellent agreement between the σ_g and observations, producing the two very recognisable features: plateau and exponential increase with the star formation rate. This is very encouraging for performing more detailed analysis of the factors which affect the σ_g -SFR relation.

The simulation data is presented here as coloured heat maps (or 2D histograms), where yellow colours corresponds to a higher density of points within that grid, as indicated by the colourbar. To avoid outliers, grids with less than 3 data points in them have been removed from this plot. The data used here is for a galaxy observed head-on, beam size ≥ 0.5 kpc, and simulation time $150 < t < 350$ Myr. Using smaller beam sizes was found to give a very large scatter in σ_g and are thus omitted. The change in σ_g stemming from varying inclination or beam size is evaluated in detail later in this Section.

In the coming sections, I only present a limited range ($\sigma_g \leq 150 \text{ km s}^{-1}$) for my plots. This is in order to more qualitatively compare with the relevant range for data derived from my simulations, as some of the observational data is above this range, which my simulations do not show. To note is that only the observational data from Lehnert et al. (2013) has recorded velocity dispersion $\sigma_g \gtrsim 150 \text{ km s}^{-1}$ (see Figure 1.1 for all of the data). Therefore, this does not limit the comparison in any way.

By fitting the simulated and observational data according to a polynomial of the form

$$\sigma_g = a\dot{M}_*^b + c, \quad (4.1)$$

I recover the fitting parameters presented in Table 4.1. Note that the theoretical predictions of the gravitational instability and stellar feedback models in Eq. 2.18 and 2.18, respectively, find $\sigma_g \propto \dot{M}_*^b$ where $b = 1$ and $1/2$, respectively. This is not the fitting parameters that a straightforward fit of the observational data recovers. However, the simulated data obtains very similar scaling parameters from the fit. The difference in scaling between simulated data and analytical models is discussed in Section 5.1.

Table 4.1: The scaling between σ_g and SFR, determined from fitting function of the shape in Equation 4.1 and described in this Section.

Data parameters	a [$\text{km s}^{-1} \text{ M}_\odot^{-1} \text{ yr}$]	b	c [km s^{-1}]
Observ. data, H α	23.402 ± 7.383	0.286 ± 0.055	14.122 ± 7.351
Observ. data, H I	5.885 ± 2.405	0.259 ± 0.177	7.088 ± 2.137
fg50_FB, all gas	29.1445 ± 1.209	0.155 ± 0.005	-11.417 ± 1.206
fg50_FB, H α	12.262 ± 0.963	0.347 ± 0.016	30.279 ± 1.015

4.2.1 Exploring observational parameters

Here I go into depth about how the parameters mentioned in Section 2.4.1 can affect the observed velocity dispersion. I previously showed that the simulations are unable to reach the high σ_g seen by observational data and the following analysis aims to explain this discrepancy between simulations and observations.

Beam size

In order to quantify the effects of beam size on the velocity dispersion, I collect the values in bins of SFR and beam size. This is in order to eliminate SFR as a contributing factor of the velocity dispersion. I initially find that there is a negative correlation between the size of the beam and the velocity dispersion, as seen in Figure 4.6. This goes against intuitive understanding of velocity dispersion increasing with the observed volume; the larger the volume observed, the larger the variation in velocities. More importantly, it is incorrect on theoretical (e.g. Kolmogorov 1941) as well as observational (e.g. Mac Low & Klessen 2004) grounds.

With careful investigation, it became evident that there is a large insecurity with the smaller beams. Since these beams do not cover many star formation events, most small beams have an insignificant SFR. However, there are still some observed points with a high SFR, and they have a large velocity dispersion in my data. This is likely due to them simply, by chance, being centred on a clump of gas with active star formation, in which the velocity dispersion is naturally higher (due to the σ_g -SFR relation). With this in mind, I calculate the velocity dispersion weighted by the number of points in each SFR bin and plot it against the beam size again, seen in Figure 4.6 as a dashed line, which appears to fit better with predictions.

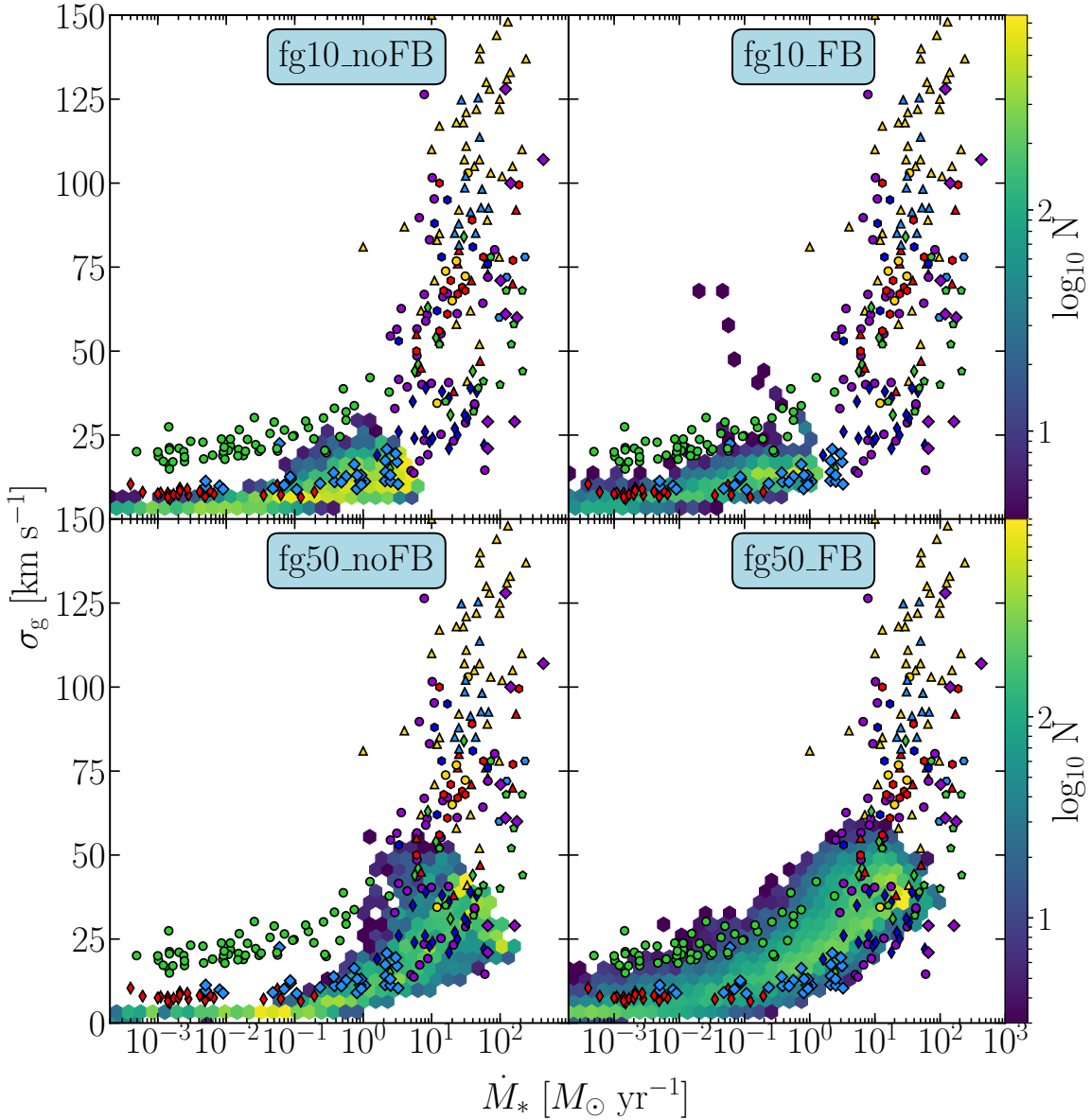


Figure 4.5: The σ_g -SFR relation for each simulation run. The markers correspond to the different data points, shown in Table 2.1. The simulation data is seen as the blue-green-yellow heat map behind the data points, where yellow indicates a higher density of points. The velocity dispersion is evaluated from looking at the galaxy head-on, $\theta = 0^\circ$, beam size ≥ 0.5 kpc and including all of the gas (no defined phase). There is no significant difference noticed between the FB and noFB runs. The exception is the large σ_g in fg10_FB, which is likely from beams mainly containing ionised, diffuse gas.

Beam smearing

I present a set of plots in Figure 4.7 which are identical to those in Figure 4.5, except for the inclusion of inclined galaxies in the simulation data. This shows the possible effects of beam smearing, if the dispersions is not corrected for inclination. The high inclination of galaxies seem to be able to explain all the observational data. Of course, this is not the full explanation, but it highlights the effects of beam smearing on the observed velocity dispersion. To quantify the inclination angle needed for this effect to be important, I plot σ_{LOS} against the line-of-sight angle, for both gas fractions. To eliminate SFR as a contributing factor of the velocity dispersion, I use the same outline as when evaluating the beam size, which is plotted in Figure 4.8. From this, it can be seen that an angle of roughly $\theta \approx 45^\circ$ is enough to explain $\sigma_{\text{LOS}} \sim 100 \text{ km s}^{-1}$ in high SFR regions.

ISM gas phases

The gas phases in the ISM have inherit differences in density and temperature between the phases, thus their kinematics may not be the same. This would mean that the magnitude of the turbulence likely depends on the tracer and adds difficulty in performing comparisons between their measured velocity dispersions. This is shown in Figure 4.9 and 4.10, displaying the measured velocity dispersion of three distinct phases for the `fg10` and `fg50` simulation runs, respectively. The observational data are divided into the gas phase corresponding to the tracer used to derive those values. Here, temperature cuts have been used to estimate the phases, but a more thorough approach is performed in Section 4.3.

Feedback is seen to be crucial for the $\text{H}\alpha$ velocity dispersion, as the observed σ_g could not be explained without feedback for this particular tracer. It is not surprising that $\text{H}\alpha$ would be different for the `noFB` and `FB` runs, since the ionised hydrogen phase (of which $\text{H}\alpha$ is a tracer) is a product of stellar feedback. However, the exact difference is not obvious and it is reassuring that the ionised phase is able to explain the high velocity dispersions recorded from observations. Further focus is put on this subject in Section 5.2.

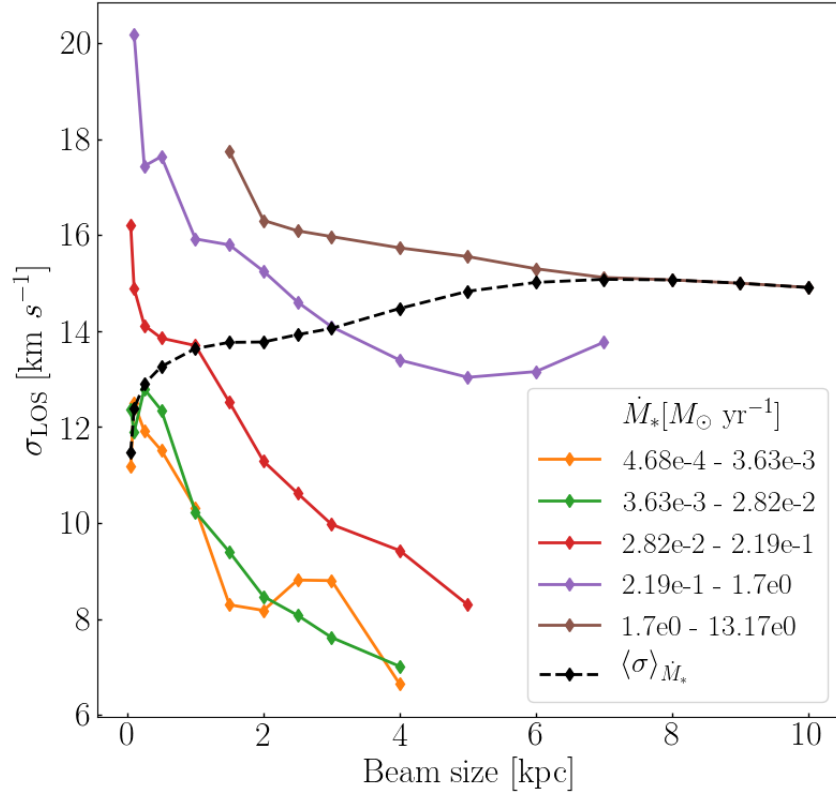


Figure 4.6: The velocity dispersion in different SFR bins as a function of the beam size used; here I adopted to have more beam sizes than the rest of the analysis, $d_{\text{beam}} = [0.05, 0.1, 0.25, 0.5, 1, 1.5, 2, 2.5, 3, 4, 5, 6, 7, 8, 9, 10]$ kpc. This figure uses simulated data from `fg10_FB`. The shape of these lines at different SFRs is not as expected when considering that observational and theoretical work indicate that turbulence should increase with beam size. This likely had to do with small beams landing on very turbulent patches. To properly evaluate this relationship, the weighted average of all the bins were taken for each beam size, using the amount of points in each SFR beam as their weight; shown as a dashed line.

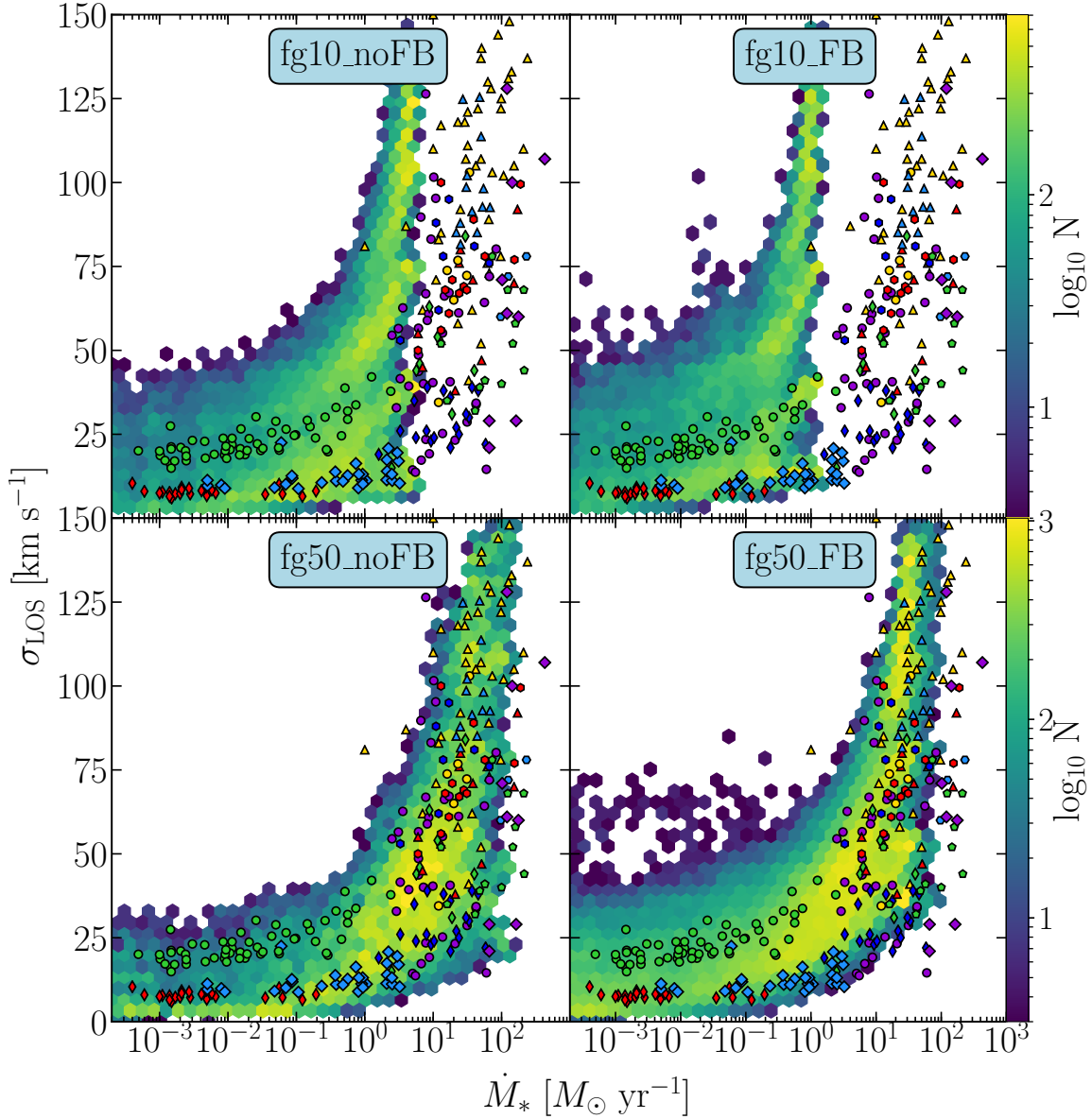


Figure 4.7: The σ_g -SFR relation for each simulation run. The markers correspond to the different data points, shown in Table 2.1. The simulation data is seen as the green-yellow histogram behind the data points, where yellow indicates a higher density of points. The velocity dispersion is evaluated from every inclination angle, $\theta = 0 - 90^\circ$, and including all of the gas (no temperature mask). The possible effects of beam smearing are highlighted when compared to Figure 4.5. Each angle has a slightly different curve for this relation, which can clearly be seen from the histogram in fg10_FB. There is no discernible difference between FB and noFB runs.

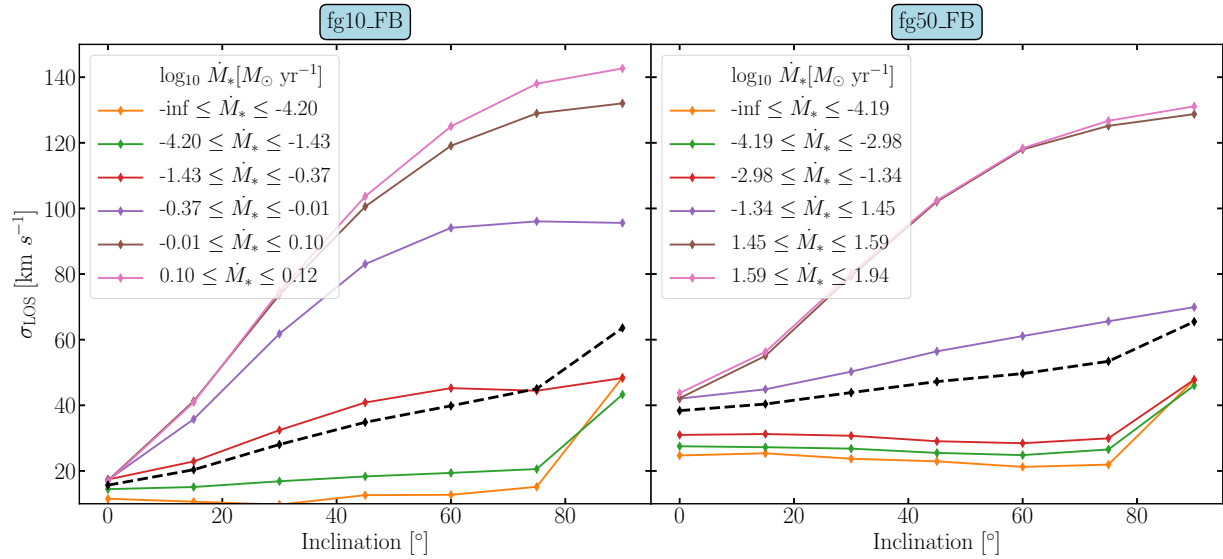


Figure 4.8: The velocity dispersion in different SFR bins as a function of the galaxy inclination. Left plot shows the `fg10_FB` data and the right shows the `fg50_FB` data. The dashed line is the averaged quantity, using the amount of points in each bin as their respective weights. A clear increase in σ_{LOS} is seen with inclination and, for a high SFR region, even a small uncorrected inclination $\theta = 45^\circ$, affects the velocity dispersion severely $\sigma_{LOS} \sim 100 \text{ km s}^{-1}$. The implications of these is especially prominent in high-redshift galaxies.

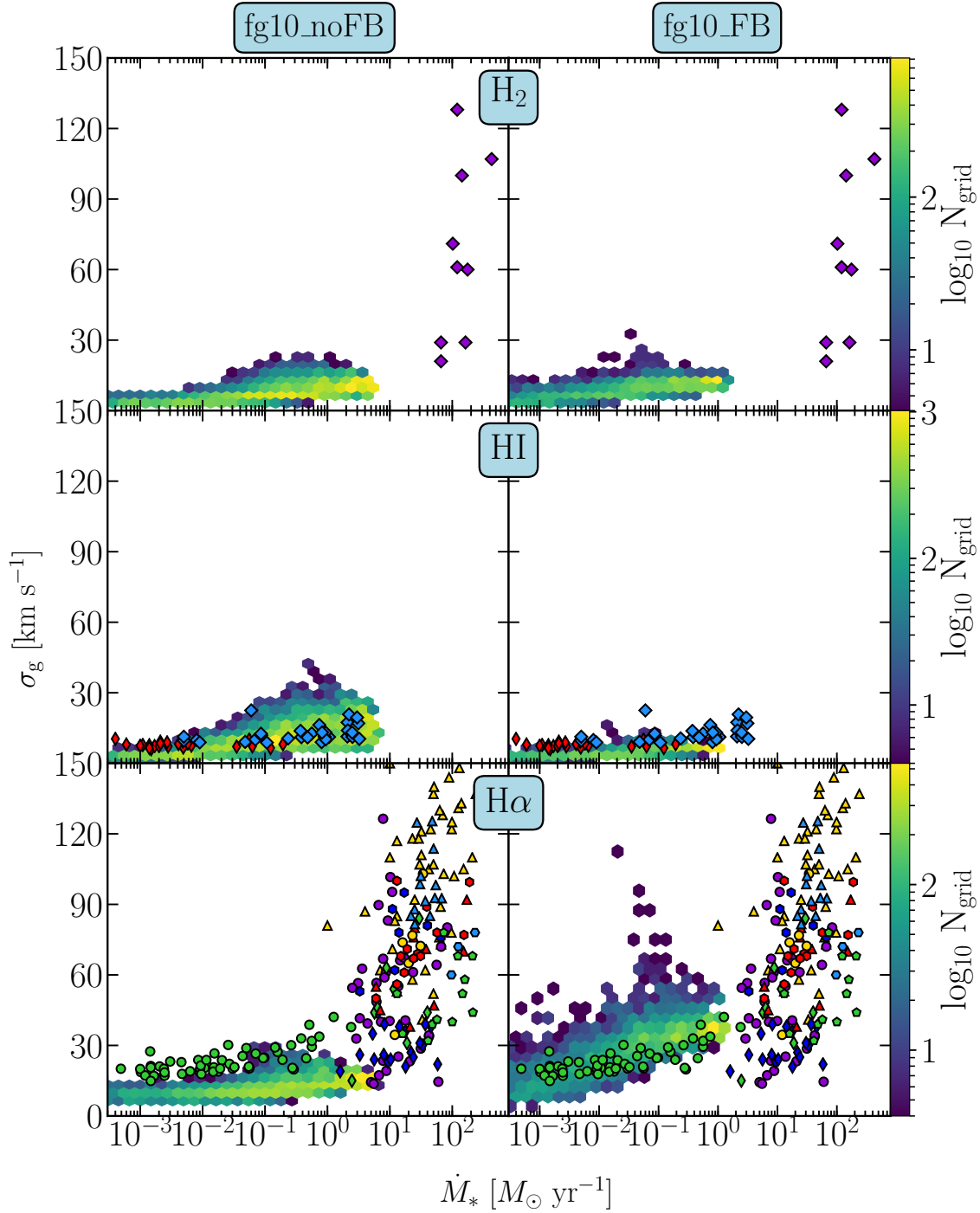


Figure 4.9: The σ_g -SFR relation in the fg10 simulation for different gas tracers, using the straightforward approach of temperature cuts to defined the gas phases. Molecular and atomic σ_g are seen to vary only slightly when including feedback, while H α is noticeably higher for the feedback run. This makes comparisons between phases troublesome and their differences need to be kept in mind.

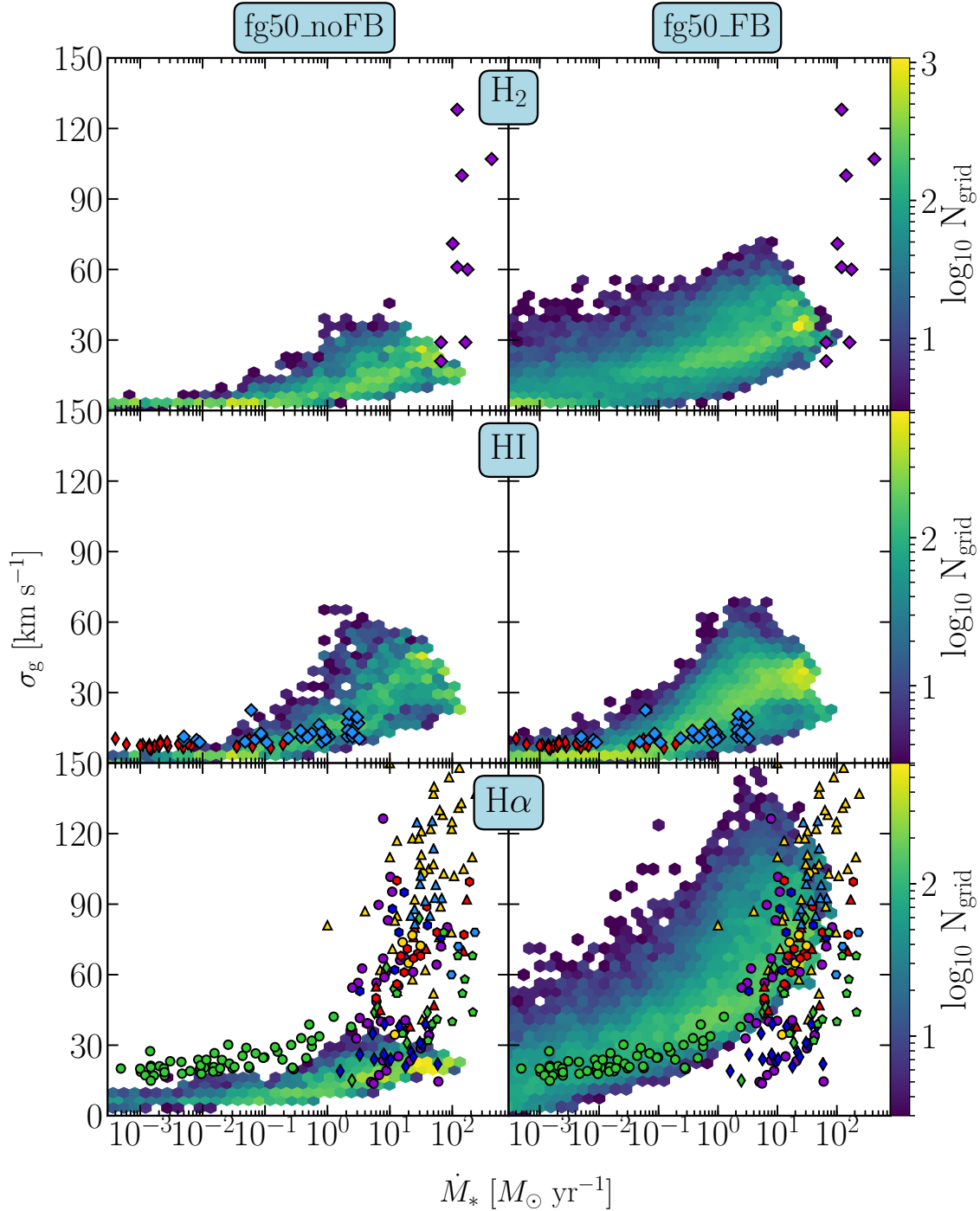


Figure 4.10: The σ_g -SFR relation in the fg50 simulation for different gas tracers, using the straightforward approach of temperature cuts to defined the gas phases. Molecular and atomic σ_g are seen to vary only slightly when including feedback, while H α is significantly higher for the feedback run. This makes comparisons between phases troublesome and their differences need to be kept in mind.

4.3 Mock observations

The temperature cuts performed here are very approximate in nature and a more qualitative approach is warranted when exploring the complex dynamics of the gas phases. In this section, the different phases are derived from ionisation conditions stemming from both collisional and recombination effects, as outlined in Section 3.3.3. In Figure 4.11, I show several projections (both face- and edge-on) of the simulated galaxies, where each projection corresponds to a gas phase. With this careful approach, these galaxies can be seen as realistic pictures of a galaxy if observed locally and with perfect information of the galaxy.

In Figure 4.12, I plot σ_g -SFR for the more realistic approach of defining the gas phases. In comparison to what was found in Figure 4.10, by using temperature cuts, the difference is not significant. The main difference is that H α did not reach the same SFRs, which likely has to do with the warm ionised phase not being present in star forming clouds for long enough (in this, more thorough, approach). This shows that the use of a temperature cut is a decent approximation for these simulations. As explained in Section 2.4.1, the observational data set shown is not homogeneous, leading to faulty comparisons between simulated and observational data. Since most high-redshift (with a lot of star formation) galaxies can mainly be observed globally, I highlight the importance of beam sizes in Figure 4.13. Clearly, the distribution of the velocity dispersion observed with H α (for high-redshift galaxies) would look significantly different if observed at higher resolutions.

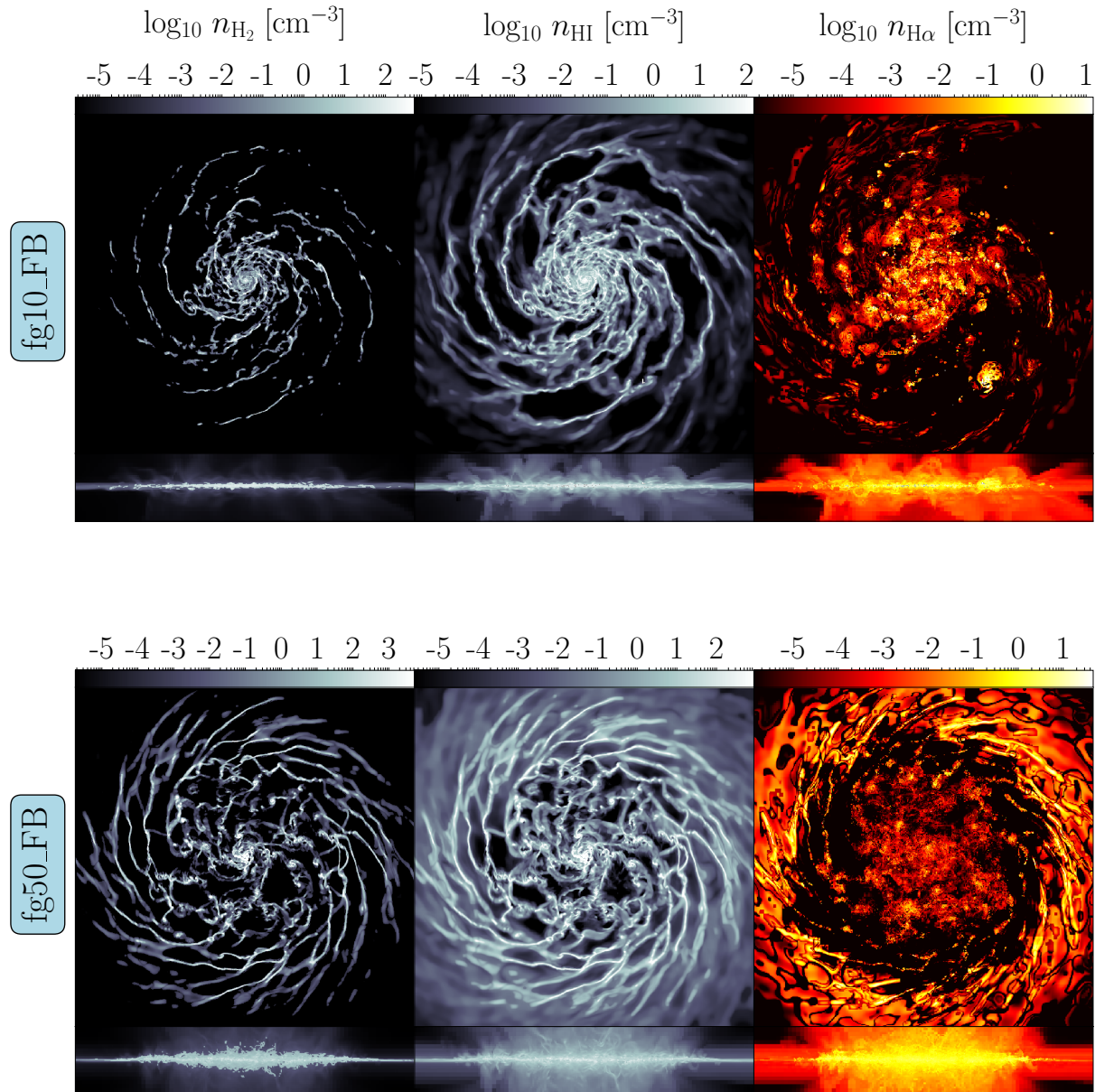


Figure 4.11: A projection map of the different gas phases in the interstellar medium, showing the feedback simulations of both gas fractions. Here, the number density n is denoted with H_2 , HI or $\text{H}\alpha$, which all are the weighted number density, using the weights relevant for the corresponding phases (described in Section 3.3). Here only the FB runs are shown. The projections for `fg10_FB` are at $t = 250$ Myr and `fg50_FB` is at $t = 150$ Myr.

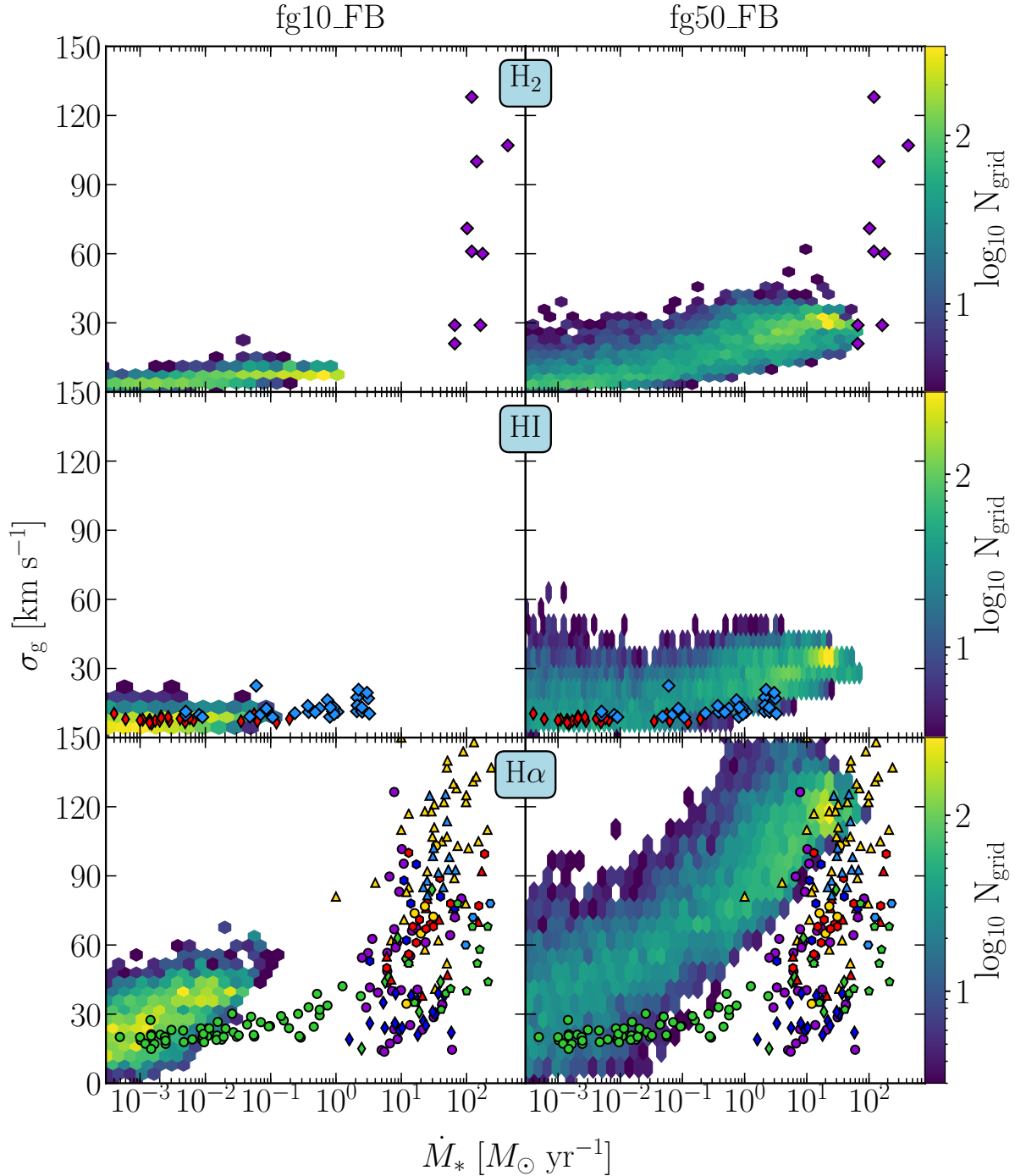


Figure 4.12: The σ_g -SFR relation in the fg10_FB and fg50_FB cases, using the more refined method for determining the different gas phases (detailed in Section 3.3.3). Comparing to Figure 4.10, which was a more rudimentary approach, these simulations are slightly different. Most notably, the σ_g for H α has changed for the lower gas fraction galaxy: the SFR is lower, which might be due to the warm ionised phase not being present in star forming clouds for long enough. The data presented here is evaluated from simulation outputs ($150 < t < 300$) Myr.

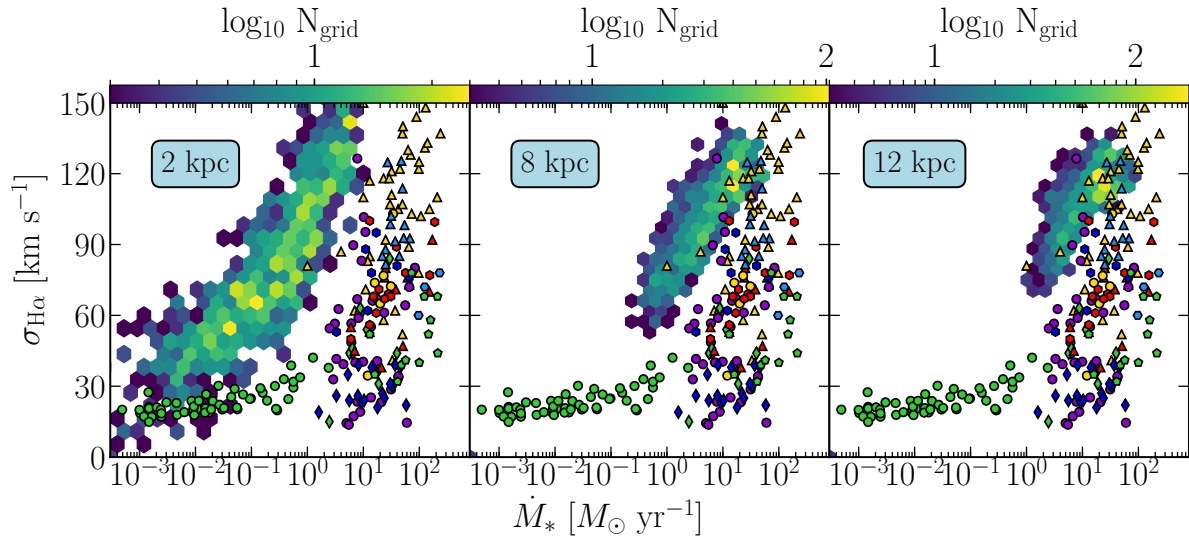


Figure 4.13: The σ_g -SFR relation for the $H\alpha$ tracer, using the detailed approach discussed in Section 3.3. The three plots are identical except that they show data for specific beam sizes, as written in the text boxes. This figure is meant to demonstrate the bias of the observational data, as high-redshift galaxies are mainly observed at with large beams sizes, equivalent to poor (large) spatial resolutions. The data used here is only for the `fg_50FB` run, evaluated for several at $270 > t > 150$ Myr.

Chapter 5

Discussion

In the previous chapter, I established the relation between velocity dispersion and star formation for my simulations. In this chapter I compare those results to the feedback- and gravity-driven analytic methods outlined in Section 2.6.1. Those models were derived using different assumptions regarding the stability of galactic discs. As I will demonstrate in this chapter, such assumptions are questionable, and require further evaluation, which is explored in Section 5.3.

5.1 Analytic models

The equations dictating the σ_g -SFR relation for the two analytic models, gravity- and feedback-driven turbulence, are shown in Eq. 2.15 and 2.18, respectively. The form which they predict for this relation is plotted in Figure 5.1, along with the data from references within Table 2.1. For these, I use the constant values recommended by KB16 in order to allow comparisons with their results (their Figure 1). They adopted a star formation efficiency per free-fall time of $\epsilon_{\text{ff}} \sim 1\%$ and integrate from $r_0 = 0.1$ kpc to $r_1 = 10$ kpc, which will be adopted in this project too. However, the Toomre Q values used in their models appear questionable to what is observed in local galaxies ($Q = 1 - 3$; Rafikov 2001; Leroy et al. 2008; Feng et al. 2014; Westfall et al. 2014) and what is found from simulations outside of clumps in high redshift galaxies. Additionally, the component representing the gas, Q_g , has been found to be significantly above unity for local as well as distant galaxies. This is confirmed by my simulations in Figure 5.4, which shows different Q parameters as a function of distance; this demonstrates how $Q_g \gtrsim 5$ and $Q \sim 1 - 3$ for almost the entire radius of the galaxy. This is further described in its captions and the sections below. Therefore, I here set the range of the parameters so that both models cover the entirety of the σ_g -SFR observational data. Not all of these values are necessarily realistic, which is used to argue whether the models can explain a particular region of the data.

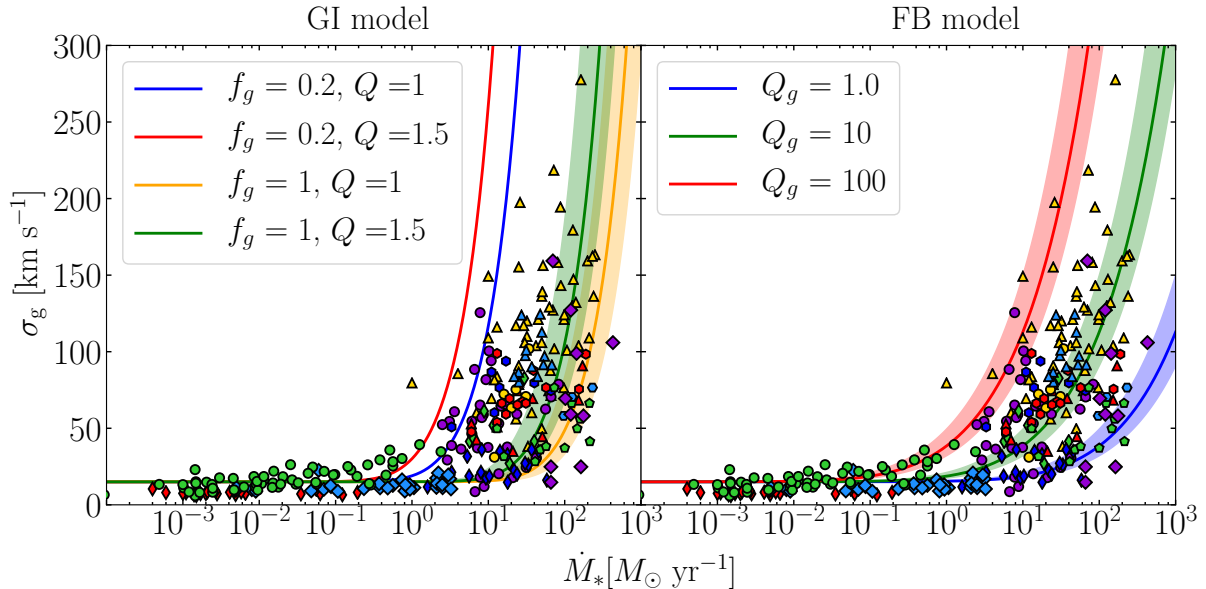


Figure 5.1: The σ_g -SFR relation predicted by the GI (left) and FB (right) analytic models (shown as lines) along with data points from the references in Table 2.1. The colour of the lines correspond to the free parameter values shown in the legends and using $v_c = 200$ km s^{-1} , while the shaded areas represent the interval $v_c = 150 - 250$ km s^{-1} ; chosen for comparisons with Figure 3 in KB16. The free parameters were chosen to encompass the entirety of the observational data.

5.1.1 Direct comparison with simulations

The most straightforward approach to evaluating the models is a direct comparison between the σ_g predicted from the models and the values calculated from the simulations. In order to do a direct comparison, values calculated from the simulations are inserted into the equations of the models; then this predicted value is compared with the σ_g from the simulations. The variables in the equations (Q_g , Q and \dot{M}_*) are calculated in each beam, while the constants applied are the same as for Figure 5.1. Due to the fact that the analytic models predict global quantities, the diameter of the beams used for the direct comparisons are on a few kpc scale and above. The results of this analysis can be seen in Figure 5.2, which shows both models for the `fg_10FB` and `fg_50FB` simulations. The contours show where 30, 68, and 80% of the data lies within, assumed to be focused around a global maximum. The dashed line works as an indication of where the observed and simulation data agree. For this figure, $Q_g = Q = 1$ is adopted in one of the plots (and the calculated values in the other plot) and my simulations indicate this is an acceptable assumption for the total Q parameter, but not for the gas (see Figure 5.4).

The first thing to note is that most of the points are on the dashed line for $\sigma_g \sim 50$ km s^{-1} and both of the model predictions are therefore valid in these regions. However, the models fail to represent both the lower and upper SFR regions; underestimating σ_g

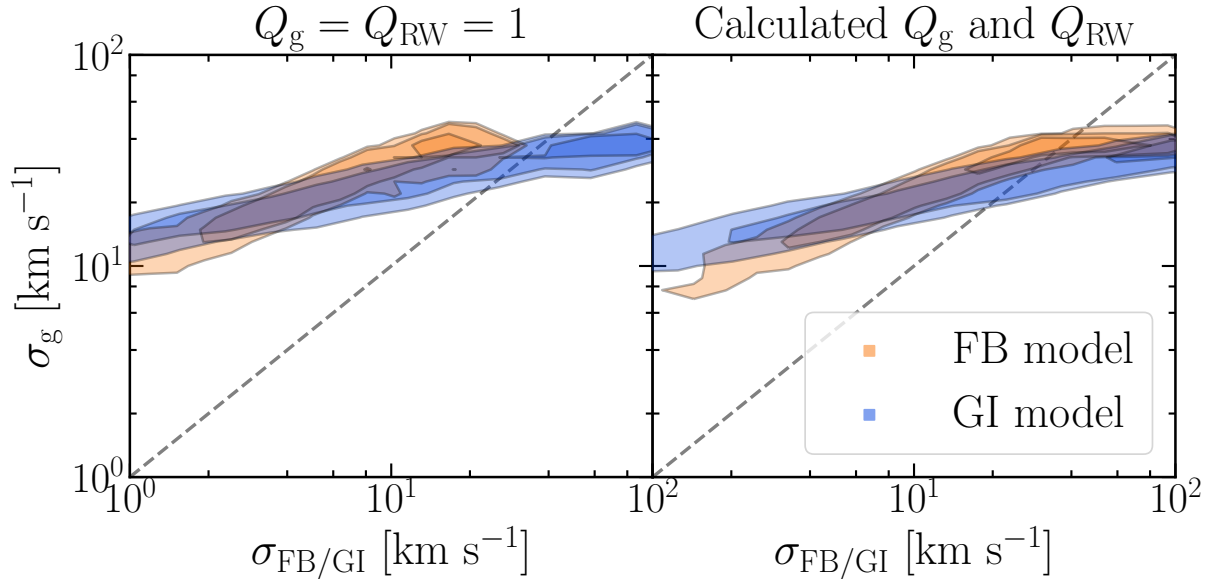


Figure 5.2: A direct comparison between the velocity dispersion from simulations (`fg50_FB`) and the analytic models in KB16. The colours correspond to the GI (blue) and FB (yellow) models and the different areas show where 30, 68 and 80% of the data is encompassed, centered around the region with the most points of data. The plot on the left has assumed the same Toomre Q values as in KB16 while the right plot uses the corresponding values derived from the simulation. The combined Q is here defined as Q for a thin disc.

in the regions of little star formation while overestimating σ_g for the starburst regions. This is in accordance with the difference in scaling of the σ_g -SFR relation between analytic models and what was found for the data in Table 4.1. In the case of using a set $Q_g \sim 1$ (as is assumed in KB16), the FB model prediction was found to deviate even further from the simulation and observational data.

Furthermore, the uncertainty and variability in quantities, especially for ϕ_P , F and ϵ_{ff} , can affect the velocity dispersions by a factor of a few. This could then result in a larger region of possible values for the FB model, as smaller values lead to larger velocity dispersions.

There is no huge noticeable difference between the [Krumholz et al. \(2018\)](#) and KB16 models in the direct comparison. Even though the newer paper has a lot more detail in it and consideration of both GI and FB, the scaling relations derived appear similar. Therefore, I simply continue using the models by KB10 and FQH13 in this section, as their form are comprehensible compared to the newer model, which have a lot of parameters that need to be considered. This heavy parameterisation requires that some parameters are set, which then must be motivated on a case-by-case basis. This further increases the uncertainty of the model, as the range of these assumed parameters might be significant.

5.1.2 Model predictions

In their paper, KB16 suggested that a relation unique for the GI model could be derived simply by rewriting Eq. 2.15 as σ/\dot{M}_* ; as done in Eq. 5.1. This would then yield a dependence on the global gas fraction, which they argue is not present in the FB model by FQH13. This prediction is seen in Figure 5.3. Unlike the similar figure presented by KB16 (their Figure 3), a constant circular velocity of $v_c = 220 \text{ km s}^{-1}$ with a varying star formation efficiency (the range of which is described in the captions of the Figure). This is motivated by the simulated galaxies having very similar rotation curves, while ϵ_{ff} can be drastically different for starburst galaxies. Most of the data and simulation points seem to lie within this region, but keep in mind the thickness of the shaded region; originating from the efficiency range.

$$\frac{\sigma}{\dot{M}_*} = \frac{G}{16\epsilon_{\text{ff}}v_c^2} \sqrt{\frac{3}{\phi_P}} \left(\ln \frac{r_1}{r_0} \right)^{-1} \frac{1}{f_g^2} \propto \frac{1}{\epsilon_{\text{ff}}} \frac{1}{f_g^2} \quad (5.1)$$

However, the FB model does have a dependence on the gas fraction of the galaxy through the Q_g parameter, which is assumed to be constant $Q_g \sim 1$ in KB16. The FB model's σ_g -SFR relation, Eq. 2.18, is rewritten in Eq. 5.2, by inserting the definition of Q_g , and yields a similar σ/\dot{M}_* relation. The resulting equation is Eq. 5.3 and is shown as the left plot in Figure 5.3, where $\Sigma_{\text{tot}} = 100 \text{ M}_\odot \text{ kpc}^{-2}$ has been adopted; taken from the suggested lower Σ_g limit, by FQH13, for the model. The shaded region corresponds to the total surface density range, here used as $\Sigma_{\text{tot}} = 50 - 1000 \text{ M}_\odot \text{ kpc}^{-2}$ (these values are found for my simulations, as can be seen in Figure 4.4). Again, this model also seems to be able to contain most of the simulation and data points, but with a rather large width. The overlapping of the two models' predictions within this field causes issues with disentangling the culprit. Therefore, evaluating σ_g/\dot{M}_* as a function of global gas fraction is not a good tool for the purposes of evaluating the likelihood of the models' accuracy.

$$\begin{aligned} \dot{M}_* &= \frac{8\sqrt{2}\phi v_c^2}{\pi G Q_g \mathcal{F}} \left(\ln \frac{r_1}{r_0} \right) \left(\frac{P_*}{m_*} \right)^{-1} \sigma^2 \\ &= \frac{8\sqrt{2}\phi v_c^2}{\pi G \mathcal{F}} \left(\ln \frac{r_1}{r_0} \right) \left(\frac{P_*}{m_*} \right)^{-1} \frac{\pi G \Sigma_g}{\kappa \sigma} \sigma^2 \implies \end{aligned} \quad (5.2)$$

$$\frac{\sigma}{\dot{M}_*} = \frac{\pi G \mathcal{F}}{8\sqrt{2}\phi v_c^2} \left(\ln \frac{r_1}{r_0} \right)^{-1} \left(\frac{P_*}{m_*} \right) \frac{\kappa}{\pi G \Sigma_g} \propto \frac{1}{\Sigma_g} = \frac{1}{\Sigma_{\text{tot}}} \frac{1}{f_g} \quad (5.3)$$

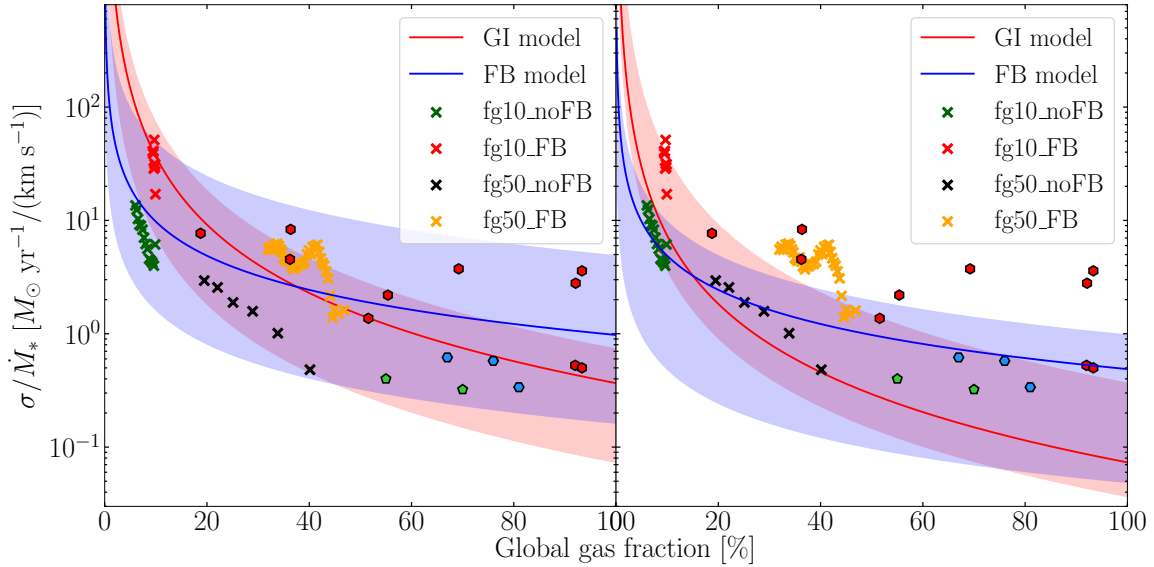


Figure 5.3: The relation predicted by the KB10 model between σ , SFR and the global gas fraction, f_g . The crosses show data from my simulations while the other markers represent the data points from Table 2.1. The specific curve predicted by the GI model is seen in Eq. 5.1, and is visualised as a red line and the curve predicted by the FB model is shown in Eq. 5.2. The coloured regions correspond to a range of possible values for the galaxies. The left and right plot adopt different ranges, to illustrate that a good match relies heavily on the exact values applied. *Left:* The GI model adopts $\epsilon_{\text{ff}} = 5\%$ for the line and $\epsilon_{\text{ff}} = 1 - 10\%$ as the range. The FB model adopts $\Sigma_{\text{tot}} = 100 \text{ M}_{\odot} \text{ kpc}^{-2}$ $\Sigma_{\text{tot}} = 50 - 1000 \text{ M}_{\odot} \text{ kpc}^{-2}$. *Right:* The GI model adopts $\epsilon_{\text{ff}} = 1\%$ for the line and $\epsilon_{\text{ff}} = 0.5 - 5\%$ as the range. The FB model adopts $\Sigma_{\text{tot}} = 50 \text{ M}_{\odot} \text{ kpc}^{-2}$ for the line and $\Sigma_{\text{tot}} = 20 - 3000 \text{ M}_{\odot} \text{ kpc}^{-2}$ for the range.

I find that:

- The direct comparison of σ between analytic models and simulation data shows that both models can predict the correct velocity dispersion when $\sigma_g \approx 50 \text{ km s}^{-1}$. Furthermore, the velocity dispersions cluster around this value. However, they do not follow the same scaling as found by simulations and can therefore not explain the higher σ at low SFR and the comparatively low σ at high SFR.
- Determining the dominant source of turbulence using the σ/M_* relations predicted by analytic models is not feasible. The lack of proper constraints allow the models to encompass a large region, in which there exists galaxies with different properties. However, it highlights how the uncertainties in parameters such as ϕ_p and the non-variability of e.g. the star formation efficiency ϵ_{ff} , yield a large scatter in the σ_g -SFR relation.

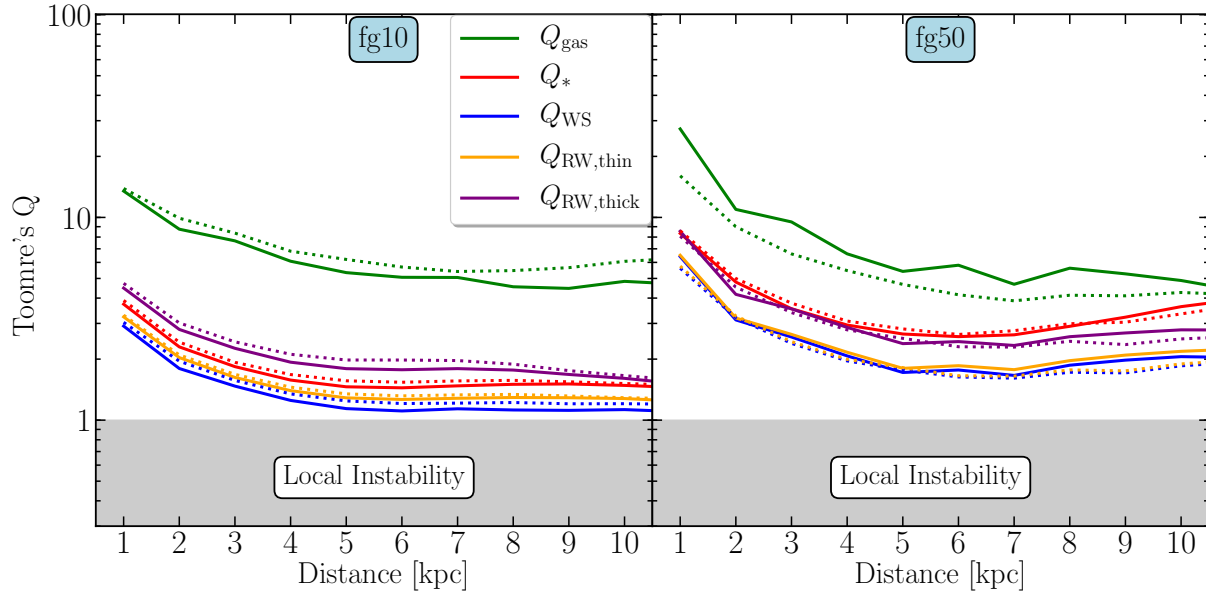


Figure 5.4: Toomre Q values plotted against the radial distance from the centre, including all runs; `fg10` on the left and `fg50` on the right, where the dotted lines are the runs without any feedback. The Q -values shown are for the gas, stars and the combined parameter, using three different methods for combining these, discussed in this section and explained in Section 2.5.2. These values were evaluated at kpc-scale beam size.

5.2 Driving turbulence in different phases

The decomposition of the different gas phases, as seen in Section 4.2.1, made it apparent that the dynamics of the gas differ significantly between the phases. This is a crucial point of discussion, since the observational data for the velocity dispersion is mainly composed of light emitted from the $H\alpha$ gas tracer. This phase was also found to be prominent in the runs including feedback, in alignment with theoretical work on the formation of the ISM (e.g. McKee & Ostriker 1977). Due to its dependence on stellar feedback, the turbulence of the ionised gas could be a unique factor to the feedback analytic model, which could be modelled. In this section, I perform a direct comparison of $\sigma_{H\alpha}$ with both models, to see if the high values predicted by models are related to the $H\alpha$ phase. Next, I try to derive a simple equation for the velocity dispersion in the warm ionised gas phase, assuming equipartition of the turbulent energy.

5.2.1 Comparison with analytic equations

A direct comparison with the model predictions and $\sigma_{H\alpha}$ from simulations is shown in Figure 5.5. In order to attain values for the analytic models, simulation data for the entirety of the gas (i.e. the values were not derived from any specific gas phase) was put into the equations of the GI and FB models (Eq. 2.15 and 2.18, respectively). The plots

show that the high velocity dispersions might be better represented when plotting the models against $\sigma_{\text{H}\alpha}$, as compared to σ_{g} for all of the gas. However, since the functional forms for the analytic equations are still vastly different from the data, which makes me conclude that there is no clear relationship between the models and the ionised gas phase and that the better match at higher velocity dispersion is simply a consequence of the warm ionised phase being more turbulent. A point of discussion is the values which should be inserted into the models, as the models were not implicitly derived for the ionised gas phase; perhaps the gas density, Toomre parameter, etc. of the warm ionised medium should be used.

5.2.2 Energy equipartition

Using a simplistic approach of assuming equipartition between all phases, the velocity dispersion of the ionised phase can be derived through the conservation of turbulent energy. This is done by saying

$$\begin{aligned} m_{\text{tot}}\sigma_{\text{g}}^2 &= F_{\text{HI}} \cdot m_{\text{HI}}\sigma_{\text{HI}}^2 + F_{\text{H}_2} \cdot m_{\text{H}_2}\sigma_{\text{H}_2}^2 + F_{\text{H}\alpha} \cdot m_{\text{H}\alpha}\sigma_{\text{H}\alpha}^2 + \dots \\ &\approx F_{\text{res}} \cdot m_{\text{res}}\sigma_{\text{res}}^2 + F_{\text{H}\alpha} \cdot m_{\text{H}\alpha}\sigma_{\text{H}\alpha}^2, \end{aligned} \quad (5.4)$$

where F is the fraction of turbulent energy in that phase and the non-ionised phases are assumed to be similar enough to be clumped into a residual term. The explicit assumptions done here are:

$$F_{\text{res}} = F_{\text{HI}} = F_{\text{H}_2}; \quad (5.5)$$

$$\sigma_{\text{res}} = \sigma_{\text{HI}} = \sigma_{\text{H}_2}. \quad (5.6)$$

If this proves insufficient, it is possible to simply input the values for HI and H₂ as well. Rewriting this equation, setting $f_{\text{H}\alpha} = m_{\text{H}\alpha}/m_{\text{tot}}$, the expression becomes

$$\sigma_{\text{H}\alpha} \approx \sigma_{\text{g}} \sqrt{\frac{F_{\text{H}\alpha} + f_{\text{H}\alpha} - F_{\text{H}\alpha}f_{\text{H}\alpha}}{f_{\text{H}\alpha}}}. \quad (5.7)$$

Here, I have also assumed that the velocity dispersion of the non-ionised phases is similar to the that of the total gas, $\sigma_{\text{res}} \approx \sigma_{\text{g}}$. The similarity is assumed based on decomposition of the velocity dispersion of the different phases, seen in Figures 4.9, 4.10 and 4.13 to be alike. To keep in mind is that some of this turbulent energy is dissipated into heat energy, which is not taken into account in these calculations. However, one could argue that this is balanced by the input of turbulent energy from e.g. gravitational instability or stellar feedback.

I plot Eq. 5.7 with different energy input fractions $F_{\text{H}\alpha}$ against the measured $\sigma_{\text{H}\alpha}$ in Figure 5.6. The comparison shows a remarkable agreement in values and scaling between analytic equation and simulation. The best match is given when roughly 40% of the turbulent energy is in H α , which is assumed a global factor here. The validity of this

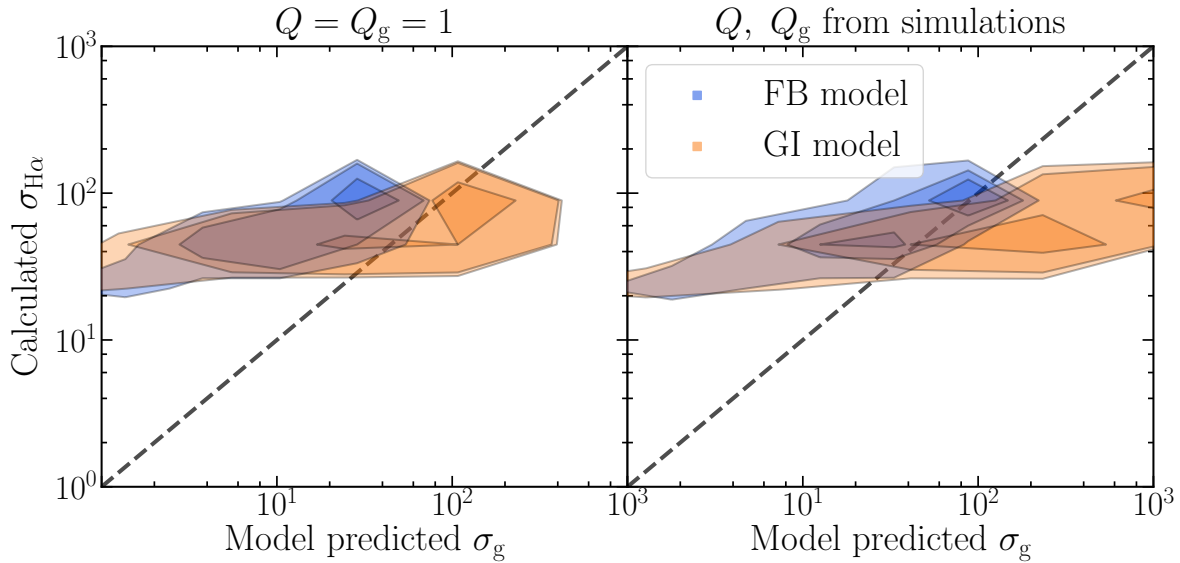


Figure 5.5: The velocity dispersion for H α derived from simulations plotted against the velocity dispersion predicted by the GI and FB models. The left plot assumes constant Toomre Q parameters, while the right one uses values derived from the simulation. These plots use the fg_50FB data.

factor is not looked into in this analysis, but it is not unreasonable that parts of the galaxy has this factor. Note that $\sigma_{H\alpha}$ and $\sigma_{g,\text{tot}}$ do not scale the same way (see Table 4.1), so the relationship shown here is not a variable plotted against itself. This was confirmed by plotting σ_g against $\sigma_{H\alpha}$ and not producing a linear relationship.

I find that:

- A direct comparison between the GI and FB model with the H α from simulations show that the model values change with the amount of H α dispersion. This comparison is able to show an agreement with models at high velocity dispersions. However, there is likely an underlying factor which is affecting both models and $\sigma_{H\alpha}$.
- A rudimentary approach of using equipartition theory to derive the velocity dispersion of H α works fairly well, appearing to also reproduce the scaling seen in the simulation data. Due to its simplistic nature, this approach may not be complete, but it indicates that models of $\sigma_{H\alpha}$ could be made to successfully reproduce simulations.

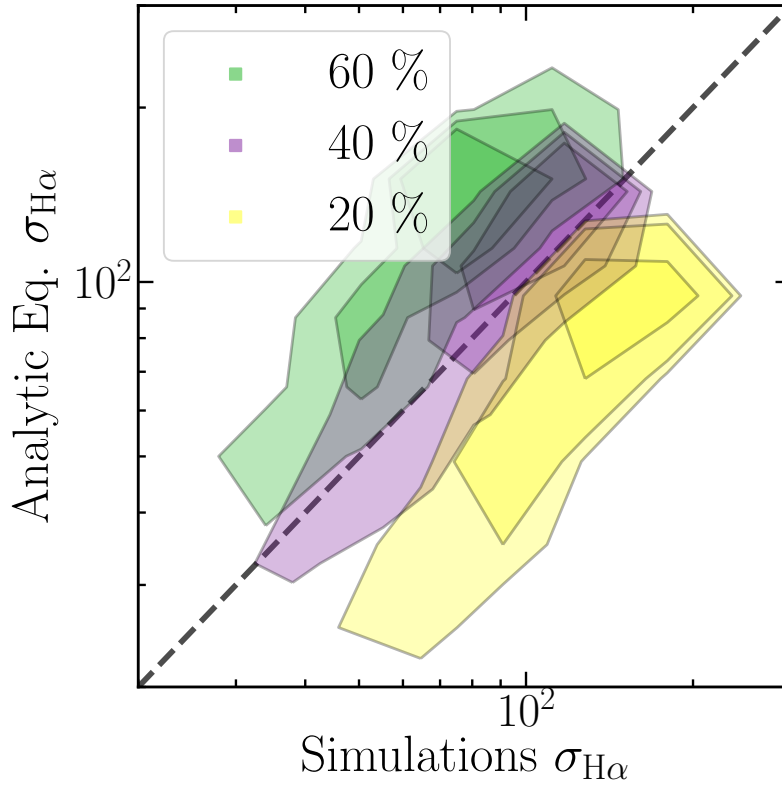


Figure 5.6: The relation between the $\sigma_{\text{H}\alpha}$ analytically derived, Eq. 5.7, and the one calculated from simulations. Different factors for the energy contributed by H α are used and the best agreement seem to be given for $F_{\text{H}\alpha} \approx 40\%$.

5.3 Disc instability as a driver of turbulence

In this section I discuss the different assumptions and conditions for disc instability, using Toomre’s Q parameter as a analytic tool for stability. The first step towards evaluating the stability criterion is to determine the Q :s from my simulations; Figure 5.4 shows different Toomre Q parameter as a function of the distance from the galactic centre. The figure includes all simulations performed and shows that the feedback does not significantly alter the stability of the disc on the scales evaluated ($\sim \text{kpc}$). However, the higher gas fraction galaxy shows a more stable disc (marginally stable at $Q \sim 2-3$). The observation that the attained values are independent on whether the galaxy is experiencing any stellar feedback, indicates that the turbulence is driven by gravitational instability. Furthermore, as both galaxies seem to be drawn towards $Q \sim 1-2$, this could be a natural progression of galactic discs.

In the GI model, the entirety of the galactic disc is assumed to be in a quasi-stable state. This is in agreement with the idea presented here but also with observational evidence,

which both show that the combined Q parameter is around unity throughout most of the disc in local galaxies. An issue, discussed earlier, with the approach of KB10 is their use of the overly simplified Wang-Silk approximation for combining the gas and star components. This is shown to closely resemble that of the more thorough Roman-Wiegert approach.

On the other hand, the FB model is supposedly dependent on the stability of the gas, as it only cares about the stars forming from the gaseous molecular clouds on a smaller scale. The contribution of the gas to the instability is different than that of the stars, which, in this section, is seen to be the dominant source most of the time. KB16 argue that Q_g must be of order unity in order to form self-gravitating giant molecular clouds, which is at odds with what I find in this thesis but also with observations of local and distant galaxies. Of course, the cloud must become gravitationally unstable in order to form stars, but this could be a question of scale and the redshift of the galaxy; high redshift disc galaxies can be rather clumpy, and the stability of an individual clump and a segment of the disc could be significantly different.

5.3.1 Deriving σ_g from Q

Assuming that the observed velocity dispersion of galaxies is caused by gravitational instability from the gas and stars, the derived expressions for the combined Q parameter can be rewritten and solved for σ_g . In this section, I present a derivation of σ_g from Q_{RW} and Q_{WS} (see Eq. 2.6 and subsequent equations). The purpose is to see how these compare to the simulations, but also whether there is a drastic difference between the two approaches of determining the combined Q parameter.

The contribution of the gas and star components to the instability of the disc changes with time (see Section 5.3.2), with gas seemingly driving the instability at the early ages of the galaxies. Although the expression for Q_{RW} is not as manageable as Q_{WS} , the former accounts for the thickness of the disc and considers both regions of instability (gas or stars), while the latter assumes an equal contribution and $\sigma_g \approx \sigma_*$. The weights, T , used to account for the thickness of the disc components, depend on the relative velocity dispersion in radial and vertical direction, which corresponds to an anisotropy of the turbulence direction. I here adopt the upper boundaries explained in Section 5.3.2, $0.5 \leq \sigma_z/\sigma_R \leq 1$, which is the more common (and less drastic) range for velocity anisotropy (compared to $0 \leq \sigma_z/\sigma_R \leq 0.5$).

The resulting equations for σ_g are shown in Eq. 5.8 and 5.9, labeled according to the Q -expression used to derive them. Both Q represent the same value, i.e. $Q_{\text{RW}} = Q_{\text{WS}} \approx 1-2$. In Figure 5.7, these predictions were calculated by inserting measured quantities of the simulated galaxies into the equations and were then plotted against the σ_g calculated from the simulations. For general use of these equations, when T might not be easily calculated, one can assume the isotropic limit of $T_g = T_* \approx 1.5$.

$$\sigma_{\text{WS}} = \frac{\pi G \Sigma_g}{\kappa} \left(\frac{1}{Q_{\text{WS}}} - \frac{1}{Q_*} \right)^{-1} \quad (5.8)$$

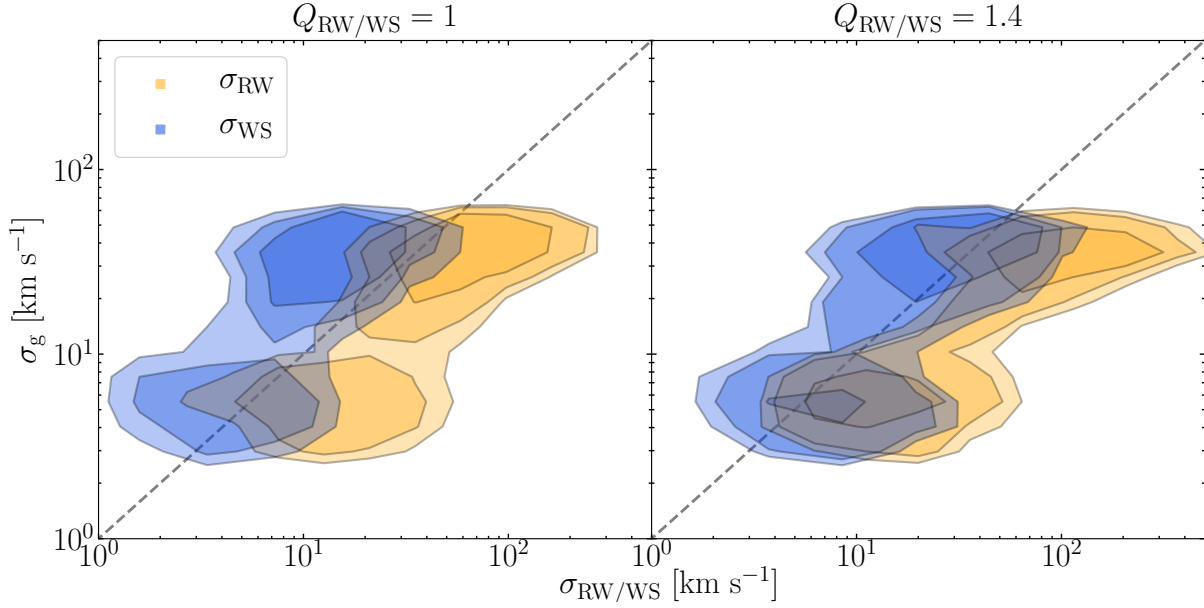


Figure 5.7: A direct comparison between the σ_g calculated from simulations and the ones predicted from Eq. 5.8 and 5.9; derived from two different approaches of combining Toomre Q parameters. The left and right plots show the differences between a slight change in the combined Q , motivated by the values seen in Figure 5.4. Both approaches seem to cluster around 50 km s^{-1} and 5 km s^{-1} . The lower values arise due to the outer region of the galaxy, where the Toomre Q are significantly different.

$$\sigma_{\text{RW}} = \sqrt{\frac{2\Sigma_g}{\Sigma_* T_g} Q_{\text{RW}} (Q_* - Q_{\text{RW}})^{-1} - \sigma_*^2} \quad (5.9)$$

$$= \sqrt{\frac{2\Sigma_g \sigma_*}{T_g} \left(\frac{\kappa}{Q_{\pi\text{GRW}}} - \frac{\Sigma_*}{T_* \sigma_*} \right)^{-1} - \sigma_*^2} \quad (5.10)$$

One can also derive the relationship when gas dominates the instability. However, this results in a third-grade polynomial without any elegant analytic solution. I used numerical tools to estimate where these roots are and find that very few points satisfies this equation and the ones which do have rather small velocity dispersions. This would seem to indicate that gas dominating the instability is rare (which I find), but also that the gas-dominated regime does not allow for high velocity dispersions through gravitational instability. Thus, the supersonic turbulence is driven by the stars. This could be at odds with the established idea that young galaxies were more turbulent, since these galaxies must also have contained more gas. This should be evaluated more thoroughly, for galaxies with a gas fraction larger than 50%.

5.3.2 Driver of the instability

The instability of the galactic disc is driven by its two components, gas and stars. Investigating the main driver of this instability is useful in the case that the turbulent motion is driven by gravitational instability. The first step is to determine under what circumstances these components are important, which is done here by looking at the criteria for the Toomre parameters, seen in Eq. 2.9. The instability is mainly driven by the gas when $T_g Q_g / T_* Q_* < 1$. The relation between $T_g Q_g / T_* Q_*$ and gas fraction has been plotted for all the simulation runs in Figure 5.10, in which it is evident that the gas dominates the instability when the galaxy has a high gas fraction and is rapidly taken over by the stars.

In order to discuss this, I have plotted the mass fraction of gas in the disc which is marginally unstable ($Q \lesssim 2$) against the simulation time and gas fraction, seen in Figure 5.8 and 5.9, respectively. The Q -parameters analysed are for the gas, stars and the combined Q_{RW} for a thick disc. The region in which gas dominates the instability is shown as a dashed line. The dependence of the stability with time and gas fraction is evident, gravitational instability of galactic discs was more prominent in the earlier lifetime of galaxies. The plots show both simulations, with and without feedback, and it can be seen that gas dominates the galaxy far longer in a galaxy without any feedback. This makes sense from the perspective that stellar feedback heats up the gas, while the stars remain kinematically cold. As a quick note, the choice of looking at marginally stable values here is motivated by Figure 5.4, in which it is evident that the higher gas fraction galaxy does not go far below this threshold. Therefore, to make any useful comparison, the same limit must be applied to the lower gas fraction simulation.

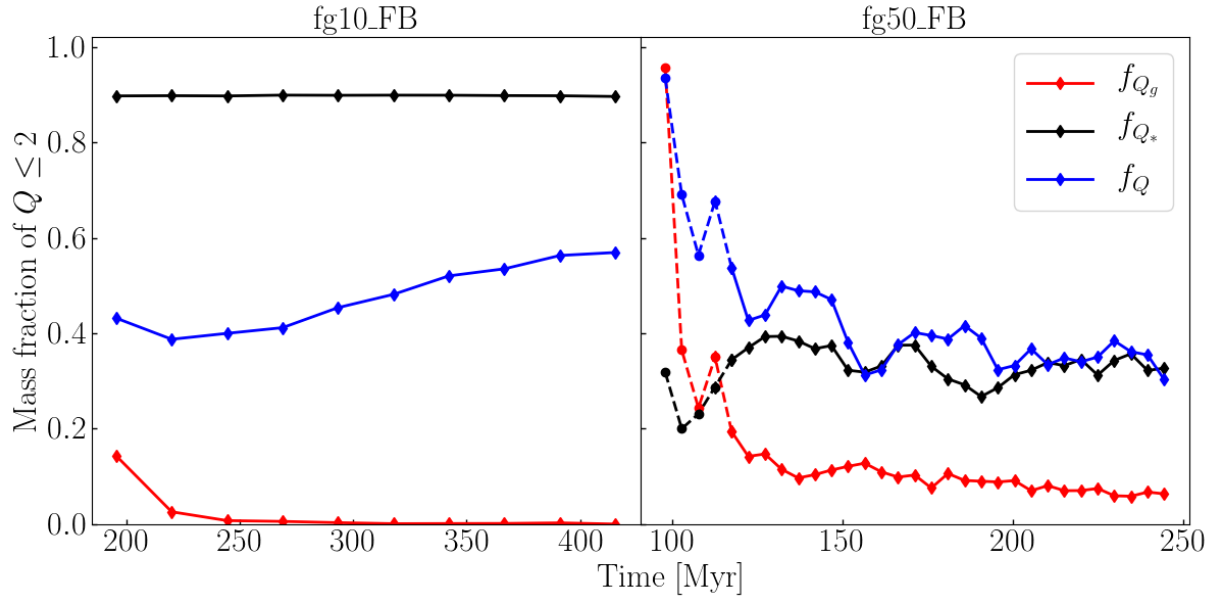


Figure 5.8: The fraction of mass in a marginally stable state ($Q \leq 2$), for different Toomre Q , as a function of the simulation time. Dashed lines correspond to the region in which the instability is driven by the gas. A clear transition from gas- to star-driven instability is seen to occur rather quickly. Note: the actual transition value is somewhere between the two data points with a dashed line between them.

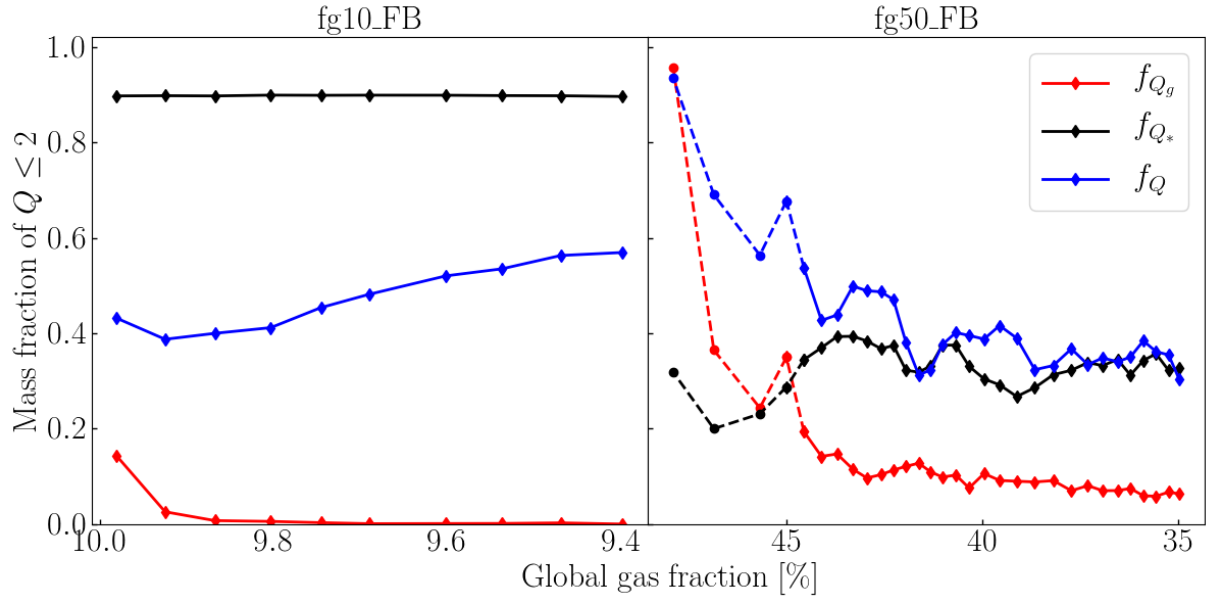


Figure 5.9: The fraction of mass in a marginally stable state disc ($Q \leq 2$), for different Toomre Q , as a function of the total gas fraction of the galaxy. Dashed lines correspond to the region in which the instability is driven by the gas. A clear transition from gas- to star-driven instability is seen to occur rather quickly. Note: the actual transition occurs somewhere between the two data points with a dashed line between them.

I find that:

- A velocity dispersion derived from a multi-component Toomre Q parameter, which is a measure of gravitational instability, can accurately predict the level of turbulence in simulated disc galaxies. I emphasize the importance of accounting for not only the stability of the gas, but also the stars.
- Toomre's Q parameter attains values $Q \sim 1 - 3$ and $Q_g \gtrsim 4 - 5$, independent on the heating mechanism of the disc (gravitational or stellar feedback). This indicates that the gas turbulence is driven by gravitational instability and that discs are drawn towards becoming marginally unstable.
- Galaxy instability is dominated by gas in the first \sim tens of Myr in the 50% gas fraction. Thereafter, it is dominated by the stars. Notably, if no feedback is present, the gas dominates the instability for a longer time. This can be explained by the star formation not being regulated by feedback, which results in the formation of large gravitationally unstable clumps that drive the instability.

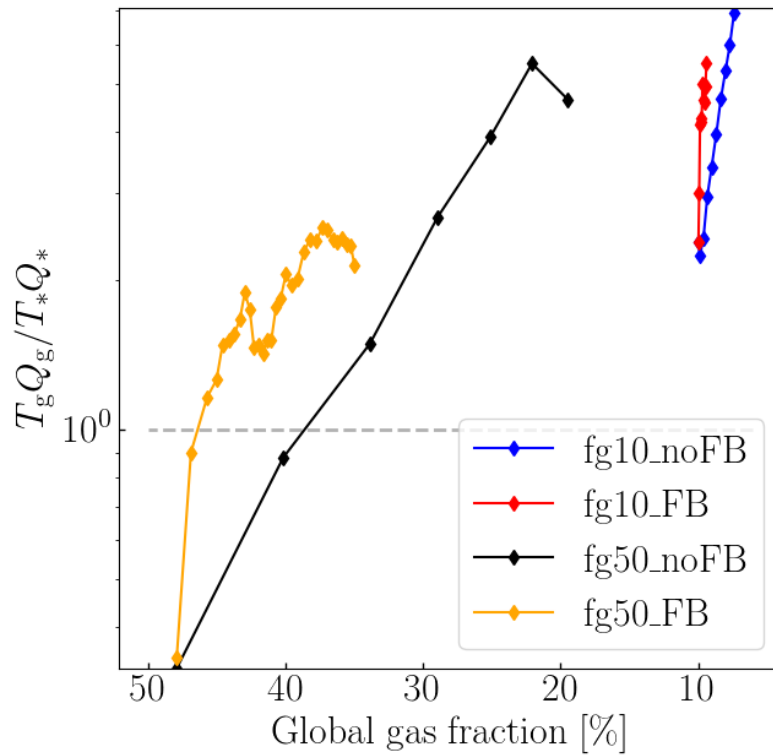


Figure 5.10: The ratio of TQ calculated for the gas and star components as a function of the global gas fraction. The product of the thickness weights T and Q values determine which component is dominating the instability. For a thin disc ($T = 1$) the ratio is simply a comparison between the Q parameters. The dashed line corresponds to the region in which the instability shifts from being driven by the gas or stars, where a ratio $T_g Q_g / T_* Q_* < 1$ indicates that the gas is driving the instability.

Chapter 6

Summary and Conclusions

In this chapter, I start by giving a brief overview of what this work is about, its purpose and how I achieve this. The key conclusions of my work are shown in a text box below, presented in list-form. In the next sections I summarise the methods I used for simulating galaxies and analysing the data. All of these sections can be read independently of the rest of the thesis and I encourage readers only wanting a basic understanding to prioritise going through these sections. The next section involves putting my results into context of other studies done in literature. Here I also discuss the possible implications and what future work could be done, which involves a discussion of methodological improvements.

Brief summary of my project

In this thesis I investigated the turbulent motion of gas in galactic discs and, in particular, its connection with star formation. This relation is observed as the increase of velocity dispersion (σ_g ; a measurement on the level of turbulence) with the star formation rate (SFR; denoted as \dot{M}_*), and has been detected in both local and high-redshift galaxies for a wide range of galaxy characteristics. Beyond affecting star formation, gas turbulence is important for a variety of galactic properties. However, the source of the gas turbulence remains undetermined. The purpose of my project was to examine the origin of this turbulence and evaluate how well analytic models work as predictors. Specifically, I focused on two proposed origins for gas turbulence that are popular in literature: gravitational instability and stellar feedback. These are dependent on the stability of the disc, which required investigating Toomre's Q , a stability criterion, for the analysis part.

My approach to study this gas turbulence was through N-body+hydrodynamic simulations of isolated galaxy discs. A key feature of performing simulations is that I am to experiment with the underlying physics of the galaxies. In particular, I performed simulations with and without stellar feedback, to investigate its effect on the gas turbulence. By considering different galactic parameters I simulate the equivalence of both local and high-redshift galaxies. For analysing the simulation data I use my own fully self-developed

pipeline of Python code, which is available upon request¹. The structure of my analysis was made to consider the impact of observational parameters, such as beam smearing (from galaxy inclination), the spatial scale observed (relevant for poorly resolved high-redshift galaxies) and the gas tracer used. Of particular interest was the warm gas phase traced by the H α -transition.

¹Email: timmy.ejdetjarn@gmail.com

My main conclusions are:

1. My simulations are able to reproduce key features in the observed σ_g -SFR relation: the plateau at $\sigma_g \sim 10 \text{ km s}^{-1}$ for $\dot{M}_* \lesssim 2 M_\odot \text{ yr}^{-1}$ and the exponential growth towards larger σ_g for $\dot{M}_* \gtrsim 2 M_\odot \text{ yr}^{-1}$. This result is independent of whether stellar feedback is included or not, and appears to be an outcome of how galactic discs regulate their gravitational stability (see point 6 below).
2. Simulated velocity dispersions only reach $\sigma_g \sim 60 \text{ km s}^{-1}$ at most, while the velocity dispersions of high-redshift galaxies have been observed to reach $\sigma_g \sim 150 \text{ km s}^{-1}$. I demonstrate that $\sigma_g > 60 \text{ km s}^{-1}$ can partly be explained by beam smearing. If not unaccounted for, or accounted for incorrectly, even galaxy inclinations of $\theta = 30^\circ$ can increase the observed velocity dispersions by factors of several. High-redshift galaxies are poorly resolved, and tend to have complex morphologies due to fragmentation and merging. It is therefore possible that beam smearing leads to overpredicted levels of gas turbulence.
3. While stellar feedback does not change the σ_g -SFR relation for the total gas content, it affects the level of turbulence in the warm gas phase, here traced by the $\text{H}\alpha$ transition. In this gas phase, feedback significantly increases the velocity dispersion from $\sigma_g \sim 50 \text{ km s}^{-1}$ to $\sigma_g \sim 130 \text{ km s}^{-1}$. As stated above, this is in good agreement with what is found in high-redshift galaxies, as observations have predominantly surveyed them in $\text{H}\alpha$.
4. Assuming energy equipartition between different gas phases, and simple arguments about the turbulent energy distribution, a relation between $\sigma_{\text{H}\alpha}$ and σ_g (for all of the gas) can be derived. This relation follows the calculated $\sigma_{\text{H}\alpha}$ exceptionally well. Furthermore, this analysis reveals that $\sim 40\%$ of the total turbulent energy is required to couple to the warm gas phase ($\sim 10^4 \text{ K}$, $\text{H}\alpha$), in order to drive the required high levels of turbulence.
5. Analytic models for the σ_g -SFR relation for gravitational instability and stellar feedback, taken from literature, can in principle reproduce the observed high velocity dispersion in rapidly star forming high-redshift galaxies. However, the parameters adopted in these models are highly uncertain, and the functional form of the predicted σ_g -SFR relation does not match that of the simulations.
6. The simulated galaxies are, when both stars and gas are accounted for, naturally drawn towards a Toomre stability level of $Q \sim 1 - 2$, *independent* of the source of the heating (galactic dynamics vs. stellar feedback). As mentioned above, this appears to be a fundamental property of galactic discs. As such, a multi-component Toomre Q parameter is a universally valuable analysis tool for predicting levels of gas turbulence in disc galaxies. In fact, σ_g from simple analytical relations (assuming $Q \sim 1$) and that found in the full galaxy simulations, are in close agreement.

Simulations and analysis summary

In order to investigate the gas turbulence of disc galaxies, I use RAMSES (Teyssier 2002), an N-body+hydrodynamics code to simulate isolated disc galaxies. RAMSES uses a grid-based method in order to solve the Eulerian equations for a self-gravitating fluid. The fluid is assumed an ideal mono-atomic gas with an adiabatic index of $\gamma = 5/3$ and gravity comes into the Eulerian equations as a source term, solved using the Poisson equation. The particles (stars and dark matter) are non-collisional and only interact with each other and the gas via gravity. The equations and how they are solved can be found in Section 3.1. The benefit of a grid-based code is that it resolves shocks in the fluid to a better degree than a particle-based method (e.g. smoothed particle hydrodynamics; SPH).

RAMSES adopts a grid-based adaptive mesh refinement (AMR) framework, which allows for selective refinement of the grid/mesh according to user-specified conditions. This ensures that only grid cells marked for refinement by these conditions will be further resolved. This avoids investing unnecessary computational time in regions which are not of interest. Refinement is handled in RAMSES by splitting a selected cell into eight equally sized cubes. For my simulations I have applied a condition for the mass within a cell, requiring refinement of a cell when it exceeds this threshold $m \geq M_{\odot}$. The lowest spatial scales resolved in my simulations have a physical size of $\Delta x \sim 10$ pc, which is enough to be able to marginally resolve individual molecular clouds. The refinement strategy is further explained in Section 3.1.1.

The galaxies which I simulate are isolated disc galaxies, with a Navarro-Frenk-White profile (Navarro et al. 1996) for the dark matter halo, a spherical Hernquist potential (Hernquist 1990) for the stars in the bulge and an exponentially shaped surface density for the stars and gas in the disc. The initial conditions were based on those from Agertz et al. (2013), but derived independently using GALIC (Yurin & Springel 2014). Different galactic parameters were chosen to emulate the characteristics of a local and a high-redshift galaxy, as outlined in Section 3.2.1. The key property changed here was the gas fraction of the galaxies, which, for an isolated galaxy, is strongly connected to the redshift. I performed two primary simulations that had initial gas fractions of $f_g = 10\%$ and $f_g = 50\%$, corresponding to a local and a high-redshift galaxy, respectively.

The formation of stars and stellar feedback effects used a sub-grid model (since these events are not resolved here) provided by Oscar Agertz (see e.g. Agertz & Kravtsov 2015). In order to explore the impact of stellar feedback on my simulations, each galaxy had a no-feedback counterpart that could be directly compared. A more thorough explanation of how these models were implemented into RAMSES is available in Section 3.1.2 and below.

The simulated galaxies were then validated through both visual comparison and known galaxy characteristics. In particular, I tested the simulation data with the Kennicutt-Schmidt relation and found good agreement, which encouraged further analysis. The distribution of densities and temperatures in the galaxies also followed what was expected from turning on/off stellar feedback and other simulations in literature. The validation of the data is discussed in Section 4.1.4.

The analysis of the simulations was done using a completely self-written Python code.

However, the galaxy analysis tool *yt* (Turk et al. 2011) was used for loading the data from the simulations and creating the projection plots seen throughout the thesis, see e.g. Figure 4.1 for an example. My code for deriving e.g. the velocity dispersion and Toomre’s Q was developed with the purpose of exploring the effects of observational parameters on these quantities, since they would later be compared with observational data. As such, I considered three observational parameters: beam size, galaxy inclination and gas tracer (corresponding to different gas phases). I wanted it to be possible to observe the entirety of the galaxy as if it was well-resolved, i.e. with several small beams. Therefore, I defined the positions of the beams to be homogeneously distributed in the galaxy (see Figure 3.2 for an intuitive look). For each position I had a set of beam sizes that I would use as well as a set of galaxy inclinations. The gas phases were evaluated in two ways, first using simple approximative temperature cuts and then by using the ionisation parameters provided by RAMSES. The latter method was performed to avoid calculating a mock spectrum of galaxy and from there determine the actual gas tracer emissions. One phase in particular, the warm ionised phase (traced by the $H\alpha$ emissivity), required calculating the recombination rates and collisional excitation. No significant discrepancy was found between the two methods. All of this is explained in more detail in Section 3.3.

This work in context of literature and future work

In this work, I have investigate the effects gravitational instability and stellar feedback could have on the gas turbulence in disc galaxies, in particular the σ_g -SFR relation. The simulations were done using RAMSES, an N-body+hydrodynamical code, and included star formation and stellar feedback, using a sub-grid model. Some physical processes are missing from these simulations, which limits parts of my analysis. For starters, no radiation physics is present, meaning that I am missing HII regions; bubbles of hot ionised gas around young stars. This could perhaps impact some of the results presented here for $H\alpha$. Furthermore, magnetic fields were not taken into account in my simulations, which are believed to be able to cause turbulence through magneto-rotational instabilities. This could have induced turbulence in the outskirts of galaxies, where there is little gravitational instability and star formation. The inclusion of an AGN would likely mainly be local effects, with the possibility of it affecting high-redshift and merged galaxies.

Beyond improving my simulations, my analysis would benefit from exploring different types of galaxies. The galaxies simulated in this project represented the same type of disc galaxy, but at different stages of its evolution. By simulating dwarf disc galaxies or a galaxy merger I could have explored how a merger shapes the gas turbulence and σ_g -SFR relation. With this I could compare with a highly inclination galaxy and determine how it differs; perhaps these could explain some of the high-star forming galaxies in the observational data.

I found that both of analytic models used in Krumholz & Burkhardt (2016) could describe the velocity dispersion of high redshift galaxies, but their scaling did not fit the simulated data. This makes it difficult to differentiate between the two models and infer anything

about which source is the actual driver. [Hung et al. \(2019\)](#) recently investigated the turbulence using the FIRE (Feedback In Realistic Environments) simulation suite and found that it was very difficult to infer anything from globally-averaged values and that SFR was temporally chaotic, i.e. it was not a smooth function of time. Instead, star formation was followed by a short rapid increase in velocity dispersion. The analytic model suggested by [Krumholz et al. \(2018\)](#) involved too much parameterisation to be feasibly applied without assuming a few parameters in a case-by-case basis. When I investigated the σ_g/\dot{M}_* relation, seen in Section 5.1, it became evident that by allowing a range of parameters, instead of having them set, the spread of the relation became quite large. This shows how the uncertainty or variability in galactic parameters used in analytical models are detrimental to their success.

However, the approach for equipartition with $H\alpha$ and Toomre’s Q parameter, I am optimistic that newer models that will consider the contribution of the warm ionised phase to the velocity dispersion could prove very resourceful. Especially for comparisons with high-redshift galaxies, given that most of their data is derived from the $H\alpha$ transition.

Observational data for the σ_g -SFR relation has been made for a large variety of observational parameters, which were shown in this thesis to be important. As mentioned earlier, the different phases have different dynamics and scale differently in the σ_g -SFR relation. The data compiled by [Krumholz et al. \(2018\)](#) contained observations of Ultra Luminous Infrared Galaxies. Such galaxies have very likely undergone mergers and, therefore, they do not resemble typical disc galaxies anymore. These galaxies could perhaps be compared with watching a disc galaxy edge-on, as they would not have a set rotational direction of a disc; which would then explain the high velocity dispersion attained from observations. Observational data of high-redshift galaxies where the velocity dispersion has not been corrected for inclination should not be used in a qualitative analysis of gas turbulence. For the future, the heterogeneity of the observational data needs to be addressed by researchers aiming to explore velocity dispersion in galaxies.

The results of this thesis are of interest to the galaxy and ISM community. Therefore, I have started writing on a manuscript, to be submitted to MNRAS (Ejdetsj rn & Agertz, in prep).

Acknowledgements

To start off, I want to give thanks to my supervisor Oscar Agertz for his guidance and advice during my Master's project. Also for proposing this project, which I have found to be very intriguing and challenging, in an enjoyable way. I have enjoyed and learned a lot from him every opportunity we have had to talk.

I wish to thank Nils Ryde for correcting my thesis, as well as for providing me with useful comments to improve my thesis.

I am grateful towards Matthew Orkney, who provided me with an approach for calculating the $H\alpha$ collisional excitation, and Jeremy Blaizot, who did the same for the $H\alpha$ recombination rates. Thanks to their help, I was able to go into depth on determining the different gas phases and thus improve the quality of my work presented here.

I also wish to thank you, the reader, for reading my thesis.

Lastly, I would like to thank everybody who I forgot to thank.

Bibliography

- Agertz, O. & Kravtsov, A. V. 2015, ApJ, 804, 18 [13, 35, 36, 86]
- Agertz, O. & Kravtsov, A. V. 2016, ApJ, 824, 79 [13]
- Agertz, O., Kravtsov, A. V., Leitner, S. N., & Gnedin, N. Y. 2013, ApJ, 770, 25 [23, 36, 37, 38, 44, 51, 86]
- Agertz, O., Teyssier, R., & Moore, B. 2009, MNRAS, 397, L64 [22]
- Alcorn, L. Y., Tran, K.-V., Glazebrook, K., et al. 2018, ApJ, 858, 47 [11, 31]
- Armillotta, L., Krumholz, M. R., & Fujimoto, Y. 2018, MNRAS, 481, 5000 [13]
- Bastian, N., Covey, K. R., & Meyer, M. R. 2010, ARA&A, 48, 339 [22]
- Behroozi, P. S., Wechsler, R. H., & Conroy, C. 2013, ApJ, 770, 57 [22]
- Benson, A. J. 2010, , 495, 33 [12]
- Bigiel, F., Leroy, A., Walter, F., et al. 2008, AJ, 136, 2846 [6, 12, 18, 22, 53, 54]
- Bigiel, F., Leroy, A. K., Walter, F., et al. 2011, ApJ, 730, L13 [13, 36]
- Binney, J. & Tremaine, S. 1987, Galactic dynamics [18, 26]
- Bullock, J. S., Kolatt, T. S., Sigad, Y., et al. 2001, MNRAS, 321, 559 [38]
- Caldú-Primo, A., Schruba, A., Walter, F., et al. 2015, AJ, 149, 76 [18, 24]
- Caldú-Primo, A., Schruba, A., Walter, F., et al. 2013, AJ, 146, 150 [18]
- Chabrier, G. 2003, Publications of the Astronomical Society of the Pacific, 115, 763 [22, 23, 36]
- Chepurnov, A., Burkhart, B., Lazarian, A., & Stanimirovic, S. 2015, ApJ, 810, 33 [18]
- Chomiuk, L. & Povich, M. S. 2011, AJ, 142, 197 [13]
- Chu, Y.-H. & Kennicutt, Jr., R. C. 1994, ApJ, 425, 720 [19]

- Clemens, D. P. & Barvainis, R. 1988, , 68, 257 [18]
- Cresci, G., Hicks, E. K. S., Genzel, R., et al. 2009, ApJ, 697, 115 [18, 31]
- Di Teodoro, E. M., Fraternali, F., & Miller, S. H. 2016, A&A, 594, A77 [25, 31]
- Dijkstra, M. 2017, arXiv e-prints, arXiv:1704.03416 [45]
- Diplas, A. & Savage, B. D. 1991, ApJ, 377, 126 [18]
- Elmegreen, B. G. 2011, in EAS Publications Series, Vol. 51, EAS Publications Series, ed. C. Charbonnel & T. Montmerle, 19–30 [18]
- Elmegreen, B. G. & Scalo, J. 2004, Annual Review of Astronomy and Astrophysics, 42, 211 [13]
- Epinat, B., Amram, P., & Marcelin, M. 2008, MNRAS, 390, 466 [31]
- Epinat, B., Contini, T., Le Fèvre, O., et al. 2009, A&A, 504, 789 [25, 31]
- Evans, II, N. J., Heiderman, A., & Vutisalchavakul, N. 2014, ApJ, 782, 114 [23]
- Faucher-Giguère, C.-A., Quataert, E., & Hopkins, P. F. 2013, MNRAS, 433, 1970 [14, 29]
- Feng, C.-C., Lin, L.-H., Wang, H.-H., & Taam, R. E. 2014, ApJ, 785, 103 [68]
- Ferrière, K. M. 2001, Reviews of Modern Physics, 73, 1031 [17]
- Genzel, R., Förster Schreiber, N. M., Lang, P., et al. 2014, ApJ, 785, 75 [18]
- Genzel, R., Newman, S., Jones, T., et al. 2011, ApJ, 733, 101 [31]
- Glazebrook, K. 2013, Publications of the Astronomical Society of Australia, 30, e056 [13]
- Green, A. W., Glazebrook, K., McGregor, P. J., et al. 2014, MNRAS, 437, 1070 [18]
- Gu, M., Conroy, C., & Behroozi, P. 2016, ApJ, 833, 2 [12]
- Hayward, C. C. & Hopkins, P. F. 2017, MNRAS, 465, 1682 [12]
- Hensler, G. 2009, in IAU Symposium, Vol. 254, The Galaxy Disk in Cosmological Context, ed. J. Andersen, Nordströara, B. m, & J. Bland- Hawthorn, 269–282 [12, 18]
- Hernquist, L. 1990, ApJ, 356, 359 [38, 86]
- Hockney, R. W. & Eastwood, J. W. 1981, Computer Simulation Using Particles [33]
- Hopkins, P. F., Quataert, E., & Murray, N. 2012, MNRAS, 421, 3488 [12, 13]
- Hui, L. & Gnedin, N. Y. 1997, MNRAS, 292, 27 [46]

- Hung, C.-L., Hayward, C. C., Yuan, T., et al. 2019, MNRAS, 482, 5125 [13, 88]
- Ianjamasimanana, R., de Blok, W. J. G., Walter, F., & Heald, G. H. 2012, AJ, 144, 96 [18, 31]
- Ianjamasimanana, R., de Blok, W. J. G., Walter, F., et al. 2015, AJ, 150, 47 [18]
- Kennicutt, Jr., R. C. 1998, ARA&A, 36, 189 [6, 13, 22, 53, 54]
- Khokhlov, A. 1998, Journal of Computational Physics, 143, 519 [35]
- Kim, C.-G. & Ostriker, E. C. 2015, ApJ, 802, 99 [36]
- Kolmogorov, A. 1941, Akademiia Nauk SSSR Doklady, 30, 301 [56]
- Kroupa, P. 2002, in Astronomical Society of the Pacific Conference Series, Vol. 285, Modes of Star Formation and the Origin of Field Populations, ed. E. K. Grebel & W. Brandner, 86 [22, 23]
- Krumholz, M. & Burkert, A. 2010, ApJ, 724, 895 [14, 28]
- Krumholz, M. R. 2015, arXiv e-prints, arXiv:1511.03457 [24]
- Krumholz, M. R. & Burkert, B. 2016, MNRAS, 458, 1671 [14, 25, 28, 87]
- Krumholz, M. R., Burkert, B., Forbes, J. C., & Crocker, R. M. 2018, MNRAS, 477, 2716 [28, 31, 42, 70, 88]
- Krumholz, M. R., Dekel, A., & McKee, C. F. 2012, ApJ, 745, 69 [29]
- Krumholz, M. R., McKee, C. F., & Tumlinson, J. 2009, ApJ, 693, 216 [45]
- Krumholz, M. R. & Tan, J. C. 2007, ApJ, 654, 304 [12]
- Lada, C. J., Lombardi, M., & Alves, J. F. 2010, ApJ, 724, 687 [23]
- Larson, R. B. 1981, MNRAS, 194, 809 [18, 19]
- Law, D. R., Steidel, C. C., Erb, D. K., et al. 2009, ApJ, 697, 2057 [31]
- Le Tiran, L., Lehnert, M., Nesvadba, N., Di Matteo, P., & van Driel, W. 2011, in Galaxy Formation, P21 [18]
- Lee, E. J., Miville-Desch nes, M.-A., & Murray, N. W. 2016, ApJ, 833, 229 [13]
- Lehnert, M. D., Le Tiran, L., Nesvadba, N. P. H., et al. 2013, A&A, 555, A72 [18, 31, 42, 55]
- Lehnert, M. D., Nesvadba, N. P. H., Le Tiran, L., et al. 2009, ApJ, 699, 1660 [18]

- Lemoine-Busserolle, M., Bunker, A., Lamareille, F., & Kissler-Patig, M. 2010, MNRAS, 401, 1657 [31]
- Leroy, A. K., Walter, F., Brinks, E., et al. 2008, AJ, 136, 2782 [68]
- Licquia, T. C. & Newman, J. A. 2015, ApJ, 806, 96 [13]
- Mac Low, M.-M. & Klessen, R. S. 2004, Reviews of Modern Physics, 76, 125 [13, 19, 56]
- Macciò, A. V., Dutton, A. A., van den Bosch, F. C., et al. 2007, MNRAS, 378, 55 [38]
- McKee, C. F. & Ostriker, E. C. 2007, ARA&A, 45, 565 [13]
- McKee, C. F. & Ostriker, J. P. 1977, ApJ, 218, 148 [12, 17, 23, 73]
- Megeath, S. T., Gutermuth, R., Muzerolle, J., et al. 2016, AJ, 151, 5 [22]
- Meidt, S. E., Schinnerer, E., García-Burillo, S., et al. 2013, ApJ, 779, 45 [18]
- Mo, H. J., Mao, S., & White, S. D. M. 1998, MNRAS, 295, 319 [38]
- Moiseev, A. V., Tikhonov, A. V., & Klypin, A. 2015, MNRAS, 449, 3568 [18, 31]
- Murray, N. 2011, ApJ, 729, 133 [18, 23]
- Naab, T. & Ostriker, J. P. 2017, ARA&A, 55, 59 [12, 15]
- Navarro, J. F., Frenk, C. S., & White, S. D. M. 1996, ApJ, 462, 563 [38, 86]
- Ostriker, E. C., Gammie, C. F., & Stone, J. M. 1999, ApJ, 513, 259 [13]
- Patrício, V., Richard, J., Carton, D., et al. 2018, MNRAS, 477, 18 [31]
- Peng, C. Y., Ho, L. C., Impey, C. D., & Rix, H.-W. 2002, AJ, 124, 266 [25]
- Petric, A. O. & Rupen, M. P. 2007, AJ, 134, 1952 [18]
- Rafikov, R. R. 2001, MNRAS, 323, 445 [68]
- Raiteri, C. M., Villata, M., & Navarro, J. F. 1996, A&A, 315, 105 [36]
- Romeo, A. B. & Falstad, N. 2013, MNRAS, 433, 1389 [27, 28]
- Romeo, A. B. & Wiegert, J. 2011, MNRAS, 416, 1191 [27]
- Rosen, A. & Bregman, J. N. 1995, ApJ, 440, 634 [36]
- Safronov, V. S. 1960, Annales d'Astrophysique, 23, 979 [25]
- Saintonge, A., Tacconi, L. J., Fabello, S., et al. 2012, ApJ, 758, 73 [22]

- Salim, D. M., Federrath, C., & Kewley, L. J. 2015, *ApJ*, 806, L36 [13, 19]
- Sanders, D. B. & Mirabel, I. F. 1996, *ARA&A*, 34, 749 [22]
- Schaye, J. & Dalla Vecchia, C. 2008, *MNRAS*, 383, 1210 [22]
- Schmidt, M. 1959, *ApJ*, 129, 243 [22]
- Spitzer, L. 1978, *Physical processes in the interstellar medium* [17]
- Stilp, A. M., Dalcanton, J. J., Skillman, E., et al. 2013, *ApJ*, 773, 88 [18, 31]
- Sutherland, R. S. & Dopita, M. A. 1993, , 88, 253 [36]
- Tacconi, L. J., Neri, R., Genzel, R., et al. 2013, *ApJ*, 768, 74 [18]
- Tamburro, D., Rix, H.-W., Leroy, A. K., et al. 2009, *AJ*, 137, 4424 [18]
- Teyssier, R. 2002, *A&A*, 385, 337 [32, 35, 37, 86]
- Tinker, J. L., Leauthaud, A., Bundy, K., et al. 2013, *ApJ*, 778, 93 [12]
- Toomre, A. 1964, *ApJ*, 139, 1217 [25]
- Turk, M. J., Smith, B. D., Oishi, J. S., et al. 2011, , 192, 9 [42, 87]
- van Zee, L. & Bryant, J. 1999, *AJ*, 118, 2172 [18]
- Varidél, M., Pracy, M., Croom, S., Owers, M. S., & Sadler, E. 2016, *Publications of the Astronomical Society of Australia*, 33, e006 [31]
- Wang, B. & Silk, J. 1994, *ApJ*, 427, 759 [27]
- Watson, D. F. & Conroy, C. 2013, *ApJ*, 772, 139 [12]
- Westfall, K. B., Andersen, D. R., Bershad, M. A., et al. 2014, *ApJ*, 785, 43 [68]
- Wisnioski, E., Glazebrook, K., Blake, C., et al. 2011, *MNRAS*, 417, 2601 [31]
- Yang, C.-C. & Krumholz, M. 2012, *ApJ*, 758, 48 [13]
- Yu, X., Shi, Y., Chen, Y., et al. 2019, *MNRAS*, 486, 4463 [13]
- Yurin, D. & Springel, V. 2014, *GALIC: Galaxy initial conditions construction*, *Astrophysics Source Code Library* [38, 86]
newpage